IN: Gann, R.G., Editor, Fire Suppression System Performance of Alternative Agents in Aircraft Engine and Dry Bay Laboratory Simulations, Vol. 1, Section 5, NIST SP 890, 121-200 pp, 1995

5. COMPATIBILITY WITH METALS

Mark R. Stoudt, James L. Fink, James F. Dante and Richard E. Ricker
Metallurgy Division
Materials Science and Engineering Laboratory

Contents

5.1 Introduction

Under current military practice, fire suppressants are stored for up to five years. Since the corrosivities of the chemicals currently under consideration as replacements for halon 1301 are not well known, there is a need for compatibility information between these chemicals and the array of materials used on high performance aircraft. As a result, experiments were conducted to assess the relative compatibility of the potential fire suppressants with the different metallic materials used for storage, distribution, and handling of aircraft fire suppressants.

On board an aircraft, the metallic materials will be exposed to fire suppressants during storage (storage vessels, rupture disks, etc.), deployment (distribution tubes, nozzles, etc.) and after deployment (structural and engine components exposed to combustion by-products). Of these possible exposures, the greatest concern for the safe operation of the aircraft lies in the possibility that the fire suppressant might cause attack of the storage vessels resulting in a loss of agent or prevention of proper operation of the deployment system.

In flight, the storage vessels, which are designed to contain the agent for up to five years, will experience pressure excursions up to 5.9 MPa at operational temperatures which will range from below ambient to those as high as 150 °C. At the maximum in-flight temperature, it is likely that the agent will surpass the critical temperature and will, therefore, be a single phase. At the lower in-flight and ground temperatures, the agent will be an equilibrium mixture of the liquid and vapor phases. Since corrosion behavior is a function of many variables and is also strongly dependent on temperature, it follows that the corrosion behavior at the ground conditions are likely to be very different from those in flight (Fontana, 1987).

Corrosion is defined as a degradation of the properties of a material resulting from a chemical reaction with the environment and can generally be classified into eight different categories based on the morphology of the corrosion damage. These eight forms are: general corrosion, pitting corrosion, crevice corrosion, intergranular corrosion, environmentally induced fracture, dealloying, galvanic corrosion, and erosion corrosion (Fontana, 1987). The definitions and descriptions of these forms of corrosion are detailed in an earlier report (Ricker, 1994). Of these eight corrosion failure modes, six are of potential concern for the storage, distribution, and post deployment corrosivity of fire suppressant agents on aircraft: general corrosion, pitting corrosion, crevice corrosion, intergranular corrosion, environmentally induced fracture, and dealloying (Ricker, 1994). Erosion corrosion may be a concern for nozzles, but the duration of the flow through the nozzle is very short and damage by this mechanism should be noted in the fire suppressant efficiency tests if it occurs. Galvanic coupling may influence corrosion damage accumulation, but due to the relatively low conductivity of these agents, galvanic effects should be minimal. As a result, the experiments were designed in a manner that would allow for the evaluation of the occurrence of the remaining six modes of damage (Ricker, 1994).

Very little is known about the corrosion behavior of the metals in these environments, and there is virtually no information available in the literature regarding the compatibility of these agents with the alloys used in the storage systems. As a result, corrosion experiments, which emulate these storage conditions, are a vital component in the selection of a replacement to halon 1301.

In the first phase of this investigation, a series of twelve possible replacements for halon 1301 were evaluated on the basis of a general ranking of the corrosivity with respect to storage vessel materials (Ricker, 1994). For the second phase, three candidates from the original list of twelve were selected for further study. These were: HFC-125, HFC-227ea, FC-218. An additional candidate, CF_3I, was also included in this corrosion study. The primary objective of the Phase II analysis was to assess the compatibility of this select group of replacement candidates over a broader range of environmental

conditions and longer exposure times. Since limited corrosion data is available for the selected alloys in 1301 in the literature, and the service performance record of this agent has been acceptable, this agent was included in Phase II as a reference environment.

The potential for corrosion damage to the structural materials of the aircraft by residual suppressant or by combustion by-products is also of great concern. These chemicals have been shown to form aggressive halide acids or salts during fire suppression (Nyden, 1994). Residual suppressant or the combustion by-products left on the surface of the structural components after deployment could result in extensive corrosion damage before they are cleaned.

This analysis was designed and conducted to further evaluate the compatibility of the replacement candidates selected for additional study under probable and potential service conditions. The experiments consisted of exposure tests which emulated the in-flight and on-the-ground conditions under which corrosion might occur followed by careful examination and evaluation of the resulting corrosion damage. Standard experimental techniques were employed to assess the potential for failure of the storage container alloys by the aforementioned six possible corrosion mechanisms in normal service. The techniques used for this evaluation consisted of immersion tests and slow strain rate tensile tests and were similar to those utilized in Phase I (Ricker, 1994). A new electrochemical technique was also developed to predict the corrosion behavior over a broader range of potential service conditions and incorporated into the analysis.

5.2 Mass Change Exposure Tests

Experiments were conducted to assess the changes in mass of container alloys as a result of a long term exposure to the replacements candidates. These measurements provided a basis to determine the rate of formation of surface scales or the rate of removal of metallic species due to the exposure to the replacement candidate. Also visual and optical microscopic examinations following the exposures allowed for further evaluation of the occurrence of pitting, intergranular corrosion, and dealloying.

5.2.1 Materials. The materials selected by the sponsors for evaluation in Phase II of this study represented the range of alloys currently in service as or under consideration for use as storage vessels. These were: 304 stainless steel, stainless steel alloy 21-6-9 (Nitronic 40)[1], titanium alloy 15-3-3-3 and 6061-T6 aluminum alloy. Shortly after the immersion tests began, a decision was made to include AISI 4130 alloy steel in the test matrix and the exposure times for this alloy were shortened appropriately. After HFC-125 was selected as the most likely candidate to replace halon 1301, several additional alloys were included for further testing in HFC-125 and halon 1301 in order to provide compatibility information over a broader range of materials. Those materials were: Inconel alloy 625, CDA-172 copper/beryllium alloy, CDA-110 copper alloy, 321 stainless steel, and AM-355 stainless steel. The compositions of these alloys are given in Table 1.

5.2.2 Experimental Procedure at 150 °C. All of the samples used for the weight loss immersion tests were flat coupons of the geometry shown in Figure 1 (ASTM G 01-93). The sample preparation

[1]Certain trade names and company products are mentioned in the text or identified in an illustration in order to specify adequately the experimental procedure and equipment used. In no case does such identification imply recommendation or endorsement by the National Institute of Standards and Technology, nor does it imply that the products are necessarily the best available for the purpose.

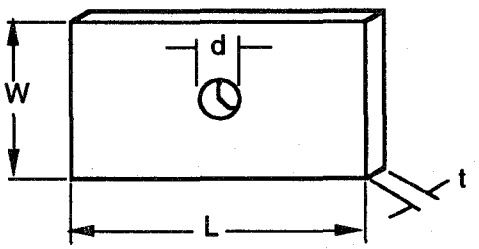

W = 25.4 mm (1.0 in)
L = 50.8 mm (2.0 in)
t = 1.6 mm (0.0625 in)
d = 6.7 mm (0.265 in)

General corrosion coupon design (ASTM G-01).

Figure 1. General corrosion coupon sample design (ASTM G 01-93).

Table 1. Composition of alloys tested in Phase II (mass fraction in percent)

Element	Nitronic 40	304 SS	Al 6061	Titanium 15-3-3-3	AISI 4130	Inconel 625	AM-355 SS	Cu-Be CDA 172	321 SS	Cu Alloy CDA 110
Al	--	--	bal	3.50	0.04	0.23	--	0.04	--	--
C	0.02	0.06	--	0.01	0.30	0.02	0.12	--	0.04	--
Cr	20.20	18.39	0.34	3.30	0.91	21.71	15.28	0.01	17.22	--
Cu	0.03	0.27	0.40	--	0.01	--	--	bal	0.10	99.95
Fe	bal	bal	0.70	0.11	bal	3.97	bal	0.06	bal	--
Mn	9.07	1.41	0.15	--	0.48	0.08	0.80	--	1.61	--
Mo	0.07	0.21	--	--	0.17	8.82	2.60	--	0.14	--
Ni	7.01	8.15	--	--	0.01	61.39	4.23	0.06	9.85	--
Ti	--	--	--	bal	--	--	--	--	0.43	--
V	--	--	--	14.70	--	--	--	--	--	--
Mg	--	--	1.20	--	--	--	--	--	--	--
Zn	--	--	0.25	--	--	--	--	--	--	--
B	--	--	--	--	--	--	--	--	--	--
N	0.31	0.03	--	0.01	--	--	0.12	--	0.02	--
Sn	--	--	--	3.00	--	--	--	--	--	--
Co	--	0.14	--	--	--	--	--	--	0.21	--
Nb	--	--	--	--	--	3.41	--	--	--	--
W	--	--	--	--	--	--	--	--	--	--
Be	--	--	--	--	--	--	--	1.94	--	--

technique used for these experiments was identical to that used for Phase I (Ricker, 1994). Three separate weighings were taken at approximately 30 s intervals and averaged. This average value was then referred to as the initial weight of the coupon. The balance used for these weight measurements was self-calibrating to maintain an accuracy to within $\pm$ 10 x 10^{-6} g with a reproducibility of no less than $\pm$ 15.1 x 10^{-6} g. Representative photographs of the surface of each alloy were also taken prior to the start of testing.

Prior to the start of each exposure test, three coupons of each alloy were mounted on a polytetrafluoroethylene (PTFE) rod with PTFE spacers between the samples. This was done (1) to separate and (2) to electrically isolate the samples so that the effects from galvanic couplings would be minimized. PTFE shields were also placed between the individual sets of alloys to protect them from contacting any corrosion products that may have formed on other alloy sets. The samples were next placed in a custom designed PTFE liner and placed into a 2 L pressure vessel, as shown in Figure 2, for exposure. The test vessel was sealed, connected to a mechanical vacuum pump and evacuated for a minimum of 45 min.

The mass of agent required to produce a nominal pressure of 5.9 MPa at 150 °C was determined with the same mass balance used for the elevated temperature tests in Phase I which is shown in the following equation: (Ricker, 1994)

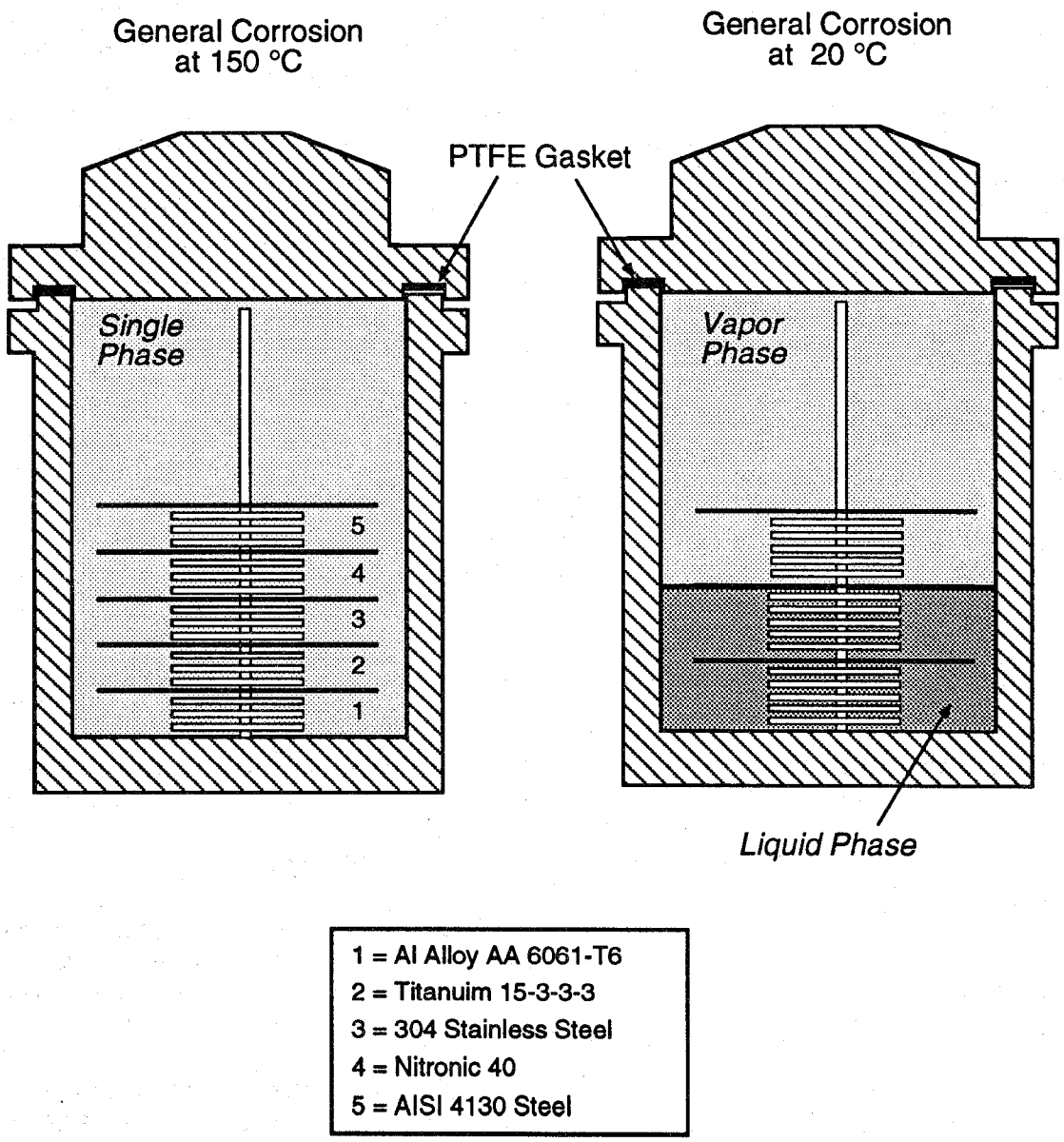

Figure 2. Schematic diagram of the immersion testing chamber used for general corrosion experiments.

$$M_T=\rho_l V_l+\rho_v V_v \quad (1)$$

where M_T is the total mass of the system, ρ_l is the density of the liquid agent at 20 °C, V_l is the volume of the liquid agent at 20 °C, ρ_v is the density of the vapor phase at 20 °C, and V_v is the volume of the vapor at 20 °C. To facilitate charging of the agents, the test vessels were chilled in a bath of either ice and water, or dry ice and alcohol, depending on the temperature necessary to maintain the liquid phase. The vessels were then placed on a balance so that the mass of the agent could be monitored during filling. Upon completion of the charging step, the vessels were placed in proportionally controlled, calrod-type heaters for the duration of the exposure period.

Mass-change measurements were performed on the coupons after one, two, four, eight, and twelve month elapsed times during the one year exposure. To minimize agent loss during the extraction process, the vessels were immersed in a bath of dry ice and alcohol for approximately three hours in order to condense as much of the agent as possible. The vessels were immediately sealed and returned to the cooling bath upon the extraction of the PTFE rod assemblies. After extraction, the samples were allowed to warm naturally to ambient temperature, promptly weighed using the standard weighing procedure, and then immediately returned to the test vessels.

At the end of the exposure tests, the agents were released, the coupons were extracted and immediately re-weighed, again using the standard weighing procedure. The average of the three weight measurements was then referred to as the final weight of the coupon. Representative photographs of the surfaces were again taken and compared to those of the initial condition.

A series of statistical analyses were performed on the weight loss coupon data. The results of these analyses were then used to evaluate the potential for general corrosion induced failure for each alloy in the replacement candidates.

5.2.3 Experimental Procedure at 20 °C. The sample charging procedure used for the ambient temperature experiments differed slightly from the one utilized for the tests at 150 °C. For these tests, the samples were not separated according to alloy type, but were stacked so that each set contained one coupon from each alloy. This sample arrangement was selected because it exposed two coupons from each alloy to the liquid phase, and one to the vapor phase as also shown in Figure 2. As with the tests conducted at 150 °C, each coupon was separated by a PTFE spacer and each alloy set was separated by a PTFE shield.

The agent filling procedure used for the ambient temperature tests was also slightly different from the high temperature test. For these tests, Equation (1) was used to determine an agent volume which located the interface region between the two phases near the midpoint of the vessel. The remainder of the procedure for these experiments was identical to the procedure used for the tests at 150 °C.

5.2.4 Results at 150 °C. The rate of mass change was calculated for each alloy/environment combination using the mass change measurements and the same relationship from Phase I (Ricker, 1994)

$$R=\frac{\Delta M}{A\cdot t} \quad (2)$$

where ΔM is the mass change, A is the total exposed area of the sample and t is the exposure time in days. These values are presented in Table 2. If the mass change rate is assumed to be essentially constant throughout the entire exposure period, then this relationship will provide a reasonable estimate of the average mass change rate for the duration of the exposure. While the magnitudes of these measurements are small they are larger than the minimum required to be statistically significant.

Linear regression analyses were also performed on the mass change rate values. Table 3 contains the results of a regression performed on mass change per unit area versus time basis (*i.e.*, ΔM/A vs t). In this table, the slope of the linear regression, m, corresponds to the estimated corrosion rate for each alloy/environment combination, R is the correlation coefficient for the linear regression, and the standard error is an estimate of the standard deviation of the estimated slope. In this table, it can be seen that the correlation coefficients reflect the high degree of scatter in the measurements. At this temperature, 4130 alloy steel in halon 1301 had the best correlation (R value > 0.9) and the 4130 alloy steel in HFC-125 was the worst (R < 0.1).

If the corrosion rates were indeed constant, then the weight changes would be linear and the regression slope would then equal the mass change rate for each exposure. However, in most cases the corrosion rate slows with time due to mass transport through the surface film thereby limiting the reaction rate. In this case, the corrosion rate should decrease with time following a square root of time dependence. As a result, a second regression was performed on the mass change data on a square root of time basis. If one assumes that transport through a surface film is rate limiting, then the rate of mass change would be inversely proportional to the thickness of the film according to the following relation:

$$\frac{\partial}{\partial t}\left(\frac{\Delta M}{A}\right)\alpha\frac{1}{\ell} \tag{3}$$

where the film thickness, ℓ, is proportional to the mass change per unit area. Solving this differential equation yields the equation used for the second regression:

$$\left(\frac{\Delta M}{A}\right)=kt^{1/2} \tag{4}$$

The results of this regression are presented in Table 4. The correlation coefficients for this analysis also exhibited a wide scatter ranging from > 0.9 for Al-6061 in HFC-125 to ~0.1 for 4130 in the same agent. While the correlations of this regression were better in some cases, the overall fit was not much better than the simple linear regression. As a result, a third regression was also performed on this data. This analysis assumes that part of the samples surface is bare and exhibits linear reaction kinetics while part is filmed and exhibits square root of time behavior so that:

$$\left(\frac{\Delta M}{A}\right)=m_0+m_1t+m_2t^{1/2} \tag{5}$$

This regression produced very good correlations for most of the environment/alloy combinations as shown in Table 5 and are also shown along with the raw mass change data as derived from the measurements made on the three samples of each of the alloys in each of the agents at 150 °C, (Figures 3-7). (The raw data used for these figures is presented in tabular form in Appendix A.)

Table 3. Mass change rate per unit area at 150 °C (g/meter^2 · day) estimated by the slope for a linear regression of mass change per unit area on exposure time (assumes constant, bare surface, reaction kinetics)

Alloy	HFC-125			HFC-227ea			Halon 1301		
	m	R	Std Err	m	R	Std Err	m	R	Std Err
Nit 40	0.00022	0.669	0.00006	0.00076	0.502	0.00036	0.00077	0.777	0.00016
Al 6061-T6	0.00233	0.800	0.00044	0.00474	0.861	0.00078	0.00237	0.681	0.00064
304 SS	0.00039	0.692	0.00010	0.00072	0.608	0.00026	0.00066	0.693	0.00017
Ti 15-3-3-3	0.00029	0.651	0.00009	0.00063	0.333	0.00049	0.00096	0.768	0.00020
AISI 4130	-0.00037	0.035	0.00407	-0.08934	0.413	0.07450	0.01737	0.937	0.00245
321 SS	‡	‡	‡	*	*	*	‡	‡	‡
CDA 110	‡	‡	‡	*	*	*	‡	‡	‡
CDA 172	‡	‡	‡	*	*	*	‡	‡	‡
AM 355	‡	‡	‡	*	*	*	‡	‡	‡
IN 625	‡	‡	‡	*	*	*	‡	‡	‡

Table 3. (continued)

Alloy	FC-218			CF_3I		
	m	R	Std Err	m	R	Std Err
Nit 40	0.02284	0.855	0.00384	0.07057	0.435	0.04622
Al 6061-T6	0.01996	0.454	0.01085	0.05121	0.864	0.00944
304 SS	0.00140	0.848	0.00024	0.19160	0.887	0.03156
Ti 15-3-3-3	0.00578	0.792	0.00124	0.00973	0.410	0.00819
AISI 4130	0.03982	0.804	0.01112	-0.45896	0.792	0.13382
321 SS	*	*	*	*	*	*
CDA 110	*	*	*	*	*	*
CDA 172	*	*	*	*	*	*
AM 355	*	*	*	*	*	*
IN 625	*	*	*	*	*	*

* No measurements were made in this alloy/environment combination
‡ Only one exposure time used for these measurements, see the average mass change rate table
m = estimated mass change rate for linear regression of mass change per unit area on exposure time (g/meter^2 · day)
R = correlation coefficient for regression
Std Error = estimated standard deviation for the mass change rate (regression slope)

Table 4. Mass change rate per unit area at 150 °C (g/meter^2 · day) estimated by the slope for a linear regression of mass change per unit area on square root of the exposure time (assumes a uniformly filmed surface)

Alloy	HFC-125			HFC-227ea			Halon 1301		
	k	R	Std Err	k	R	Std Err	k	R	Std Err
Nit 40	0.00552	0.831	0.00092	0.01415	0.661	0.00446	0.01849	0.922	0.00194
Al 6061-T6	0.05442	0.923	0.00566	0.07080	0.922	0.00827	0.05913	0.839	0.00958
304 SS	0.00220	0.855	0.00147	0.01347	0.811	0.00269	0.00243	0.875	0.00232
Ti-15-3-3-3	0.00802	0.710	0.00221	0.01466	0.555	0.00609	0.02338	0.922	0.00246
AISI 4130	0.01836	0.140	0.49160	-1.10539	0.419	0.90484	0.22373	0.991	0.01171
321 SS	‡	‡	‡	*	*	*	‡	‡	‡
CDA 110	‡	‡	‡	*	*	*	‡	‡	‡
CDA 172	‡	‡	‡	*	*	*	‡	‡	‡
AM 355	‡	‡	‡	*	*	*	‡	‡	‡
IN 625	‡	‡	‡	*	*	*	‡	‡	‡

Table 4. (continued)

Alloy	FC-218			CF_3I		
	k	R	Std Err	k	R	Std Err
Nit 40	0.30768	0.818	0.06006	1.16426	0.657	0.42281
Al 6061-T6	0.26926	0.440	0.15261	0.53902	0.819	0.11951
304 SS	0.00450	0.783	0.00396	2.20300	0.918	0.30045
Ti-15-3-3-3	0.08392	0.824	0.01598	0.13561	0.343	0.14058
AISI 4130	0.48701	0.807	0.13449	-6.09099	0.862	1.35119
321 SS	*	*	*	*	*	*
CDA 110	*	*	*	*	*	*
CDA 172	*	*	*	*	*	*
AM 355	*	*	*	*	*	*
IN 625	*	*	*	*	*	*

* No measurements were made in this alloy/environment combination

‡ Only one exposure time used for these measurements, see the average mass change rate table

k = estimated mass change rate for linear regression of mass change per unit or square root of the exposure time (g/meter^2 · day$^{1/2}$)

R = correlation coefficient for linear regression

Std Error = estimated standard deviation for the mass change rate (regression slope)

Table 5. Mass change rates at 150 °C estimated from a regression model that assumes mixed bare and filmed surface kinetics

HFC-125

Alloy	M_0	M_0(error)	M_1	M_1(error)	M_2	M_2(error)	R
Nit 40	-0.00201	0.00986	-0.00038	0.00011	0.01282	0.00219	0.913
Al 6061-T6	-0.06235	0.06541	-0.00213	0.00072	0.09514	0.01452	0.952
304 SS	-0.00825	0.01503	-0.00065	0.00017	0.0220.	0.00334	0.931
Ti-15-3-3-3	-0.00179	0.01893	-0.00065	0.00021	0.02397	0.00420	0.920
AISI 4130	0.000	0.35385	-0.07341	0.03582	0.57720	0.26956	0.658
321 SS	‡	‡	‡	‡	‡	‡	‡
CDA 110	‡	‡	‡	‡	‡	‡	‡
CDA 172	‡	‡	‡	‡	‡	‡	‡
AM 355	‡	‡	‡	‡	‡	‡	‡
IN 625	‡	‡	‡	‡	‡	‡	‡

Table 5. (continued)

Halon 1301

Alloy	M_0	M_0(error)	M_1	M_1(error)	M_2	M_2(error)	R
Nit 40	-0.01110	0.01654	-0.00095	0.00018	0.03665	0.00367	0.974
Al 6061-T6	-0.06996	0.10502	-0.00390	0.00115	0.13374	0.02331	0.912
304 SS	0.00554	0.01651	-0.00126	0.00018	0.04079	0.00366	0.972
Ti-15-3-3-3	-0.01031	0.01885	-0.00129	0.00021	0.04813	0.00418	0.979
AISI 4130	$1.15e^{-10}$	0.09515	0.00234	0.00964	0.33181	0.07258	0.993
321 SS	‡	‡	‡	‡	‡	‡	‡
CDA 110	‡	‡	‡	‡	‡	‡	‡
CDA 172	‡	‡	‡	‡	‡	‡	‡
AM 355	‡	‡	‡	‡	‡	‡	‡
IN 625	‡	‡	‡	‡	‡	‡	‡

Table 5. (continued)

FC-218

Alloy	M_0	M_0(error)	M_1	M_1(error)	M_2	M_2(error)	R
Nit 40	-0.17990	0.56982	0.02352	0.01314	-0.00991	0.18321	0.855
Al 6061-T6	-0.14014	1.61140	0.01692	0.03715	0.04445	0.51810	0.455
304 SS	0.00294	0.03554	0.00182	0.00082	-0.00613	0.01143	0.852
Ti-15-3-3-3	-0.04398	0.17003	0.00050	0.00392	0.07724	0.05467	0.825
AISI 4130	0.00001	1.25580	0.08739	0.12758	0.10738	0.96200	0.813
321 SS	*	*	*	*	*	*	*
CDA 110	*	*	*	*	*	*	*
CDA 172	*	*	*	*	*	*	*
AM 355	*	*	*	*	*	*	*
IN 625	*	*	*	*	*	*	*

Table 5. (continued)

HFC-227ea

Alloy	M_0	M_0(error)	M_1	M_1(error)	M_2	M_2(error)	R
Nit 40	-0.00571	0.04056	-0.00197	0.00094	0.03995	0.01304	0.762
Al 6061-T6	0.00940	0.08720	-0.00099	0.00201	0.08400	0.02804	0.923
304 SS	-0.00153	0.01084	-0.00212	0.00025	0.04168	0.00348	0.975
Ti-15-3-3-3	-0.00582	0.04084	-0.00402	0.00094	0.06807	0.01313	0.852
AISI 4130	0.000	8.55920	-0.15585	0.86606	-0.56139	6.52660	0.420
321 SS	*	*	*	*	*	*	*
CDA 110	*	*	*	*	*	*	*
CDA 172	*	*	*	*	*	*	*
AM 355	*	*	*	*	*	*	*
IN 625	*	*	*	*	*	*	*

Table 5. (continued)

CF_3I

Alloy	M_0	M_0(error)	M_1	M_1(error)	M_2	M_2(error)	R
Nit 40	0.00119	1.4523	-0.35183	0.05306	4.9333	0.58918	0.953
Al 6061-T6	-0.06787	0.87966	0.05271	0.03214	-0.01757	0.35687	0.864
304 SS	-0.12567	2.5037	0.03099	0.09147	1.8759	1.0157	0.919
Ti-15-3-3-3	0.12893	0.55508	-0.04101	0.02028	0.88433	0.22519	0.915
AISI 4130	-2.12e10	12.199	0.50302	1.2265	-13.27	9.2174	0.876
321 SS	*	*	*	*	*	*	*
CDA 110	*	*	*	*	*	*	*
CDA 172	*	*	*	*	*	*	*
AM 355	*	*	*	*	*	*	*
IN 625	*	*	*	*	*	*	*

* No measurements were made in this alloy/environment combination
‡ Only one exposure time used for these measurements, see the average mass change rate table
m_0 = g/meter^2
m_1 = g/meter^2 · day
m_2 = g/meter^2 · day$^{1/2}$

Figure 3 shows the mass change per unit exposed area for each sample in FC-218. The performances of the alloys in HFC-227ea, HFC-125 and in halon 1301 are shown in Figures 4, 5, and 6, respectively. Examination of these figures revealed that the majority of the observed changes were mass increases. Mass increases are not uncommon during immersion testing and are generally an indication of the formation and growth of a scale on the surface of the samples. Visual examinations confirmed the presence of such surface films; the samples were discolored in many cases. During immersion tests in aqueous solutions, the scales that form are usually oxide and/or hydroxide films. In the case of exposures to the replacement candidates, the films may be the result of reaction with the agent residual gasses, decomposition products, or just deposits of decomposition products. The large variations in mass exhibited in these figures could be due to cracking and/or spalling of these surface scales during the exposure period or during sample handling necessary for the measurements. Generally, the 4130 alloy steel exhibited the largest mass changes in every agent and the poorest correlation coefficients. Again, these were usually mass increases; however, the 4130 steel did exhibit significant mass decreases in the CF_3I (Figure 7). These decreases in mass are believed to be the result of active corrosion processes.

At this temperature, the CF_3I appeared to be substantially more aggressive than the other agents evaluated. The magnitudes of the mass changes observed in this agent were larger as a result of the formation of substantially thicker surface films. This hypothesis was supported by the results of the visual inspections performed on the coupons. While visual examination found that films were also present on the 4130 steel samples, they were layers of loose corrosion products. In general, the magnitudes of the mass changes for the 4130 steel were consistently higher than the other alloys tested in the same environments.

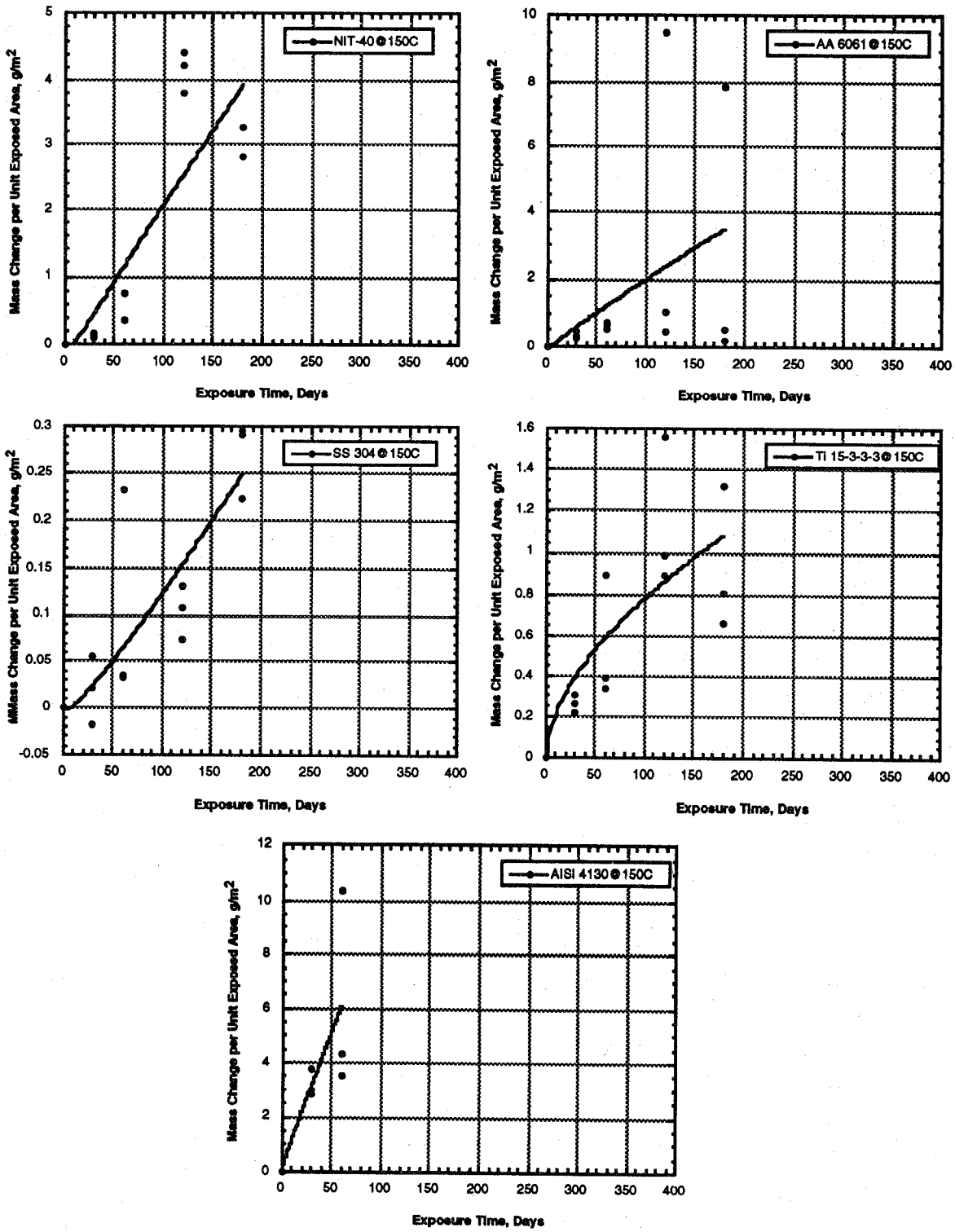

Figure 3. Mass change versus exposure time in FC-218 at 150 °C.

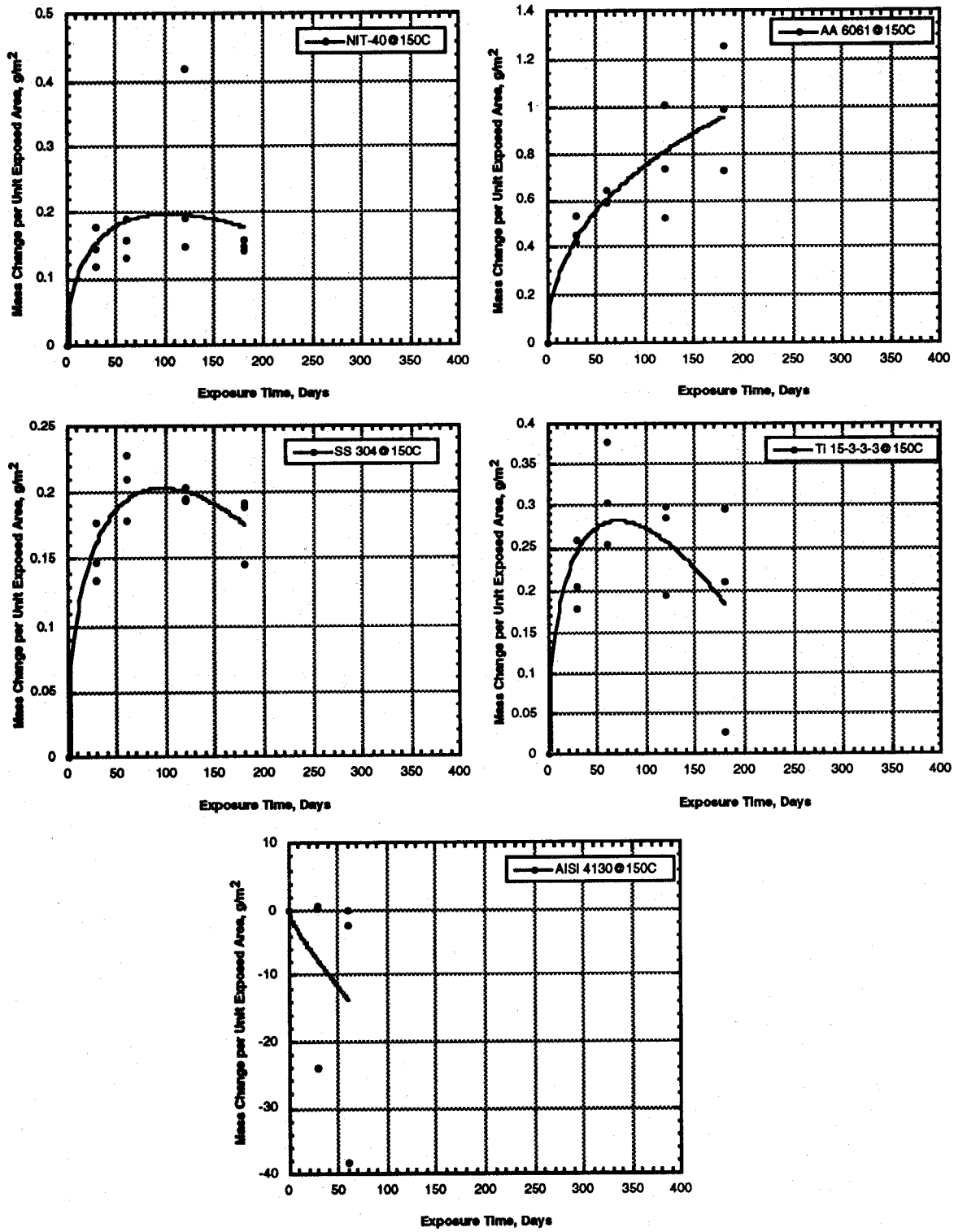

Figure 4. Mass change versus exposure time in HFC-227ea at 150 °C.

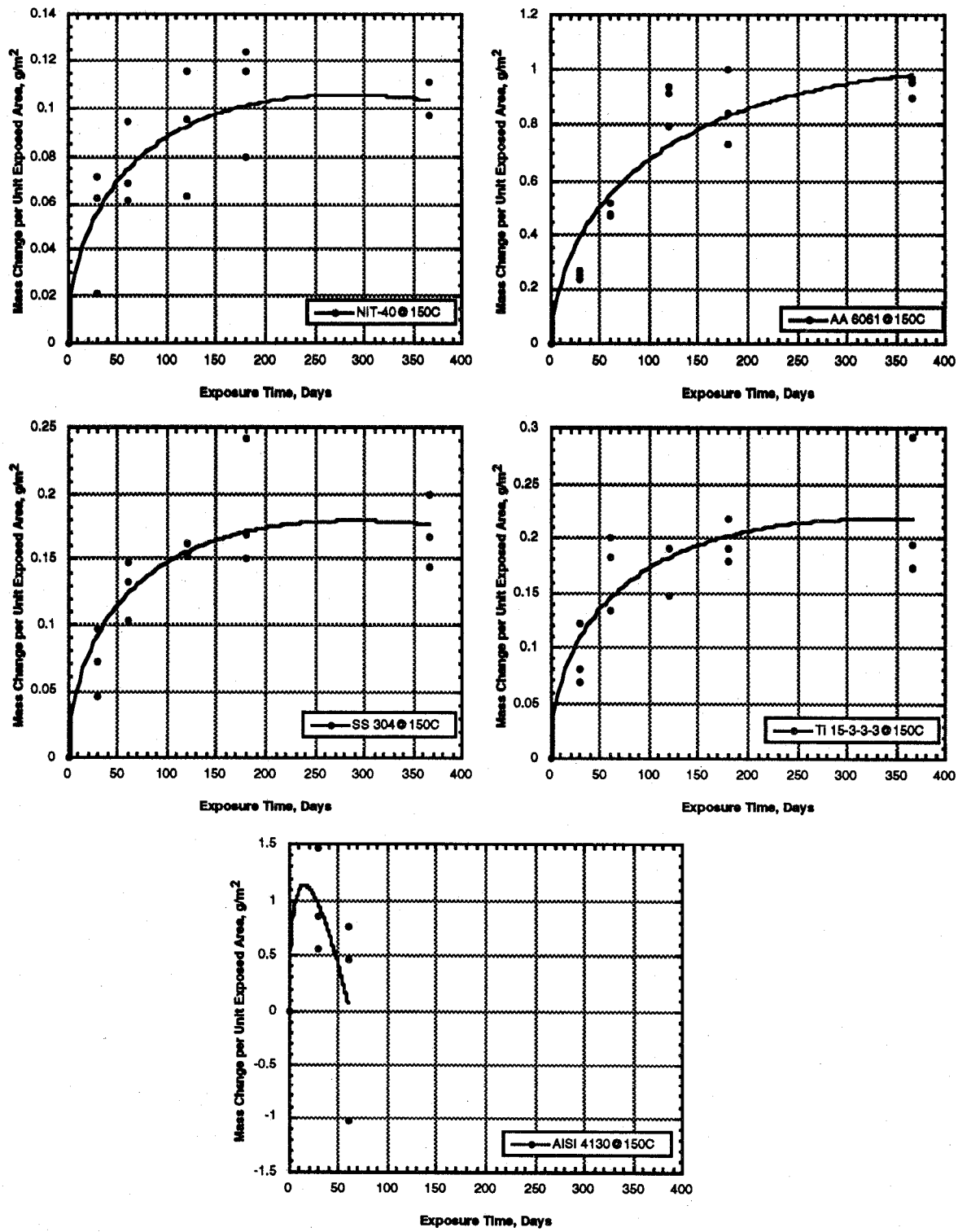

Figure 5. Mass change versus exposure time in HFC-125 at 150 °C.

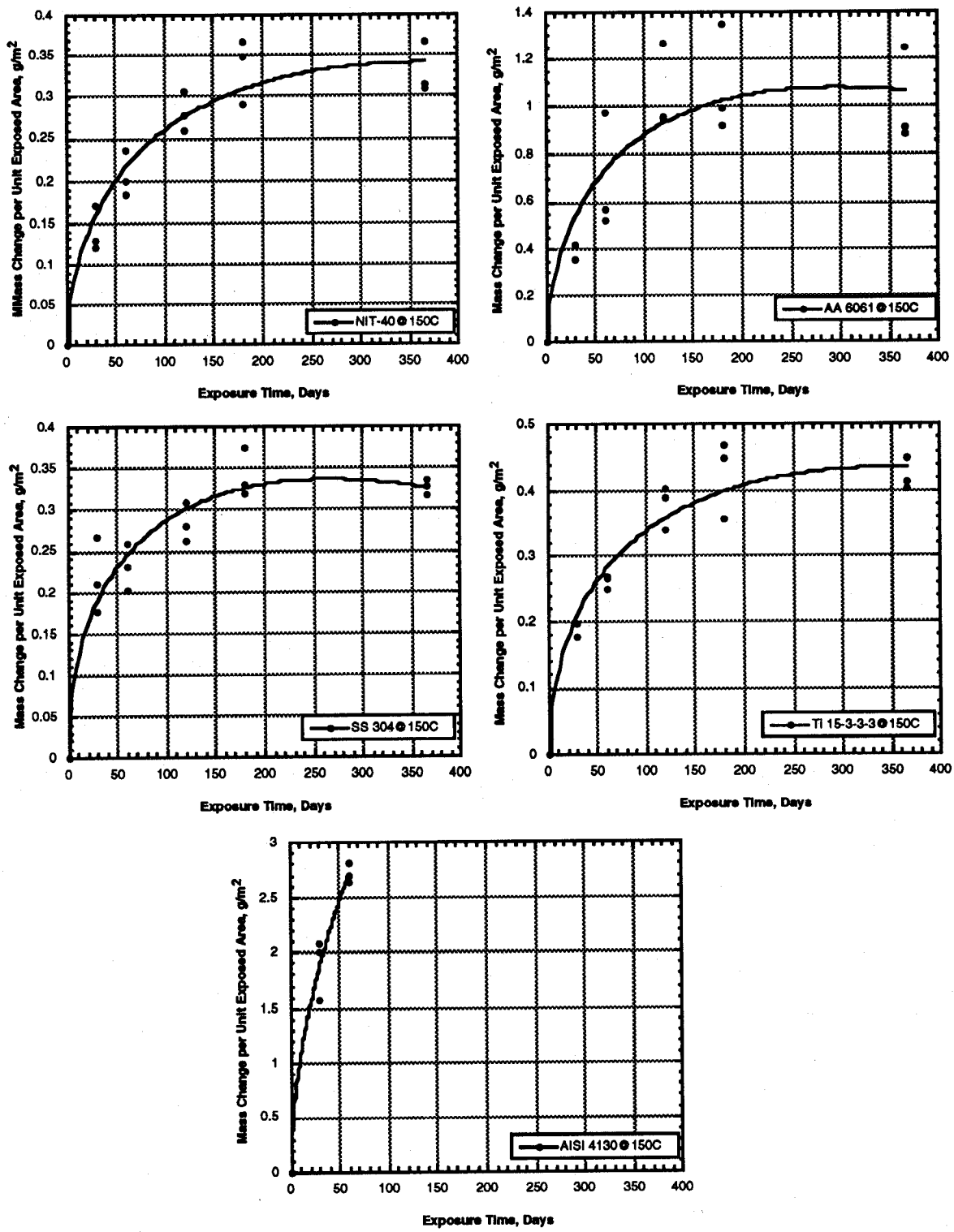

Figure 6. Mass change versus exposure time in halon 1301 at 150 °C.

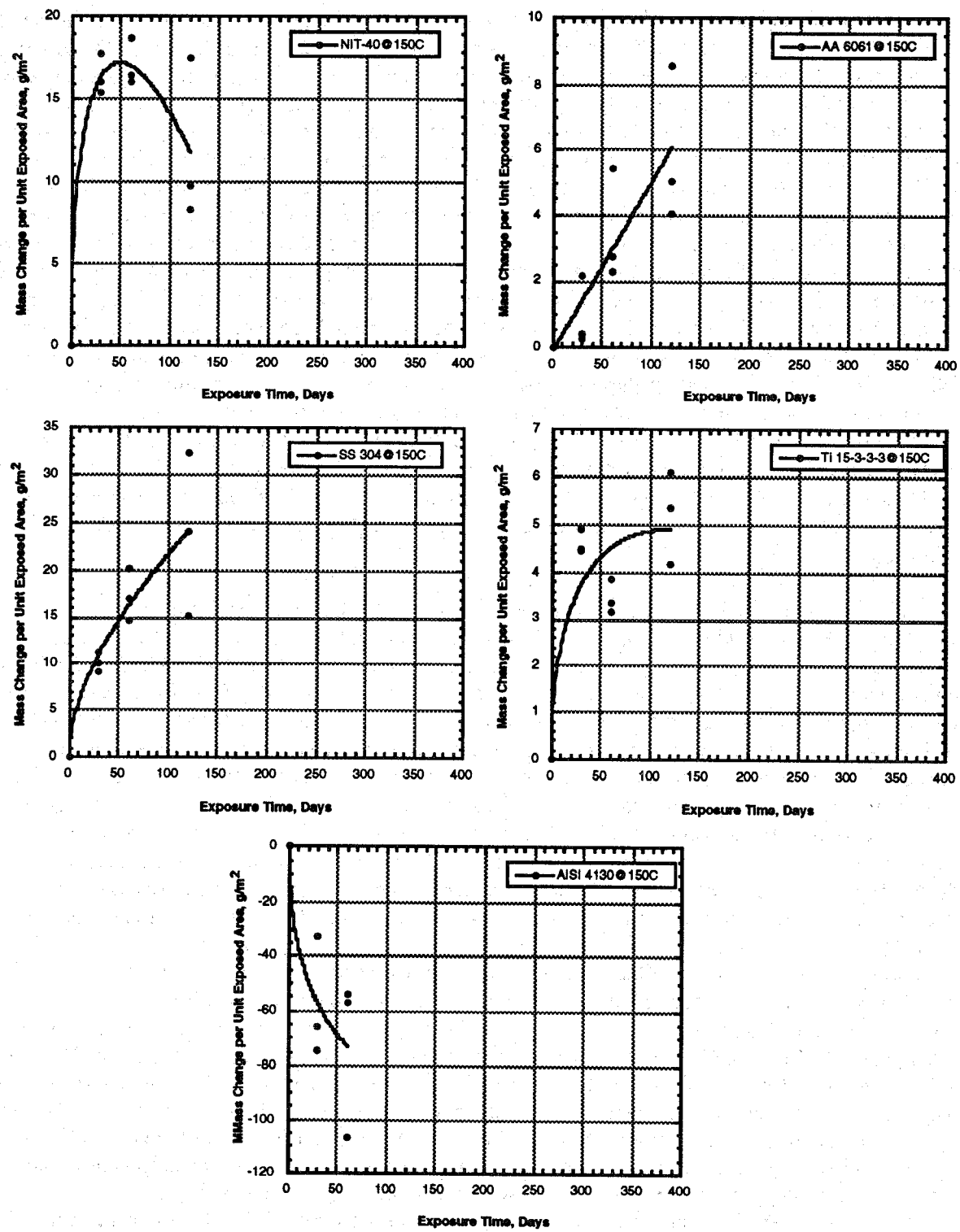

Figure 7. Mass change versus exposure time in CF_3I at 150 °C.

As with the Phase I results, the evaluation of the relative performances of the alloy/agent combinations was hampered by the comparison of mass loss and mass gain measurements in the same environment. Typically, mass loss measurements are evaluated by assuming that all of the lost mass was the result of corrosion and that no corrosion products were left on the surface to generate errors in this determination. Then, the quantity of metal reacting and rate of the reactions can be calculated directly from the mass loss. Similarly, mass gain measurements can be evaluated if the reaction and the reaction product stoichiometry are known and it is assumed that none of the scale spalls off on the samples weighed before and after scale removal. For this study, descaling techniques were examined, but it was found that these techniques removed significant quantities of metal with respect to the magnitude of these measurements or did not remove the surface scales. For analysis of the relative corrosion behavior of the candidates, it is assumed that the relative magnitudes of the mass changes are proportional to the corrosion rates of the different alloy/agent combinations. It should be noted that the electrochemical measurements are the only means available for checking this assumption.

Visual inspections were also conducted on immersion test coupons. Those results are presented in Table 6. The attack observed on these coupons was relatively minor in nature and mainly consisted of staining and/or discolorations, but some pitting was observed. The observed staining may be an indication of general corrosion but this form of corrosion could not be distinguished from these measurements. CF_3I, again, appeared to be the most aggressive of the agents at 150 °C since pitting was observed in every alloy except for Nitronic 40 stainless steel. The 4130 alloy steel exhibited some slight pitting in every environment except for in the CF_3I where the most severe pitting was observed.

5.2.5 Results at 20 °C. The mass change rate, estimated for each alloy/environment combination using the same relationships from the 150 °C analyses, are presented in Table 7. As expected, the magnitudes of these values are much smaller at ambient temperature than at 150 °C. Similar linear regressions were also performed on these data. Table 8 shows the results of the mass versus simple time regression where m, the slope, is the estimated mass change rate, and R is the correlation coefficient. The standard error, again is the estimated standard deviation of the mass change rate values. The correlations at this temperature were somewhat better than those at 150 °C, but once again, the scatter resulting from the loss of surface films had a large influence. The worst value (< 0.1) occurred in the Al-6061 in CF_3I. The second regression, ($\Delta M/A = k(t)^{1/2}$) produced slightly better results (Table 9), but once again, the correlations were not encouraging. As in the case with the 150 °C data, the correlation coefficients of this regression demonstrate that the mass changes at 20 °C also followed a combined linear and $t^{1/2}$ dependence. The results of this regression are shown in Table 10.

The mass change data from the experiments performed at ambient temperatures are presented in similar fashion to those performed at 150 °C and the corresponding curves from the multiple regression are once again included with the data. The raw data used for these analyses are presented in Appendix B. Figures 8-12 are the mass change per unit exposed area for each alloy in FC-218, HFC-227ea, HFC-125, halon 1301 and CF_3I respectively. The magnitudes of the mass changes observed at ambient temperature were significantly smaller than those observed at 150 °C. These large variations are particularly evident in the aluminum data. The CF_3I did not appear to be as aggressive an environment at ambient temperature as it was at 150 °C. At this temperature, the mass changes appear to be due to the formation, growth and spalling of surface scales.

Visual inspections were also conducted on the coupons tested at 20 °C (Table 11). As in the case of the evaluation performed on the coupons tested at 150 °C, the attack observed on these coupons was relatively minor in nature and mainly consisted of staining. Some pitting was observed but, it was generally less severe at 20 °C. While the 6061-T6 aluminum alloy did not exhibit any

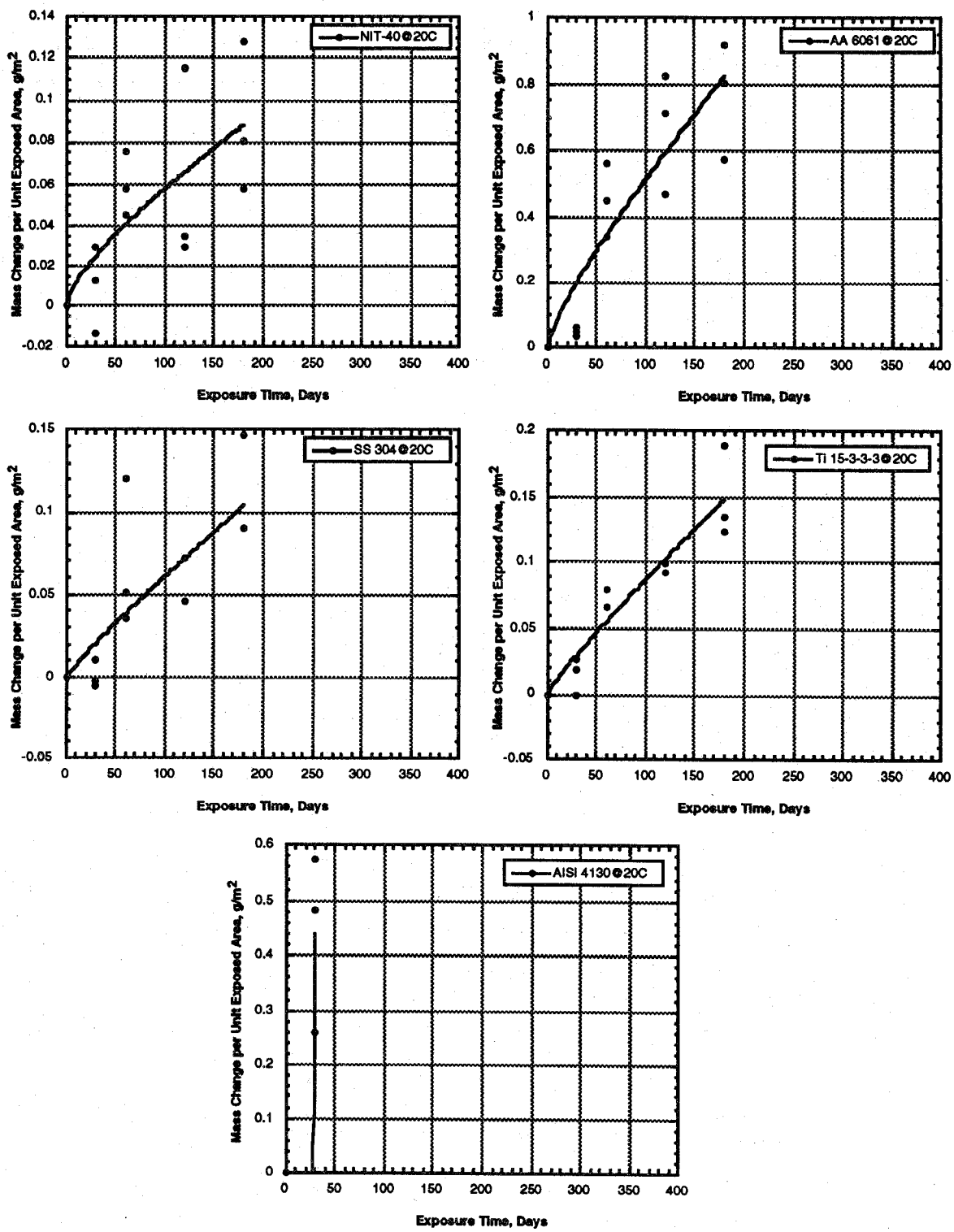

Figure 8. Mass change versus exposure time in FC-218 at 20 °C.

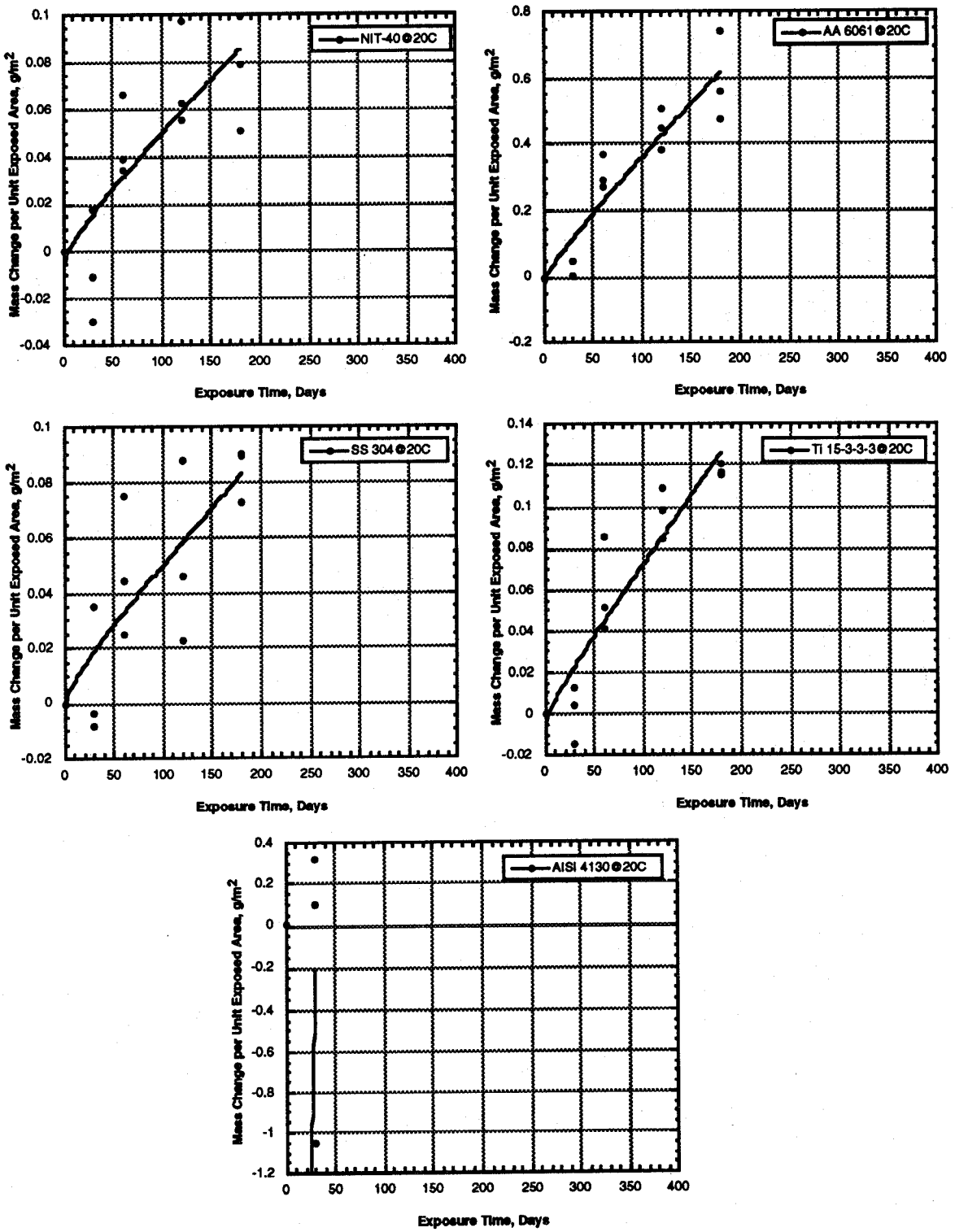

Figure 9. Mass change versus exposure time in HFC-227ea at 20 °C.

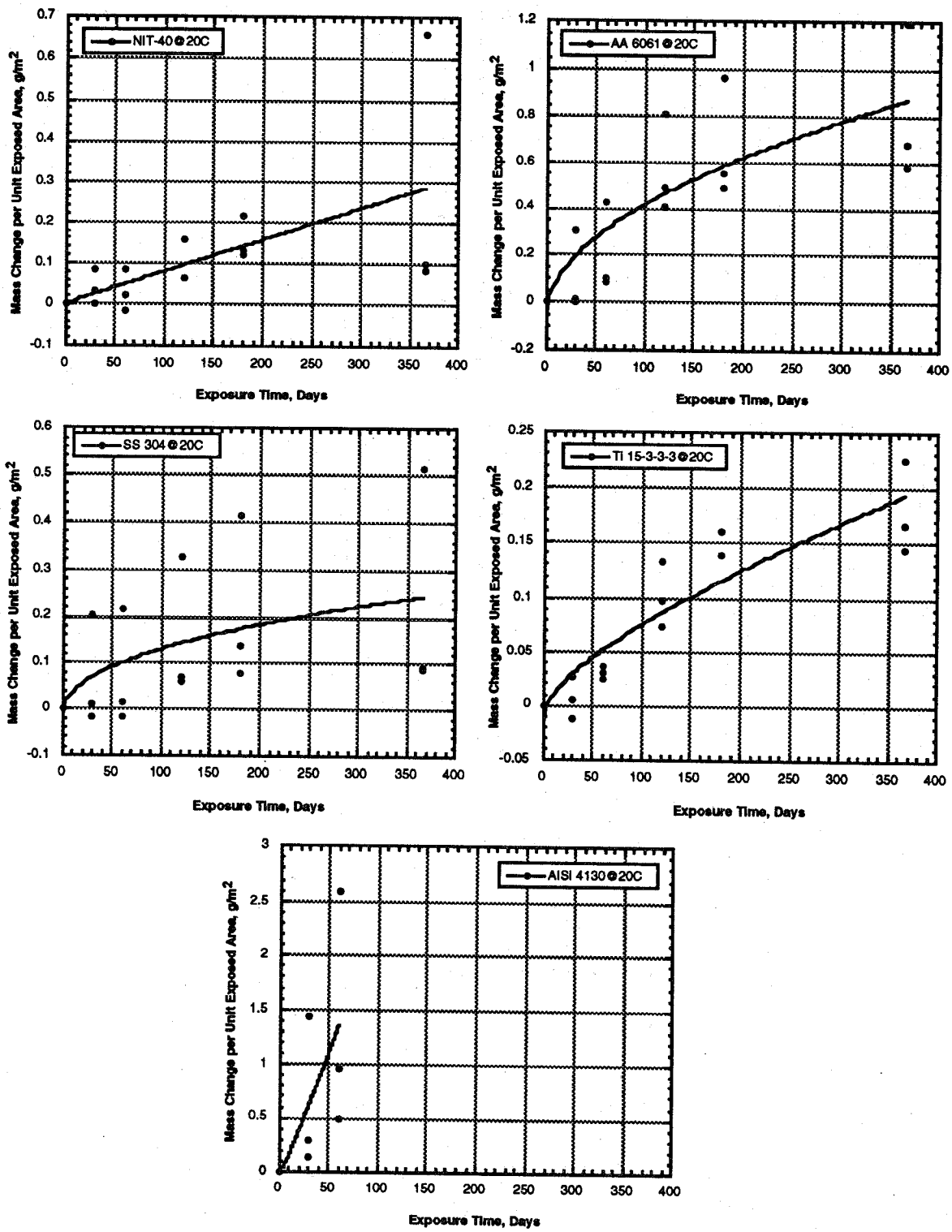

Figure 10. Mass change versus exposure time in HFC-125 at 20 °C.

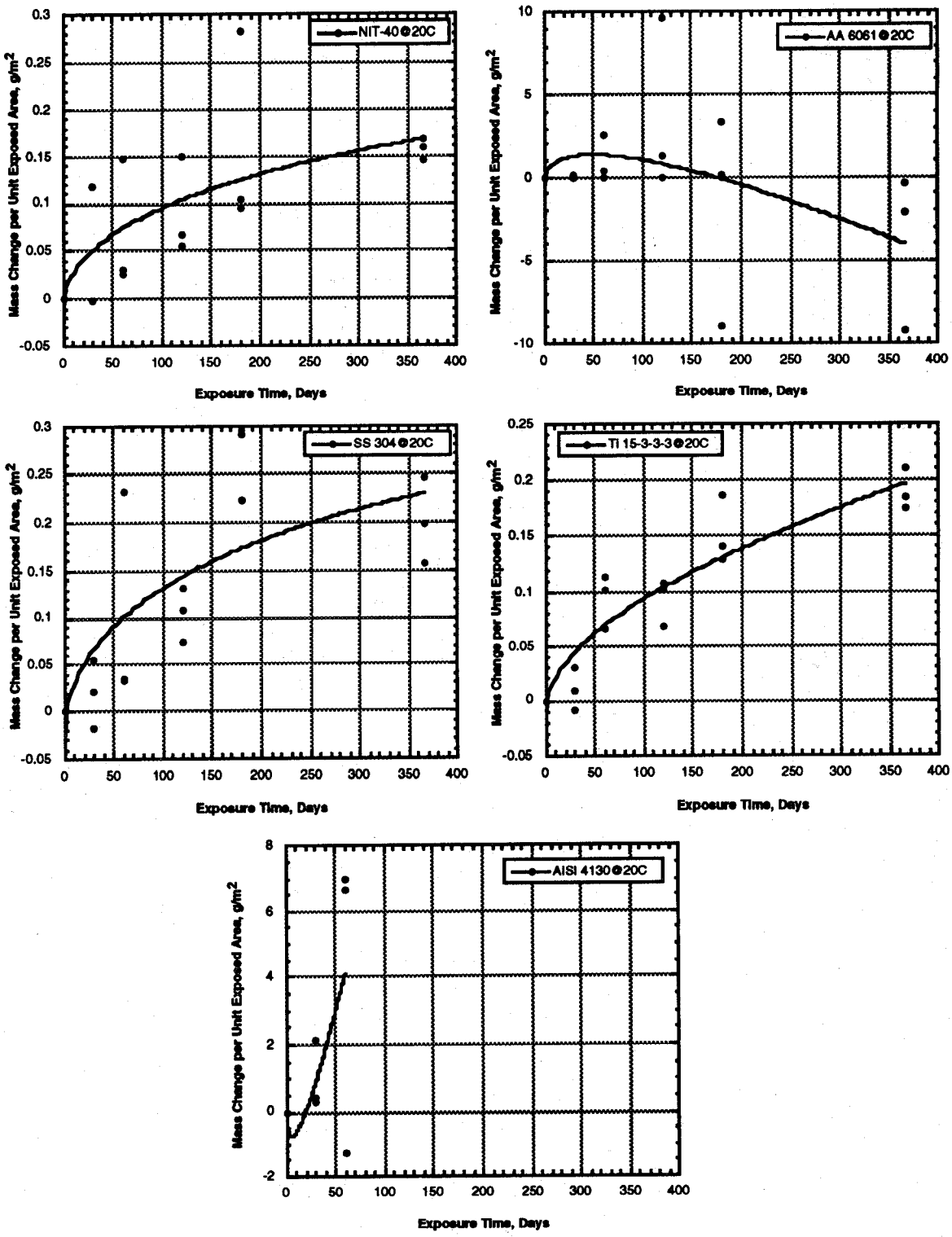

Figure 11. Mass change versus exposure time in halon 1301 at 20 °C.

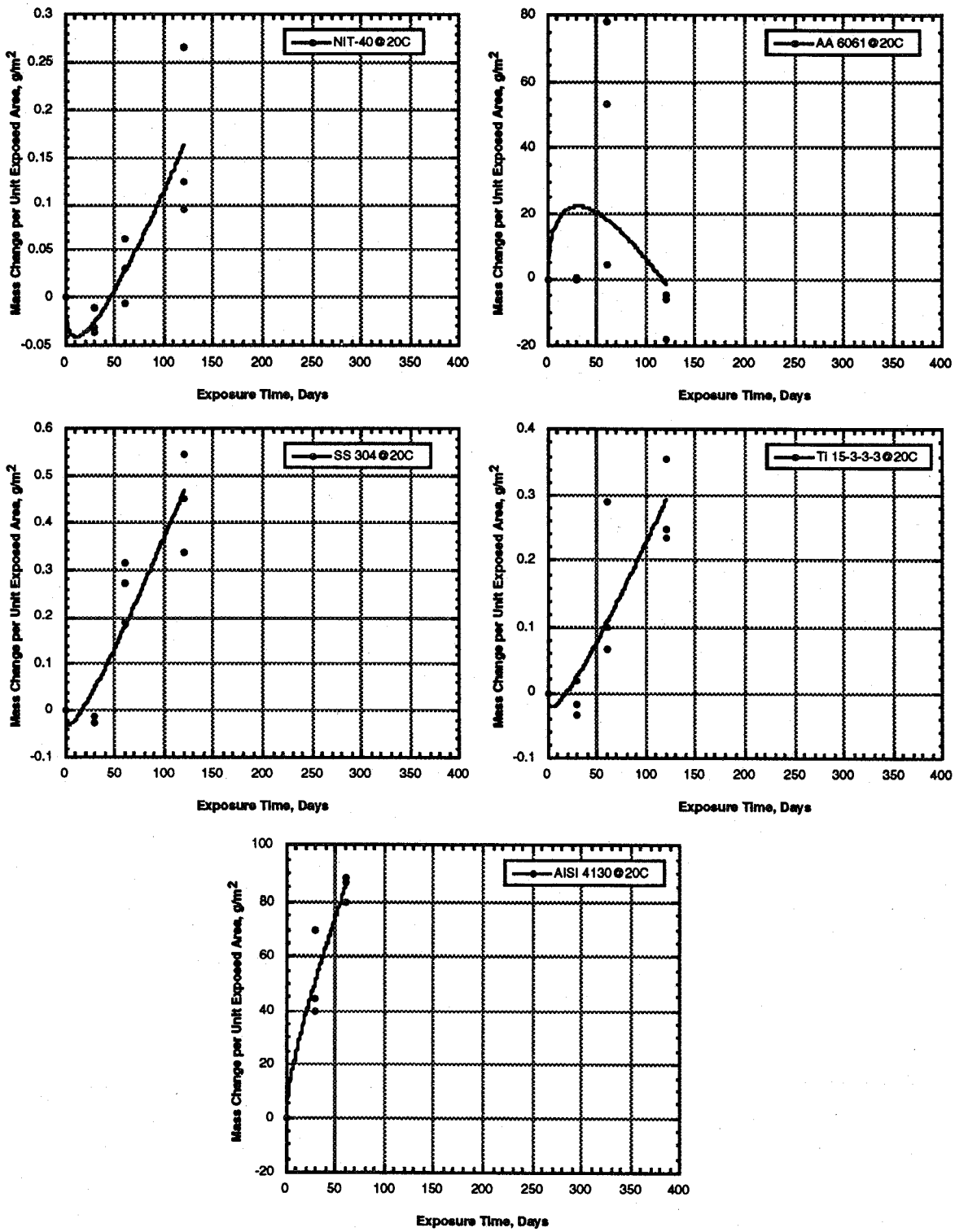

Figure 12. Mass change versus exposure time in CF_3I at 20 °C.

Table 6. Results of visual inspection of coupons tested at 150 °C

Alloy	HFC-125	HFC-227ea	Halon 1301	FC-218	CF_3I
Nit 40	0	0	0	0	0
Al 6061-T6	0	0	0	0	1
304 SS	0	0	0	0	2
Ti 15-3-3-3	0	0	0	0	1
AISI 4130	1	2	1	1	3
321 SS	0	*	0	*	*
CDA-110	0	*	0	*	*
CDA-172	0	*	0	*	*
AM 355	0	*	0	*	*
Inconel 615	0	*	0	*	*

(0) No visual evidence attack
(1) Average observed pit depth < 0.06 mm
(2) Average observed pit depth between 0.06 mm and 0.1 mm
(3) Average observed pit depth > 0.1 mm
(*) Alloy not tested in this environment

Table 7. Mass change rate per unit area (g/meter^2 · day) at 20 °C estimated from the mass change measurements divided by the exposure time and sample area. This analysis assumes the reaction rate does not vary with time (bare surface kinetics)

Alloy	HFC-125		HFC-227ea		Halon 1301		FC-218		CF_3I	
	R	Std Dev	R	Std Dev	R	Std Dev	R	Std Dev	R	Std Dev
Nit 40	0.00084	0.00078	0.00039	0.00055	0.00090	0.00106	0.00057	0.00046	0.00031	0.00110
Al 6061-T6	0.00354	0.00277	0.00322	0.00183	0.00548	0.02867	0.00474	0.00253	0.22589	0.50962
304 SS	0.00128	0.00190	0.00049	0.00045	0.00104	0.00099	0.00056	0.00055	0.00248	0.00238
Ti 15-3-3-3	0.00058	0.00036	0.00062	0.00046	0.00080	0.00052	0.00084	0.00036	0.00149	0.00182
AISI 4130	0.00974	0.00884	-0.00352	0.01229	0.02156	0.02336	0.00731	0.00271	0.71189	0.23330
321 SS	0.00030	0.00027	*	*	0.00069	0.00010	*	*	*	*
CDA 110	0.00039	0.00073	*	*	0.00140	0.00078	*	*	*	*
CDA 172	0.00006	0.00058	*	*	-0.00020	0.00031	*	*	*	*
AM 355	-0.00001	0.00077	*	*	0.00022	0.00047	*	*	*	*
IN 625	0.00004	0.00012	*	*	0.00016	0.00015	*	*	*	*

(+) Values mean mass increase (scaling)
(-) Values mean mass decrease (corrosion)
* No measurement made in the agent for this alloy
R = Average mass change rate (g/meter^2 · day)

Table 8. Mass change rate per unit area (g/meter^2 · day) at 20 °C estimated by the regression slope for a linear regression of mass change per unit area on exposure time(assumes constant, bare surface, reaction kinetics)

Alloy	HFC-125			HFC-227ea			Halon 1301		
	m	R	Std Err	m	R	Std Err	m	R	Std Err
Nit 40	0.00078	0.637	0.00023	0.00049	0.825	0.00009	0.00042	0.660	0.00012
Al 6061-T6	0.00229	0.791	0.00044	0.00348	0.934	0.00037	0.01262	0.389	0.00748
304 SS	0.00061	0.495	0.00027	0.00046	0.824	0.00009	0.00060	0.691	0.00016
Ti 15-3-3-3	0.00053	0.900	0.00006	0.00071	0.934	0.00008	0.00051	0.886	0.00007
AISI 4130	0.00894	0.664	0.00380	-0.00352	0.241	0.00709	0.02791	0.603	0.01395
321 SS	‡	‡	‡	*	*	*	‡	‡	‡
CDA 110	‡	‡	‡	*	*	*	‡	‡	‡
CDA 172	‡	‡	‡	*	*	*	‡	‡	‡
AM 355	‡	‡	‡	*	*	*	‡	‡	‡
IN 625	‡	‡	‡	*	*	*	‡	‡	‡

Table 8. (continued)

Alloy	FC-218			CF_3I		
	m	R	Std Err	m	R	Std Err
Nit 40	0.00048	0.753	0.00012	0.00149	0.798	0.00036
Al 6061-T6	0.00459	0.900	0.00062	0.03963	0.066	0.18881
304 SS	0.00058	0.800	0.00012	0.00409	0.919	0.00055
Ti-15-3-3-3	0.00082	0.944	0.00008	0.00257	0.860	0.00048
AISI 4130	0.00731	0.920	0.00156	0.55297	0.949	0.06940
321 SS	*	*	*	*	*	*
CDA 110	*	*	*	*	*	*
CDA 172	*	*	*	*	*	*
AM 355	*	*	*	*	*	*
IN 625	*	*	*	*	*	*

* No measurements were made in this alloy/environment combination

‡ Only one exposure time used for these measurements, see the average mass change rate table

m = estimated mass change rate for linear regression of mass change per unit area on exposure times (g/meter^2 · day)

R = correlation coefficient for linear regression

Std Error = estimated standard deviation for the mass change rate (regression slope)

Table 9. Mass change rate per unit area (g/meter^2 · day) at 20 °C estimated by the slope for a linear regression of mass change per unit area on square root of the exposure time (assumes a uniformly filmed surface)

Alloy	HFC-125			HFC-227ea			Halon 1301		
	k	R	Std Err	k	R	Std Err	k	R	Std Err
Nit 40	0.01491	0.602	0.00494	0.00696	0.823	0.00133	0.00922	0.714	0.00226
Al 6061-T6	0.04856	0.829	0.00818	0.04711	0.907	0.00606	-0.18978	0.289	0.01570
304 SS	0.01331	0.530	0.00532	0.00622	0.809	0.00126	0.01327	0.761	0.02820
Ti 15-3-3-3	0.01084	0.913	0.00121	0.00965	0.904	0.00126	0.01078	0.925	0.00110
AISI 4130	0.10716	0.654	0.04691	-0.02725	0.241	0.05492	0.31117	0.552	0.17774
321 SS	‡	‡	‡	*	*	*	‡	‡	‡
CDA 110	‡	‡	‡	*	*	*	‡	‡	‡
CDA 172	‡	‡	‡	*	*	*	‡	‡	‡
AM 355	‡	‡	‡	*	*	*	‡	‡	‡
IN 625	‡	‡	‡	*	*	*	‡	‡	‡

Table 9. (continued)

Alloy	FC-218			CF_3I		
	k	R	Std Err	k	R	Std Err
Nit 40	0.00688	0.766	0.00160	0.01350	0.663	0.00483
Al 6061-T6	1.63021	0.894	1.63021	0.46755	0.070	2.09612
304 SS	0.00785	0.776	0.00177	0.04108	0.831	0.00869
Ti 15-3-3-3	0.01113	0.917	0.00135	0.02562	0.772	0.00668
AISI 4130	0.05658	0.920	0.01209	6.92014	0.975	0.59885
321 SS	*	*	*	*	*	*
CDA 110	*	*	*	*	*	*
CDA 172	*	*	*	*	*	*
AM 355	*	*	*	*	*	*
IN 625	*	*	*	*	*	*

* No measurements were made in this alloy/environment combination

‡ Only one exposure time used for these measurements, see the average mass change rate table

k = estimated mass change rate for linear regression of the mass change per unit area on square root of exposure time (g/meter^2 · day$^{1/2}$)

R = correlation coefficient for linear regression

Std Error = estimated standard deviation for the mass change rate (regression slope)

Table 10. Mass change rates at 150 °C for a regression model that assumes mixed bare and filmed surface kinetics

HFC-125

Alloy	M_0	M_0(error)	M_1	M_1(error)	M_2	M_2(error)	R
Nit 40	0.00035	0.06907	0.00075	0.00076	0.00047	0.01533	0.637
Al 6061-T6	-0.05633	0.11893	0.00014	0.00131	0.04588	0.02640	0.830
304 SS	-0.00965	0.07734	-9.53e-5	0.00085	0.01513	0.01716	0.531
Ti-15-3-3-3	-0.01411	0.01693	0.00020	0.00019	0.00700	0.00376	0.920
AISI 4130	1.05e-10	0.4376	0.02643	0.04432	-0.03015	0.33373	0.666
321 SS	‡	‡	‡	‡	‡	‡	‡
CDA 110	‡	‡	‡	‡	‡	‡	‡
CDA 172	‡	‡	‡	‡	‡	‡	‡
AM 355	‡	‡	‡	‡	‡	‡	‡
IN 625	‡	‡	‡	‡	‡	‡	‡

Table 10. (continued)

Halon 1301

Alloy	M_0	M_0(error)	M_1	M_1(error)	M_2	M_2(error)	R
Nit 40	-0.00814	0.03247	-0.00012	0.00036	0.01154	0.00721	0.720
Al 6061-T6	-0.39446	2.1183	-0.03640	0.02326	0.50713	0.47012	0.461
304 SS	-0.02406	0.04067	-0.00026	0.00045	0.01815	0.00903	0.767
Ti-15-3-3-3	-0.00970	0.01602	5.18e-5	0.00018	0.00978	0.00355	0.926
AISI 4130	7.29e-15	1.593	0.15669	0.157	-0.68495	1.1102	0.614
321 SS	‡	‡	‡	‡	‡	‡	‡
CDA 110	‡	‡	‡	‡	‡	‡	‡
CDA 172	‡	‡	‡	‡	‡	‡	‡
AM 355	‡	‡	‡	‡	‡	‡	‡
IN 625	‡	‡	‡	‡	‡	‡	‡

Table 10. (continued)

FC-218

Alloy	M_0	M_0(error)	M_1	M_1(error)	M_2	M_2(error)	R
Nit 40	-0.00226	0.01695	0.00022	0.00039	0.00378	0.00545	0.764
Al 6061-T6	-0.03239	0.08801	0.00268	0.00203	0.02799	0.02829	0.908
304 SS	-0.00210	0.01788	0.00047	0.00041	0.00154	0.00575	0.801
Ti-15-3-3-3	-0.00205	0.01165	0.00067	0.00027	0.00225	0.00374	0.946
AISI 4130	n/a	n/a	n/a	n/a	n/a	n/a	n/a
321 SS	*	*	*	*	*	*	*
CDA 110	*	*	*	*	*	*	*
CDA 172	*	*	*	*	*	*	*
AM 355	*	*	*	*	*	*	*
IN 625	*	*	*	*	*	*	*

Table 10. (continued)

HFC-227ea

Alloy	M_0	M_0(error)	M_1	M_1(error)	M_2	M_2(error)	R
Nit 40	-0.00502	0.01389	0.00037	0.00032	0.00177	0.00447	0.827
Al 6061-T6	-0.01883	0.05417	0.00280	0.00125	0.00987	0.01742	0.936
304 SS	-0.00142	0.01276	0.00032	0.00030	0.00194	0.00410	0.828
Ti-15-3-3-3	-0.00467	0.01119	0.00060	0.00026	0.00172	0.00360	0.935
AISI 4130	n/a	n/a	n/a	n/a	n/a	n/a	n/a
321 SS	*	*	*	*	*	*	*
CDA 110	*	*	*	*	*	*	*
CDA 172	*	*	*	*	*	*	*
AM 355	*	*	*	*	*	*	*
IN 625	*	*	*	*	*	*	*

Table 10. (continued)

CF_3I

Alloy	M_0	M_0(error)	M_1	M_1(error)	M_2	M_2(error)	R
Nit 40	-0.00019	0.0267	0.00353	0.00098	-0.02389	0.01083	0.874
Al 6061-T6	-3.2761	15.868	-0.83038	0.57971	9.2353	6.4376	0.436
304 SS	-0.00955	0.04828	0.00597	0.00176	-0.0220	0.01959	0.929
Ti-15-3-3-3	-0.00551	0.04308	0.00392	0.00157	-0.0159	0.01718	0.872
AISI 4130	1.21e-10	5.605	0.71758	0.56594	5.443	4.232	0.9706
321 SS	*	*	*	*	*	*	*
CDA 110	*	*	*	*	*	*	*
CDA 172	*	*	*	*	*	*	*
AM 355	*	*	*	*	*	*	*
IN 625	*	*	*	*	*	*	*

* No measurements were made in this alloy/environment combination
‡ Only one exposure time used for these measurements, see the average mass change rate table.
m_0 = g/meter^2
m_1 = g/meter^2 · day
m_2 = g/meter^2 · day$^{1/2}$

Table 11. Results of visual inspection of coupons tested at 20 °C

Alloy	HFC-125	HFC-227ea	Halon 1301	FC-218	CF_3I
Nit 40	0	1	0	0	0
Al 6061-T6	1	1	3	0	0
304 SS	0	0	0	0	0
Ti 15-3-3-3	0	0	0	0	0
AISI 4130	3	1	1	1	3
321 SS	0	*	0	*	*
CDA-110	0	*	0	*	*
CDA-172	0	*	0	*	*
AM 355	0	*	0	*	*
Inconel 615	0	*	0	*	*

(0) No visual evidence attack observed
(1) Average observed pit depth < 0.06 mm
(2) Average observed pit depth between 0.06 mm and 0.1 mm
(3) Average observed pit depth > 0.1 mm
(*) Alloy not tested in this environment

pitting in the halon 1301 at 150 °C, it did however, exhibit some pitting in that agent at 20 °C. This result was unexpected and may be an indication that this alloy has some compatibility problems with the halon 1301. The 4130 alloy steel, once again, exhibited some pitting in every environment with the most severe pitting observed in the CF_3I.

5.3 Environmentally Induced Fracture Experiments (Slow Strain Rate Tensile Tests)

The environmentally induced fracture resistance of the alloys was evaluated by conducting exposure tests in each of the replacement candidates. This was accomplished by loading cylindrical tensile specimens of the alloys in tension, by a slow increase in the applied strain, until failure occurred by either a normal mechanical or an environmentally assisted means. Comparisons between the stresses and strains required to cause failure in an inert environment and in the agent at the same temperature provided a measure of the propensity for that agent to cause an environmentally induced failure.

5.3.1 Materials. The materials selected by the sponsors for Phase II were: 304 stainless steel, stainless steel alloy 21-6-9 (Nitronic 40), and beta-titanium alloy 15-3-3-3. These alloys were selected

because they are presently in service, or under consideration for future use, in the agent storage and distribution systems on board jet aircraft. The compositions of these alloys are also given in Table 1 (Section 5.2.1).

5.3.2 Experimental Procedure at 150 °C. The alloys were evaluated for stress corrosion cracking susceptibility in the replacement candidates by the slow strain rate (SSR) tensile test technique. This technique was selected because it generates intrinsic mechanical properties data for a given alloy and it also reveals any interactions that may have occurred between that alloy and the testing environment within a relatively short time frame (Ricker, 1994, Stoudt and Fink 1994, and Stoudt and Ricker, 1994).

All of the samples used for these experiments were machined with the tensile axis parallel to the rolling direction of the plate stock (Figure 13) and tested in the "as received" condition. The sample preparation consisted of a measurement of the appropriate quantities (e.g., gauge length) followed by degreasing in acetone and alcohol. The vessels used for these experiments were 250 ml volume autoclaves with a design similar to those used for the exposure testing, except that these vessels were modified so that load could be applied to the tensile specimen in-situ under constantly maintained environmental conditions as shown in Figure 14 (Ricker, 1994). The testing conditions used for this portion of the analysis were nominally 5.86 MPa at 150° ± 1 °C.

The test vessels were evacuated and charged with agent in the same manner as the exposure test vessels, but due to the reduced capacity of the test vessels, the appropriate mass was obtained by a calculation based on the ideal gas law. This approach was selected over the mass balance shown in Equation (1) (Section 5.2.2) for two reasons. First, the number of moles of gas could be held constant allowing for a consistent agent concentration for each test. Second, this model generated a slightly lower pressure in the cells reducing the risk of a rupture.

The mechanical tests were conducted using a computer controlled SSR testing system which operated at a constant crosshead speed of 2.54×10^{-8} m/s (1.0×10^{-6} in/s). The computer was configured to sample and record the applied load, the crosshead displacement and the elapsed time at 90 s intervals. After failure, the agent was released, the vessels were then allowed to cool to ambient temperature, and the samples were removed from the vessel and stored in a desiccator until analyzed.

The fracture surfaces were sectioned from the broken samples and prepared for analysis. The influence of the agents on the ductility of the alloys was determined from reduction in area (RA) measurements performed on the fracture surfaces with an optical measuring microscope with a $\pm 0.5 \times 10^{-6}$ m resolution. All samples were examined visually and scanning electron microscopy was performed on selected samples to verify the presence of stress corrosion cracking. The results of these experiments were used to assess the potential for failure by stress corrosion cracking for each of the alloys in a replacement candidate.

5.3.3 Experimental Procedure at 20 °C. A second series of slow strain rate tests was conducted at ambient conditions in order to determine the possible influences of the liquid phase and/or the meniscus regions on the stress corrosion cracking resistance of these materials. To do this, Equation (1) was utilized to determine an appropriate mass of agent so as to locate the liquid/vapor meniscus region at the approximate midpoint of the gauge section of the tensile specimen. The resulting cell pressures varied according to the density of each agent, but were on the order of 1.38 MPa at 20 ± 1 °C. The remainder of the procedure was identical to the one outlined in the previous section.

5.3.4 Results at 150 °C. Environmentally induced fracture is the initiation and/or propagation of a crack at stresses well below those normally required to cause fracture resulting from simultaneous

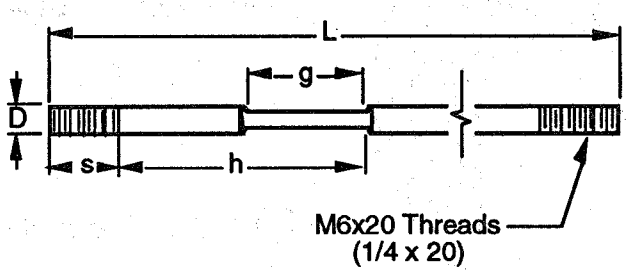

D = 19 mm (0.25 in)
L = 178 mm (7 in)
g = 25.4 mm (1 in)
h = 57 mm (2.25 in)
s = 19 mm (0.75 in)

Figure 13. Slow strain rate tensile sample design (ASTM E-8, G-49).

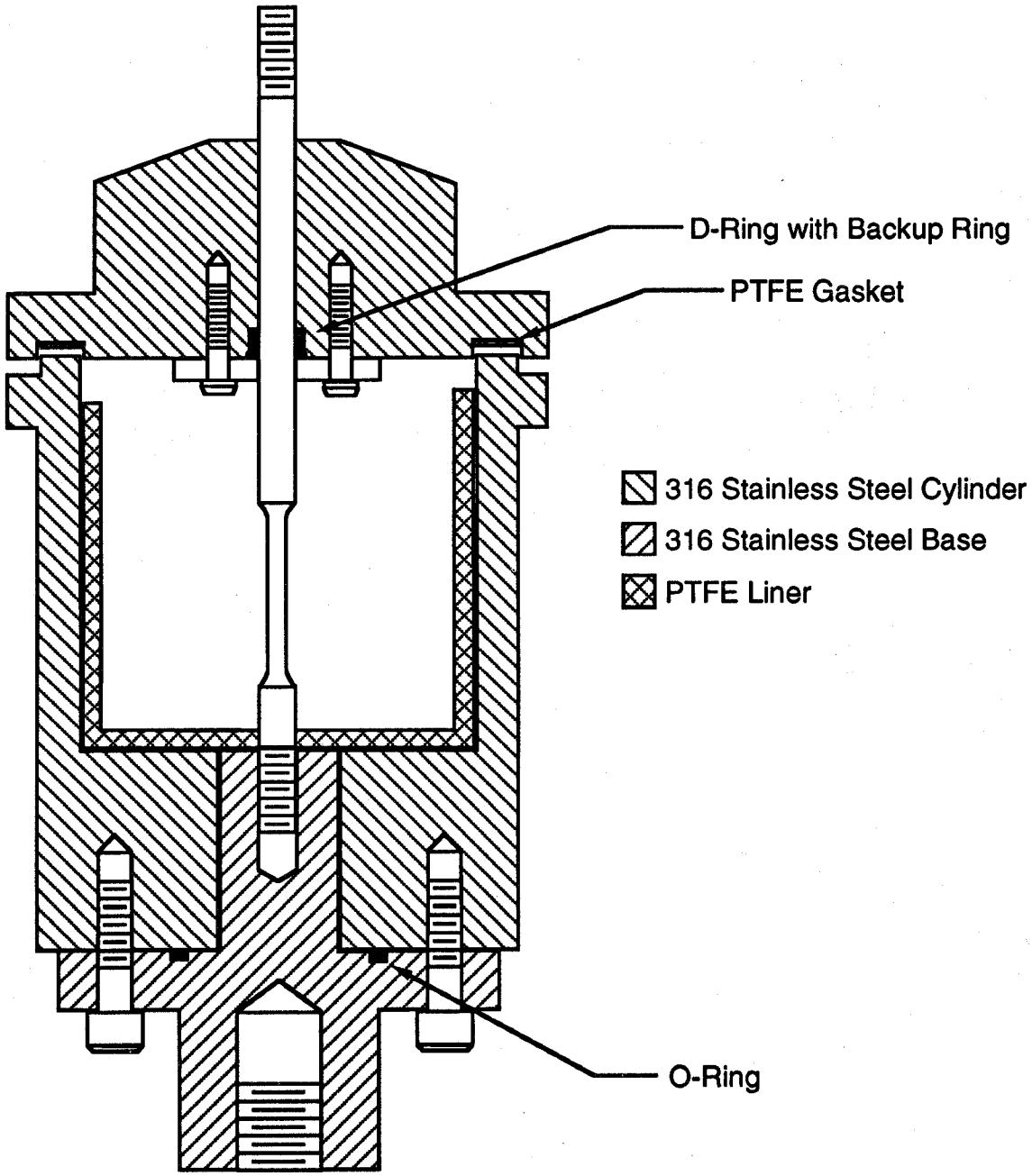

Figure 14. Schematic diagram of the slow strain rate test chamber.

exposure to a chemically reactive environment and a mechanical stress (Stoudt, 1995 and Stoudt, 1994). This particular form of corrosion occurs in specific material/environment combinations and while attack may not be readily apparent, failures can be sudden and catastrophic.

The same three parameters used to indicate the susceptibility of an alloy to environmentally induced failure used for Phase I were applied to the Phase II data. These are: the ultimate tensile strength (UTS), the strain to failure (ε_f), and the reduction in cross sectional area (RA) (Ricker, 1994).

The UTS is an indication of the fracture strength of the sample and it is determined from the maximum load observed during the tensile test according to the relationship:

$$\sigma_{UTS}=\frac{P_{max}}{A_o} \tag{6}$$

where P_{max} is the maximum load supported by the sample during the test and A_0 is the initial cross-sectional area of the gauge section of the sample (Deiter, 1986). If cracking, or some other environmental interaction that promotes crack initiation or propagation at lower stresses, occurs, it will produce a noticeable change in this parameter (Stoudt, 1994). Environmental interactions can also alter deformation processes on the surfaces and at tips of cracks formed in the sample. One of the two parameters used to measure the ductility is the engineering strain to failure (ε_f) which can be determined from the relationship:

$$\epsilon_f=\frac{[L_f-L_o]}{L_o} \tag{7}$$

where L_f is the total change in sample length during the experiment and L_0 is the initial gauge length (Deiter, 1986). This measurement includes both the elastic and plastic deformation components required to induce failure, which are measured by displacement gages located outside the environmental chamber increasing measurement errors. As a result, a ductility determination based solely on this quantity may contain significant experimental error. Another means for determining the ductility of a material is the reduction in area (RA). This quantity is obtained from physical measurements performed on the fracture surface after completion of the tensile test from the relationship:

$$RA=\frac{[A_f-A_o]}{A_o} \tag{8}$$

where A_f is the final cross-sectional area of the fracture surface and A_0 is the initial gauge section cross-sectional area (Deiter, 1986). Unlike the strain to failure (STF), the RA measurement only includes the plastic deformation component required to induce failure and does not include measurement errors which may have occurred during the time the cell was ascending to the test temperature. Therefore, this is a better measure of the environmental interactions. Typically, all three of these parameters are analyzed by forming a ratio of the value observed in the environment to the value observed in an inert reference environment, argon (Ar), (Ricker, 1994 and Stoudt *et al.*, 1994).

Another approach for analysis of this data is to estimate the statistical significance of the difference between the mean determined for the parameter in the inert reference environment and the mean determined for the agent (Ricker, 1994). This analysis consisted of the calculation of Student's t-statistic for the significance of the difference between the mean determined in each environment and

the mean for the same parameter and alloy tested in argon at the same temperature. This statistic is calculated from the relationship:

$$t = \left[\frac{(\bar{y}_{envir} - \bar{y}_{Ar})}{\sqrt{\left(\frac{s^2_{envir}}{n_{envir}} + \frac{s^2_{Ar}}{n_{Ar}} \right)}} \right] \tag{9}$$

where: $\bar{y}_{envir}$ is the mean of the tests in the agent, $\bar{y}_{Ar}$ is the mean of the tests in argon, S_{envir} is the variance of the tests conducted in the agent, S_{Ar} is the variance of the tests conducted in argon, n_{envir} is the number of samples tested in the agent, and n_{Ar} is the number of samples tested in argon all at the same temperature (Mendenhall, 1992).

Table 12 gives the average UTS determined for each alloy in argon at 150 °C, and in each agent at 150 °C. The standard deviations for these calculated values are presented in Table 13. The ratio of the average UTS in each agent to the average UTS in argon at the same temperature is given in Table 14. In this table, it can be seen that 18 of the 20 agent/alloy combinations have a higher average UTS values in the agent than in argon.

Table 15 contains the results of a t-test estimate of the statistical significance of the observed differences using the alloy standard deviations. For a confidence level of 99.5 %, t determined in this manner (4 degrees of freedom) should be less than -4.60 to conclude that the environment significantly reduced the strength or ductility of the alloy. Similarly, a value greater than +4.60 would indicate a significant increase in strength or ductility caused by the environment. Values between -4.60 and +4.60 are considered statistically insignificant. A significant decrease in the average UTS may be an indication of cracking, but it could also be the result of corrosion reactions which reduced effective cross-section or otherwise assisting deformation. An increase in the average UTS is unusual and this may suggest that sample/environment interactions are inhibiting deformation and fracture, but it could also be an indication of an interference between the corrosion products being generated on the sample and the seal of the autoclave through which the sample must slide. The most important point is that no agent caused statistically significant changes in all of the alloys which demonstrates that suitable materials can be identified for the containment of any of these candidates (Ricker, 1994).

The ductility results for the 150 °C SSR tests are given in Tables 16 and 17. Table 16 gives the average strain to failure for each alloy/environment combination, and in argon at 150 °C. Table 17 shows the standard deviations for the STF calculations. The ratio of the average strain to failure for each alloy in each environment to that observed in the same alloy in argon at the same temperature is presented in Table 18. The significance of the difference is again presented as a function of the alloy standard deviations in Table 19. Environmental induced cracking, or stress corrosion cracking (SCC), is usually evidenced by a reduction in ductility. In Table 18, it can be seen that strain to failure ratio generally increased for Nitronic 40 and for 304 stainless for most of the alloy/environment combinations. The titanium 15-3-3-3 alloy demonstrated significant decreases in ductility for all of the environments. This is best reflected in the CF_3I data. The sharp decrease in the ductility was the result of severe cracking which was observed on two of the three specimens tested in this agent. However, these strain to failure measurements are based on load frame displacement measurements taken by a transducer positioned outside the autoclave during the experiment. As a result, the reduction in area measurements, which are based on measurements performed on the fracture surface with an optical microscope after the experiment, are a more reliable indication of changes in ductility.

Table 20 presents the RA data for each alloy in argon gas at 150 °C and each agent at 150 °C. Table 21 gives the standard deviations for these measurements. The ratio of the average reduction in

Table 12. Average ultimate tensile strength at 150 °C (MPa)

Environment	Nitronic 40	304 SS	Titanium 15-3-3-3
Argon	599	649	497
Halon 1301	603	671	497
FC-218	602	646	504
HFC-227ea	611	655	534
HFC-125	611	651	552
CF_3I	607	657	505

Table 13. Standard deviation of the ultimate tensile strength measurements at 150 °C (MPa)

Environment	Nitronic 40	304 SS	Titanium 15-3-3-3
Argon	1.5	0.6	6.0
Halon 1301	2.3	1.5	3.4
FC-218	3.7	0.8	4.7
HFC-227ea	4.8	2.0	5.7
HFC-125	3.6	2.4	2.0
CF_3I	0.9	2.0	2.2

Table 14. Ultimate tensile strength ratios at 150 °C [(UTS in Agent)/(UTS in Ar)]

Environment	Nitronic 40	304 SS	Titanium 15-3-3-3
Argon	*	*	*
Halon 1301	1.007	1.035	1.000
FC-218	1.005	0.996	1.015
HFC-227ea	1.021	1.010	1.076
HFC-125	1.020	1.003	1.112
CF_3I	1.013	1.012	1.017

Table 15. t-Test for significance in UTS change at 150 °C

Environment	Nitronic 40	304 SS	Titanium 15-3-3-3
Argon	*	*	*
Halon 1301	0.281	2.109	0.003
FC-218	0.226	-0.224	0.276
HFC-227ea	0.809	0.582	1.377
HFC-125	0.776	0.198	2.035
CF_3I	0.514	0.745	0.304

Table 16. Average strain to failure at 150 °C (%)

Environment	Nitronic 40	304 SS	Titanium 15-3-3-3
Argon	43.0	17.2	6.6
Halon 1301	44.9	18.1	5.7
FC-218	43.8	16.9	6.1
HFC-227ea	43.7	17.0	5.9
HFC-125	43.1	17.2	6.0
CF_3I	41.7	18.1	3.8

Table 17. Standard deviation of the strain to failure measurements at 150 °C (%)

Environment	Nitronic 40	304 SS	Titanium 15-3-3-3
Argon	0.5	2.3	1.9
Halon 1301	3.8	1.7	0.8
FC-218	2.6	1.5	0.8
HFC-227ea	2.1	0.6	0.6
HFC-125	1.0	0.4	0.6
CF_3I	1.0	4.0	2.5

Table 18. Strain to failure ratios at 150 °C [(STF in Agent)/(STF in Ar)]

Environment	Nitronic 40	304 SS	Titanium 15-3-3-3
Argon	*	*	*
Halon 1301	1.045	1.056	0.871
FC-218	1.019	0.986	0.927
HFC-227ea	1.018	0.991	0.899
HFC-125	1.004	1.000	0.912
CF_3I	0.972	1.056	0.571

Table 19. t-Test for significance in STF change at 150 °C

Environment	Nitronic 40	304 SS	Titanium 15-3-3-3
Argon	*	*	*
Halon 1301	1.119	0.619	-0.695
FC-218	0.464	-0.159	-0.394
HFC-227ea	0.457	-0.098	-0.543
HFC-125	0.098	-0.005	-0.472
CF_3I	-0.712	0.623	-2.312

Table 20. Average reduction in area at 150 °C (%)

Environment	Nitronic 40	304 SS	Titanium 15-3-3-3
Argon	77.6	75.0	54.8
Halon 1301	80.2	68.4	56.2
FC-218	80.5	68.4	58.5
HFC-227ea	79.2	68.2	55.7
HFC-125	68.2	80.9	54.0
CF_3I	79.4	66.6	44.9

Table 21. Standard deviation of the reduction in area measurements at 150 °C (%)

Environment	Nitronic 40	304 SS	Titanium 15-3-3-3
Argon	2.4	0.7	7.2
Halon 1301	1.2	0.7	3.2
FC-218	0.7	1.5	8.4
HFC-227ea	1.1	0.9	2.7
HFC-125	0.9	0.5	3.6
CF_3I	0.4	2.4	29.9

area measured for each alloy/agent combination to argon at 150 °C is presented in Table 22. The statistical significance of the difference is again presented as a function of the alloy standard deviations in Table 23. In Table 22, it can be seen that the reduction in area values for Nitronic 40 increase in every agent except for HFC-125, while 304 stainless has the opposite behavior. The titanium alloy performed well in halon 1301, FC-218 and HFC-227ea, but exhibited significantly lower values in HFC-125 and in CF_3I.

In general, each alloy performed well in one or more of the agents evaluated at 150 °C and the titanium alloy exhibited brittle cracking in two of the three samples tested in the CF_3I. Figure 15 is a low magnification scanning electron micrograph exhibiting the crack morphology observed in the titanium 15-3-3-3 samples tested in CF_3I at 150 °C. In this figure it can be seen that the entire fracture surface consists of brittle, transgranular cleavage cracks, which indicates this alloy has a strong sensitivity to this agent (Mills, 1987). Figure 16 is a higher magnification view of the observed cracking. This cracking could be the result of interactions between the titanium alloy and one or more of the decomposition products on the CF_3I. However, it is also possible that this cracking may have been due to an interaction with an impurity present in the CF_3I. Figures 17 and 18 are scanning electron micrographs of the alloy tested in argon at the same temperature included for comparison. In these figures, it can be seen that the fracture surfaces are entirely composed of microvoid coalescence which indicates the failures occurred by completely ductile processes. Figure 18 is a higher magnification view of the microvoid coalescence (Korb, 1987, Mills, 1987, and Boyer, 1987). These figures indicate that the titanium alloy may not be a suitable alloy for the containment of CF_3I.

5.3.5 Results at 20 °C. The slow strain rate data from the tests conducted at 20 °C are presented in a fashion similar to those used for the 150 °C tests. Table 24 gives the average UTS determined for each alloy in argon at 20 °C, and in each agent at 20 °C. The standard deviations for these calculated values are presented in Table 25. The ratio of the average UTS in each agent to the average UTS in argon at the same temperature is given in Table 26. In this table, it can be seen that all of the 20 agent/alloy combinations have a higher average UTS in the agent than in argon.

Tables 27 contains the results of an estimate of the significance of the differences. As before, a significant increase in the average UTS is unusual and this suggests that sample/environment interactions are inhibiting deformation and fracture, but it could also be an indication of an interference between the corrosion products being generated on the sample and the seal of the autoclave through which the sample must slide. The most important point is, once again, suitable materials can be identified for the containment and reliable distribution of any of these candidates (Ricker, 1994).

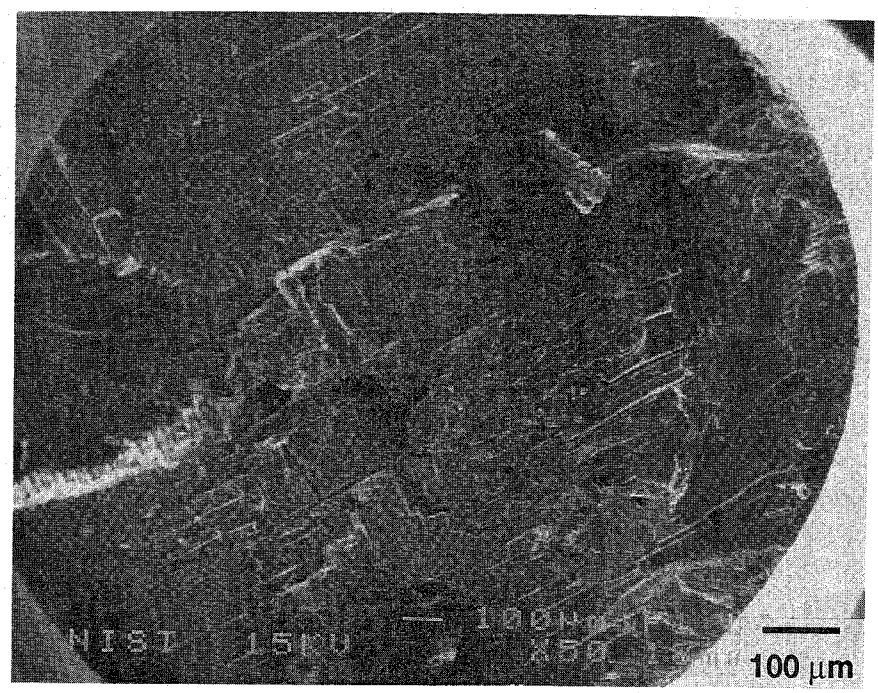

Figure 15. Scanning electron micrograph of the transgranular cleavage-like fracture observed in Ti 15-3-3-3 when tested in CF_3I at 150 °C.

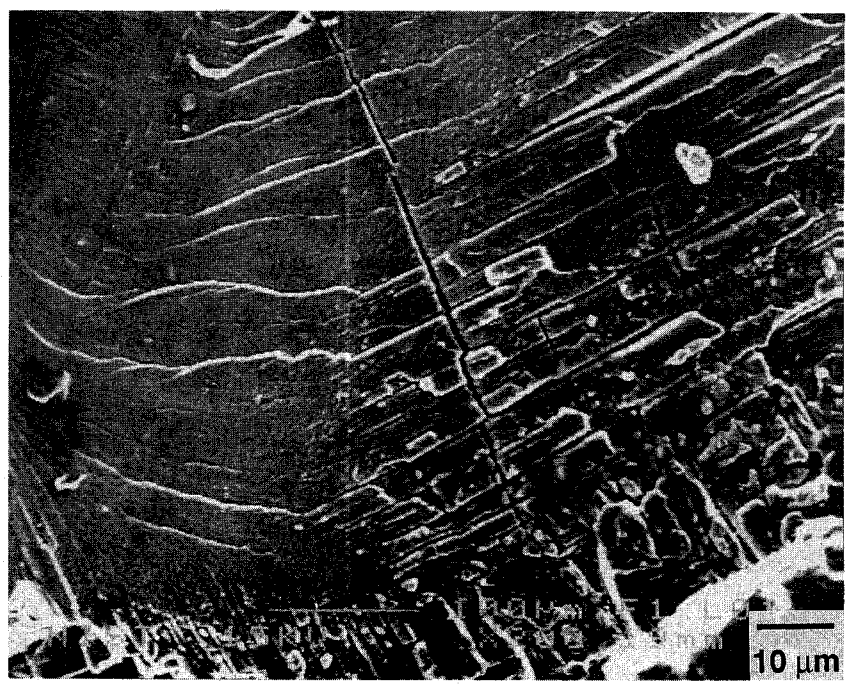

Figure 16. Higher magnification view of the transgranular cleavage-like crack morphology observed in titanium tensile specimen tested in CF_3I at 150 °C.

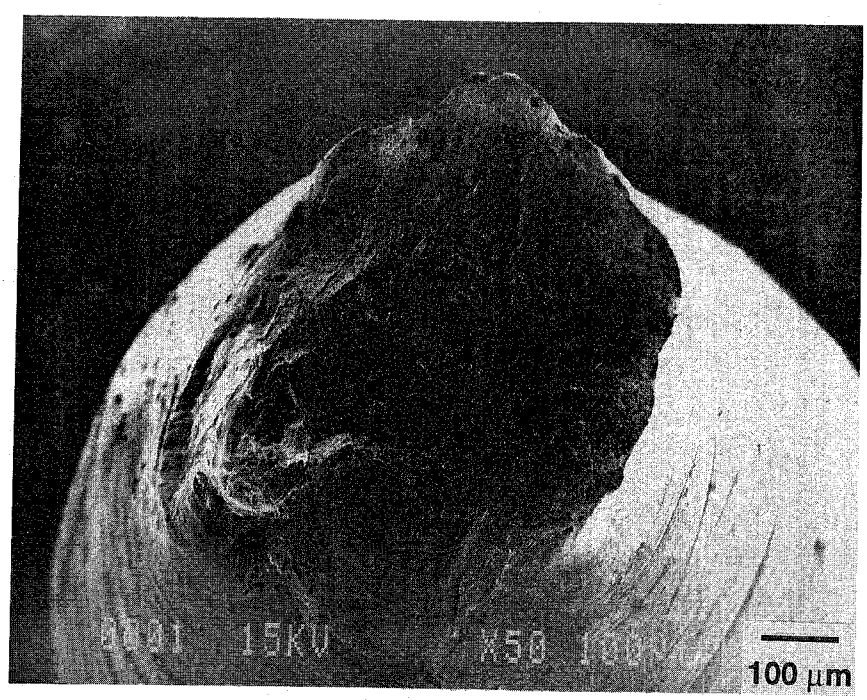

Figure 17. Scanning electron micrograph of the ductile microvoid coalescence type of fracture observed in Ti 15-3-3-3 when tested in argon at 150 °C.

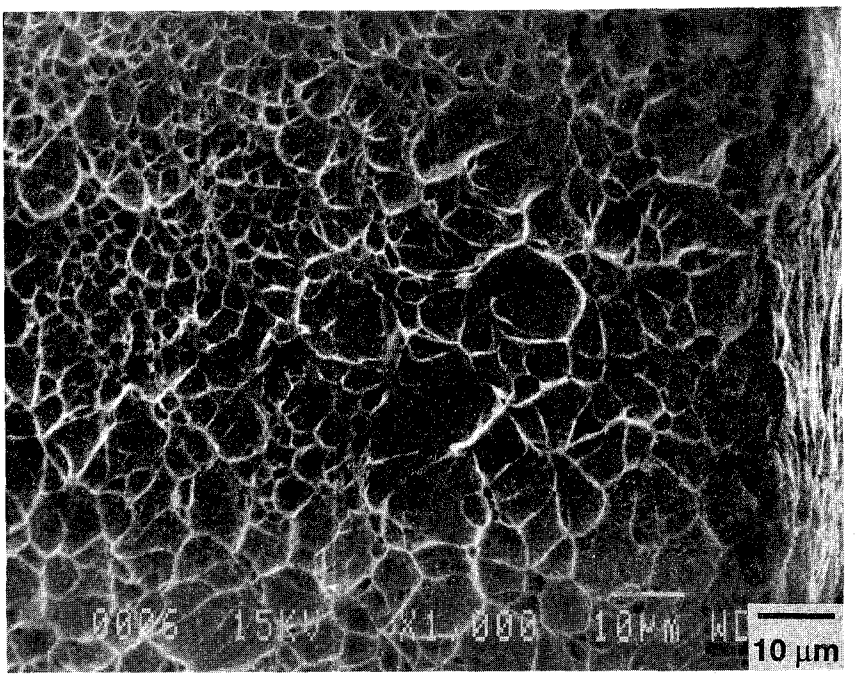

Figure 18. Higher magnification view exhibiting the microvoid coalescence observed on the titanium tensile specimens tested in argon at 150 °C.

Table 22. Reduction in area ratios at 150 °C [(RA in Agent)/(RA in Ar)]

Environment	Nitronic 40	304 SS	Titanium 15-3-3-3
Argon	*	*	*
Halon 1301	1.035	0.912	1.026
FC-218	1.038	0.912	1.068
HFC-227ea	1.021	0.909	1.015
HFC-125	0.879	1.078	0.985
CF_3I	1.024	0.888	0.820

Table 23. t-Test for significance in RA change at 150 °C

Environment	Nitronic 40	304 SS	Titanium 15-3-3-3
Argon	*	*	*
Halon 1301	0.699	-1.548	0.142
FC-218	0.768	-1.562	0.370
HFC-227ea	0.431	-1.615	0.084
HFC-125	-2.451	1.377	-0.084
CF_3I	0.476	-1.977	-0.983

Table 24. Average ultimate tensile strength at 20 °C (MPa)

Environment	Nitronic 40	304 SS	Titanium 15-3-3-3
Argon	718	793	579
Halon 1301	734	806	597
FC-218	735	805	627
HFC-227ea	726	799	633
HFC-125	746	803	606
CF_3I	724	803	603

Table 25. Standard deviation of the ultimate tensile strength measurements at 20 °C (MPa)

Environment	Nitronic 40	304 SS	Titanium 15-3-3-3
Argon	3.0	2.1	2.1
Halon 1301	3.0	2.5	2.4
FC-218	3.0	2.3	0.6
HFC-227ea	3.4	1.9	3.8
HFC-125	0.3	2.9	3.8
CF_3I	3.0	2.8	4.6

Table 26. Ultimate tensile strength ratios at 20 °C [(UTS in Agent)/(UTS in Ar)]

Environment	Nitronic 40	304 SS	Titanium 15-3-3-3
Argon	*	*	*
Halon 1301	1.023	1.016	1.031
FC-218	1.024	1.016	1.084
HFC-227ea	1.012	1.008	1.093
HFC-125	1.039	1.013	1.048
CF_3I	1.009	1.012	1.042

Table 27. t-Test for significance in UTS change at 20 °C

Environment	Nitronic 40	304 SS	Titanium 15-3-3-3
Argon	*	*	*
Halon 1301	1.072	1.076	0.840
FC-218	1.111	1.051	2.232
HFC-227ea	0.540	0.520	2.486
HFC-125	1.830	0.856	1.270
CF_3I	0.414	0.816	1.109

The ductility results for the 20 °C SSR tests are given in Tables 28-30. Table 28 gives the average strain to failure for each alloy/environment combination, and in argon at 20 °C. Table 29 shows the standard deviations for the STF calculations. The ratio of the average strain to failure for each alloy in each environment to that observed in the same alloy in argon at the same temperature is presented in Table 30. The significance of the difference is presented as a function of the alloy standard deviations, in Table 31. In Table 30, it can be seen that the STF ratios decreased for Nitronic 40 in all of the environments. However, both the 304 stainless steel and the titanium alloy exhibited increases in the STF ratio values in most of the environment/alloy combinations. This suggests that deformation may have been easier in these environments than in argon at this temperature.

Table 32 presents the RA data for each alloy in argon gas at 20 °C and each agent at 20 °C. Table 33 gives the standard deviations for these measurements and the ratio of the average reduction in area measured for each alloy/agent combination to argon at 20 °C is presented in Table 34. The statistical significance of the difference is again presented as a function of the alloy standard deviations in Table 35. In Table 34, it can be seen that the reduction in area values for Nitronic 40 increase in every agent. The 304 stainless steel alloy exhibited slight decreases in the RA values for all agents and the titanium alloy exhibited increases in every agent except for HFC-227ea, where it shows a significant decrease.

Based on these results, none of the alloys appear to be susceptible to environmentally induced fracture in these agents at 20 °C. Unlike the tests conducted at 150 °C, no evidence of environmentally induced cracking of any kind was observed on the fracture surface of any specimen tested at 20 °C. The values presented in these tables do not readily indicate any susceptibility to environmentally induced fracture at 20 °C.

5.4 Post Deployment Corrosion

When a fire suppressant is applied to a fire, the metals in the aircraft engine nacelle or the dry bays may become covered with deposits of the fire suppressant or fire suppressant combustion products. An additional evaluation of the relative corrosivity of the expected combustion products was included in the investigation. As a result, an evaluation of the relative corrosion behavior of representative structural materials with the combustion by-products was included in this investigation.

All of the potential replacements investigated in this study contain fluorine in their molecules and will produce fluoride ions and hydrofluoric acid (HF) during combustion. These ions are known to be aggressive when they contact certain alloy types. HF is commonly used to etch glasses and ceramics and will similarly attack the protective layer on the surface of passivated alloys. If the fluoride ion concentration in the combustion products deposited on the surface of an alloy exceeds some critical value, then pitting or crevice attack will result (Fontana, 1987, Zotikov, 1974, and Ricker, 1994). As a result, the post deployment corrosion damage to aircraft alloys will depend on the corrosivity of the surface films which contain these ions.

Most engineering alloys that exhibit good corrosion resistance do so because they form a protective surface film. This passive film is usually composed of metallic oxides or hydroxides (Fontana, 1987). Commercial aluminum alloys and stainless steels are examples of alloys which contain active elements, but behave in a relatively noble manner because of the formation of oxide films (Ricker, 1994). These protective surface films may be crystalline in form and may be precipitated from the solution adjacent to the bare metal surface, but it is widely believed that rapidly grown amorphous films are the most protective (Ricker, 1994). No matter what the structure of the surface

Table 28. Average strain to failure at 20 °C (%)

Environment	Nitronic 40	304 SS	Titanium 15-3-3-3
Argon	65.0	43.2	5.7
Halon 1301	63.1	44.4	6.9
FC-218	62.5	45.9	6.1
HFC-227ea	63.4	45.0	5.9
HFC-125	61.5	43.1	6.4
CF_3I	63.3	44.0	6.5

Table 29. Standard deviation of the strain to failure measurements at 20 °C (%)

Environment	Nitronic 40	304 SS	Titanium 15-3-3-3
Argon	0.9	2.5	0.7
Halon 1301	3.8	2.2	0.4
FC-218	3.7	2.7	0.2
HFC-227ea	2.1	1.3	3.5
HFC-125	1.4	3.2	1.0
CF_3I	1.1	3.0	0.1

Table 30. Strain to failure ratios at 20 °C [(STF in Agent)/(STF in Ar)]

Environment	Nitronic 40	304 SS	Titanium 15-3-3-3
Argon	*	*	*
Halon 1301	0.971	1.028	1.227
FC-218	0.962	1.062	1.073
HFC-227ea	0.975	1.041	1.045
HFC-125	0.947	0.999	1.139
CF_3I	0.974	1.020	1.154

Table 31. t-Test for significance in STF change at 20 °C

Environment	Nitronic 40	304 SS	Titanium 15-3-3-3
Argon	*	*	*
Halon 1301	-1.006	0.624	1.211
FC-218	-1.301	1.371	0.389
HFC-227ea	-0.861	0.902	0.240
HFC-125	-1.828	-0.030	0.741
CF_3I	-0.887	0.439	0.819

Table 32. Average reduction in area at 20 °C (%)

Environment	Nitronic 40	304 SS	Titanium 15-3-3-3
Argon	77.6	75.0	54.8
Halon 1301	78.7	74.3	60.3
FC-218	78.2	74.4	55.4
HFC-227ea	78.1	74.2	46.0
HFC-125	78.5	74.8	68.0
CF_3I	78.0	74.7	65.6

Table 33. Standard deviation of the reduction in area measurements at 20 °C (%)

Environment	Nitronic 40	304 SS	Titanium 15-3-3-3
Argon	1.2	0.4	6.9
Halon 1301	1.5	2.0	4.7
FC-218	0.7	0.6	4.9
HFC-227ea	1.3	0.3	23.9
HFC-125	0.9	1.0	25.4
CF_3I	0.4	0.5	3.1

Table 34. Reduction in area ratios at 20 °C [(RA in Agent)/(RA in Ar)]

Environment	Nitronic 40	304 SS	Titanium 15-3-3-3
Argon	*	*	*
Halon 1301	1.015	0.990	1.101
FC-218	1.008	0.991	1.011
HFC-227ea	1.007	0.989	0.839
HFC-125	1.012	0.997	1.241
CF_3I	1.005	0.996	1.197

Table 35. t-Test for significance in RA change at 20 °C

Environment	Nitronic 40	304 SS	Titanium 15-3-3-3
Argon	*	*	*
Halon 1301	1.433	-0.981	0.463
FC-218	0.740	-0.877	0.049
HFC-227ea	0.660	-1.154	-0.739
HFC-125	1.175	-0.262	1.110
CF_3I	0.474	-0.384	0.904

film, halogen ions generally tend to destabilize and/or reduce the protective nature of these films (Ricker, 1994).

Light weight alloys such as aluminum alloys are commonly used for aircraft applications. Unfortunately, these alloys are also susceptible to pitting corrosion in the presence of halide ions. Aluminum is a very active metal and alloys of this type will generally corrode as rapidly as mass transport kinetics will allow if the protective surface film is removed (Ricker, 1994). For this reason aluminum alloys are not used in environments where the passivity cannot be maintained (*i.e.*, pH<4 or pH>10). Other passivated materials such as titanium alloys and stainless steels are also susceptible to passivity breakdown.

In phase 1 of this study, the atmospheric corrosion behavior of representative aircraft alloys whose surfaces were contaminated with different chemical species expected to be produced by the combustion of different fire suppressants was investigated. In that investigation, three different surface pretreatments were used: (1) artificial seawater plus NaF, (2) artificial seawater plus $NaHCO_3/Na_2CO_3$, and (3) artificial seawater plus NaOH. The last two of these were used to represent surface conditions that may result from the use of $NaHCO_3$ as a fire suppressant and, therefore, are not relevant to this study. The first was used to represent surface conditions that may result from the combustion of fluoride or other halogen containing fire suppressants. When a surface film on a metal contains HF, the HF will react with the metal to form metal ions and hydrogen gas. This effectively

removes the hydrogen ion and increases the pH of the solution in the surface film. For NaF, the initial pH is higher, but the metal ions produced by corrosion will hydrolyze reducing the pH of the surface film. The end result is, whether the starting pH is low or high, the pH of the surface film will be determined by the chemical species present and the hydrolysis reaction. In Phase 1, it was decided to emulate the post deployment conditions by misting the surface of the samples. Because misting with HF would be a safety hazard and the steady state pH of the surface film is essentially independent of the initial pH, it was decided to sprinkle the surface with NaF instead of misting with HF. This resulted in questions about the difference that might result if the initial pH were lower. To resolve these questions, simple exposure experiments were conducted by dipping samples into different concentrations of HF and measuring their subsequent weight changes when exposed to humid air.

5.4.1 Materials. The materials selected by the sponsors for this study were designed to represent the broad range of aircraft structural materials which could be exposed to fire suppressant combustion bi-products. The materials selected were: 6061-T6 aluminum alloy, Inconel alloy 718, Inconel alloy 903, 410 stainless steel, titanium alloy Ti-8-1-1-1, titanium grade 5 alloy, Haynes alloy 188 and a 3501-6/AS4 epoxy-graphite composite. The compositions of these alloys are shown in Table 36.

5.4.2 Exposure Environment. According to the current military specifications, combustion product layers could remain on component surfaces for up to one month before the surfaces are cleaned. The effects of humidity variations, corrosion by condensate droplets induced by thermal cycling and contamination of the surface by salts or particulate matter were not included in this study. Also, the combustion products themselves may form fine carbonaceous particulates which could then precipitate onto the metal surfaces and behave as cathodes stimulating corrosion.

5.4.3 Experimental Procedure. The sample geometry used for this analysis was identical to the one shown in Figure 1 (Section 5.2.2). After machining, the surfaces were glass bead blasted to remove any remaining surface oxides or scale and to provide a consistent smooth surface finish (120 grit, nominal). Additional preparation prior to the start of these tests consisted of an ultrasonic cleaning in acetone then in alcohol, drying with warm air and immediate weighing using the same procedure used for the weight loss experiment.

The purpose of these experiments was to evaluate the corrosion behavior of representative aircraft materials after a deployment of a fire suppressant. The results of a study conducted by Linteris *et al.*, revealed that the initial concentration of HF produced by combustion decomposition of these agents ranges between 1.0 % and 10.0 % by volume (Nyden, 1994 and Linteris, 1994). As a result, one complete set of samples was immersed in an aqueous solution containing 1.0 volume percent HF for 60 s and a second set was immersed in a similar solution containing 10.0 volume percent HF for the same time period. At the end of this exposure, the samples were extracted and hung on individual hooks inside a sealed chamber with a constant relative humidity for 30 days. The chamber used for this exposure was specially designed to maintain a near-saturation relative humidity through the use of wicks along each side of the chamber. Regular hygrometer measurements indicated that the relative humidity inside the chamber ranged between 98 % and 100 %. Mass change measurements were taken at regular intervals during the exposure using the same weighing technique outlined previously in this report (Section 5.2.2).

5.4.4 Results. The results of the post deployment tests are presented in Figures 19 and 20. Figure 20 is a plot of the mass change per unit exposed area as a function of the exposure time following a 60 s immersion in 1.0 % by volume HF. In this figure, it can be seen that after approximately four days of exposure at 100 % relative humidity, there is little change in the rate of

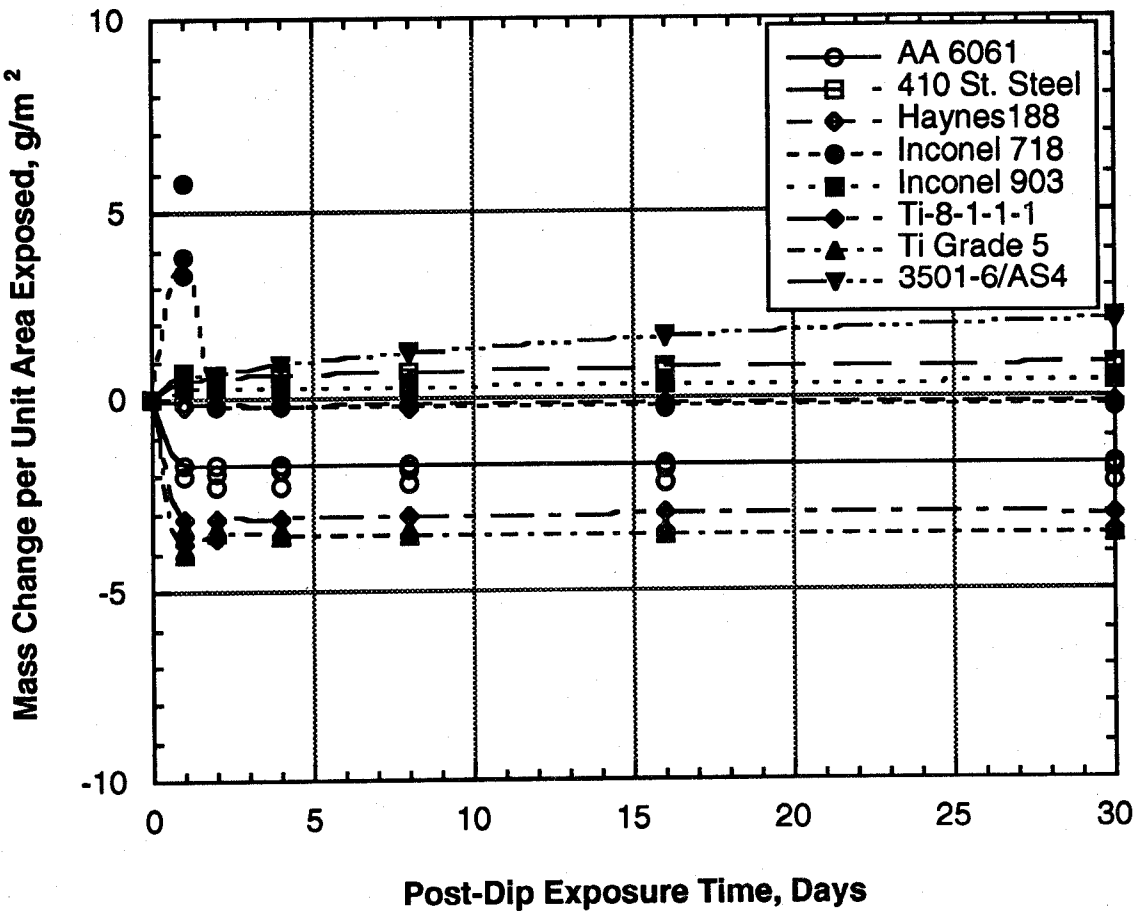

Figure 19. Mass change on exposure to saturated laboratory air following 60 s dip in 1 % HF.

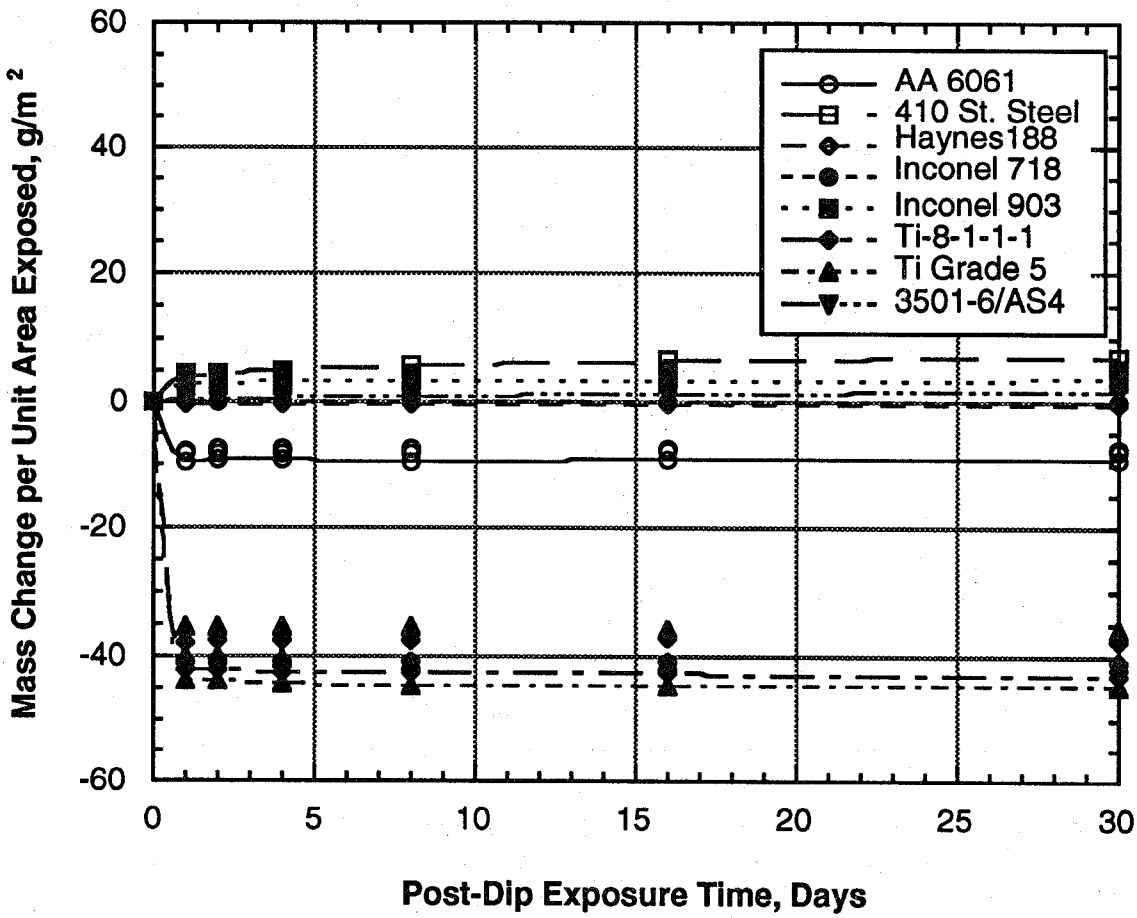

Figure 20. Mass change on exposure to saturated laboratory air following 60 s dip in 10.0 % HF.

Table 36. Composition of alloys used for post deployment testing (mass fraction in percent)

Element	Titanium 8-1-1	Inconel 718	410 SS	Haynes 188	Al 6061	Titanium Grade 5	Inconel 903
Al	7.60	0.51	--	--	bal	6.30	4.00
C	0.01	0.03	0.14	0.11	--	0.03	0.02
Cr	--	18.26	11.98	21.92	0.04	--	--
Cu	--	0.01	0.14	--	0.15	--	--
Fe	0.05	18.21	bal	2.47	0.70	0.18	41.90
Mn	--	0.05	0.31	0.86	0.15	--	0.12
Mo	1.00	2.87	0.02	--	--	--	--
Ni	--	54.01	0.20	22.53	--	--	37.96
Ti	bal	--	--	--	0.15	bal	--
V	1.00	--	--	--	--	4.00	--
Mg	--	--	--	--	1.20	--	--
Zn	--	--	--	--	0.25	--	--
0B	--	--	--	--	--	--	--
N	0.01	--	0.02	--	--	0.01	--
Co	--	0.02	--	bal	--	--	14.70
Nb	--	4.90	--	--	--	--	2.88
W	--	--	--	13.83	--	--	--

weight gain for the remainder of the thirty day exposure. The graphite/epoxy composite did continue to increase in mass, but this could be due to moisture uptake resulting from the high humidity. Research has shown that for these materials, moisture can be transported into the bulk by the wicking action of the fibers along the exposed edges and by solid state diffusion mechanisms (Stoudt, 1991).

Figure 20 is a similar plot showing the mass change as a function of exposure time after a 60 s immersion in 10.0 % by volume HF. During the immersion, the dissolution reactions were substantially more aggressive than those observed in the 1.0 % HF solution. As in Figure 19, the rate of mass change slowed shortly after the coupons were removed from the HF solution. The graphite/epoxy composite once again increased in mass, apparently the result of moisture uptake. In both cases, the decrease in the mass change rate can be attributed to the drying out of the corrosion products. Unlike the tests conducted in Phase I, the samples in this evaluation were not treated with any materials which could absorb and hold the water necessary to sustain the corrosion reactions. While the air in the exposure chamber was at saturation humidity, apparently, the corrosion products on the surface of the metal did not absorb water from the air otherwise corrosion and/or mass increases would have been observed. As a result, there was no liquid phase present to stimulate corrosion reactions. In essence, the layer of the corrosion products on the surface have an equilibrium vapor pressure for water that is greater than that of the air in the chamber so they stayed relatively dry. This may or may not be the case in actual service, since any kind of re-wetting of the corrosion product layer will re-establish the corrosion reactions (e.g., thermal transients causing condensation - fog, dew, rain, etc.)

and actual combustion product films will be composed of many more chemical species many of which may absorb water.

5.5 Electrochemical Measurements

There are a number of different electrochemical techniques that can be used to measure the corrosion rates of metals (Bard, 1980). However, because the fire suppression candidates have a high electrical resistivity, testing in these solutions becomes very difficult. For example, HCFC-124 (CF_3CHClF), has a resistivity of 1.5×10^9 ohms·cm. One technique that can be employed to enable electrochemical measurements in these environments is to add a salt to the environment which will dissolve and provide charge carriers to the electrolyte, but not alter the corrosivity of the environment (Sawyer, 1974). The choice of a salt for supporting the transfer of charge in these agents is complicated by their low dielectric constants. For example, the dielectric constant of HCFC-124 is about 6.73 (CRC Handbook, 1990). While the dielectric constant for the other compounds cannot be found in tables, examination of compounds with similar symmetry and bond strengths indicates that the dielectric constant for CF_3I and HFC-125 should be around 3.5 and 6, respectively, and even higher for FC-218, HFC-227ea and halon 1301. As a result, simple salts will not dissolve in these compounds. Several authors have shown (Pournaghi-Azar, 1994, Bond, 1988, Park, 1994 and Kadish, 1984), that quaternary ammonium salts, on the other hand, will dissolve in low dielectric constant media such as dichloromethane and chloroform where the dielectric constants are 9.08 and 4.81, respectively.

The behavior of the candidate compounds can essentially be characterized as aprotonic in nature. As a result, their ability to ionize a supporting electrolyte is significantly reduced. The ability of a salt to be ionized in this type of medium is primarily a function of the anion (Sawyer, 1974). As the size of the anion increases and its electronegativity decreases, ionization becomes more probable (Sawyer, 1974). Furthermore, dissociation of the supporting salt is limited by the very low dielectric constant of the replacement candidates (Sawyer, 1974). This can be overcome, to a certain extent, by choosing a salt in which the cation and anion have a small charge to volume ratio. On the other hand, as the size of the cation and anion increase, their mobility, and hence the solution conductivity, is reduced (Ue, 1994). For a given charge on an ion, the size effect will have a larger affect on the dissociation constant of a salt than on the ionic mobility in a given medium. The molecular structure of the supporting salt will also affect its mobility in a solvent. The ionic mobility, and hence the solution conductivity, will decrease as the molecular interaction increases. Because of their small charge to volume ratio and their anions are of intermediate size, tetrabutylammonium hexafluorophosphate ($TBAPF_6$) and tetrabutylammonium trifluoromethanesulfonate (TBATFMS) were chosen as supporting salts (Ue, 1994).

As explained in a previous study, in order to define the potential axis for polarization measurements, a platinum quasi-reference electrode (Pt-QRE) referenced to the half wave potential ($E_{1/2}$) of the ferrocene/ferrocinium ($Cp_2Fe^{0/+}$) reduction-oxidation (redox) couple is necessary (Dante, 1994). The nonpolar character of this outer sphere redox couple facilitates its dissolution into compounds with a low dielectric constant.

Once the potential scale is established, three electrode slow scan measurements can be made and a Tafel extrapolation can be used to estimate the corrosion rate of the storage vessel alloys in the halon replacement candidates.

5.5.1 Materials. The alloys examined in this analysis were: 304 stainless steel, Nitronic 40 stainless steel, aluminum alloy 6061-T6, and Titanium alloy 15-3-3-3. The compositions of these alloys are given in Table 1, Section 5.2.2.

5.5.2 Experimental Procedure. The vapor pressure for HCFC-124, HFC-125, and CF_3I are 3.393 Pa x 10^5 Pa, 11.051 Pa x 10^5 Pa, and 4.390 Pa x 10^5 Pa, respectively, at room temperature. Therefore, electrochemical measurements of the corrosion rate in the liquid phase of these agents requires the experiments be conducted in a closed pressure chamber. A stainless steel pressure vessel was modified to allow for electrical feed-throughs, Figure 21. The vessel was constructed of 0.635 cm thick 316 stainless steel and was rated for pressures of ~ 6.9 MPa. Four electrical feed-throughs were mounted through the head of the cell for performing two, three, or four electrode electrochemical tests. A pressure gauge was mounted on the cell to measure the vapor pressure in the cell. At higher temperatures, most of the gasses used in this study can reach very high vapor pressures so a rupture disc was incorporated to prevent accidental over pressurization. Temperature was monitored with the use of a thermocouple mounted in the head of the cell.

Electrochemical measurements were made using a commercial potentiostat. A commercial frequency response analyzer was used to make impedance measurements and the data was collected using commercially available software.

Before filling the electrochemical cell with one of the halon replacement candidates, 5 x 10^{-2} mol/L of one of the supporting salts, either TBATFMS or $TBAPF_6$, was placed into the cell. Then, the cell was closed and purged with dry argon to remove water vapor. After 5 min, the fill valves were closed and the cell was chilled for 30 min to 60 min. Chilling facilitated filling the cell with agents. The agent was removed from the liquid phase in the storage bottle. Enough agent was transferred to the electrochemical cell to form a 3 cm deep (250 ml) liquid phase in the bottom of the cell, *i.e.*, 352 g, 353 g, and 555 g of HCFC-124, HFC-125, and CF_3I, respectively. In all tests, a large area platinum-rhodium counter electrode and a platinum wire quasi-reference electrode (Pt-QRE) were used. The Pt-QRE electrode was placed between the counter and working electrodes approximately 2.5 cm from the working electrode. The electrodes were attached to the electrical feed-throughs using heat shrink tape. For the working electrodes, electrical contact was made using clips.

The effectiveness of both TBATFMS and $TBAPF_6$ in lowering the resistivity of HCFC-124, HFC-125, and CF_3I was measured using electrochemical impedance spectroscopy (EIS). The cell resistance was obtained by noting the value where the curve intersected the real impedance axis on the Nyquist plot. This value was converted to a resistivity by multiplying by the electrode area and subsequently dividing by the distance between the working and reference electrode. Unfortunately, it was not possible to get sufficient quantities of either of these salts to dissolve in either HFC-227ea or halon 1301 to enable electrochemical measurements.

Tests were run to elucidate the electron transfer kinetics of $Cp_2Fe^{0/+}$ in HCFC-124, HFC-125 and CF_3I. The tests were run at room temperature. A Pt disk working electrode (area = 0.00317 cm^2) was prepared by encapsulate a platinum wire in glass and polishing the electrode face to a 1 μm finish. The oxidation and reduction waves of ferrocene in each experiment were measured with respect to the Pt-QRE. The potential scale was then normalized to the half-wave potential of $Cp_2Fe^{0/+}$ redox couple.

In subsequent tests, the corrosion rate of 304 (area = 0.00785 cm^2) and Nitronic 40 (area = 0.01461 cm^2) stainless steels, aluminum 6061-T6 (area = 0.01954 cm^2), and Ti 15-3-3-3 were studied in the three agents using slow sweep voltammetry (scan rate = 0.5 mV/s) and Tafel extrapolations. In all cases, wires of each alloy were encapsulated in glass and the electrode surfaces were polished to a 1 μm finish. All of the alloys except 304 stainless steel were extruded and heat treated from stock samples. It should be noted that the encapsulation process involved temperature in excess of 500 °C for short periods of time which may have modified the metallurgy of the wires slightly.

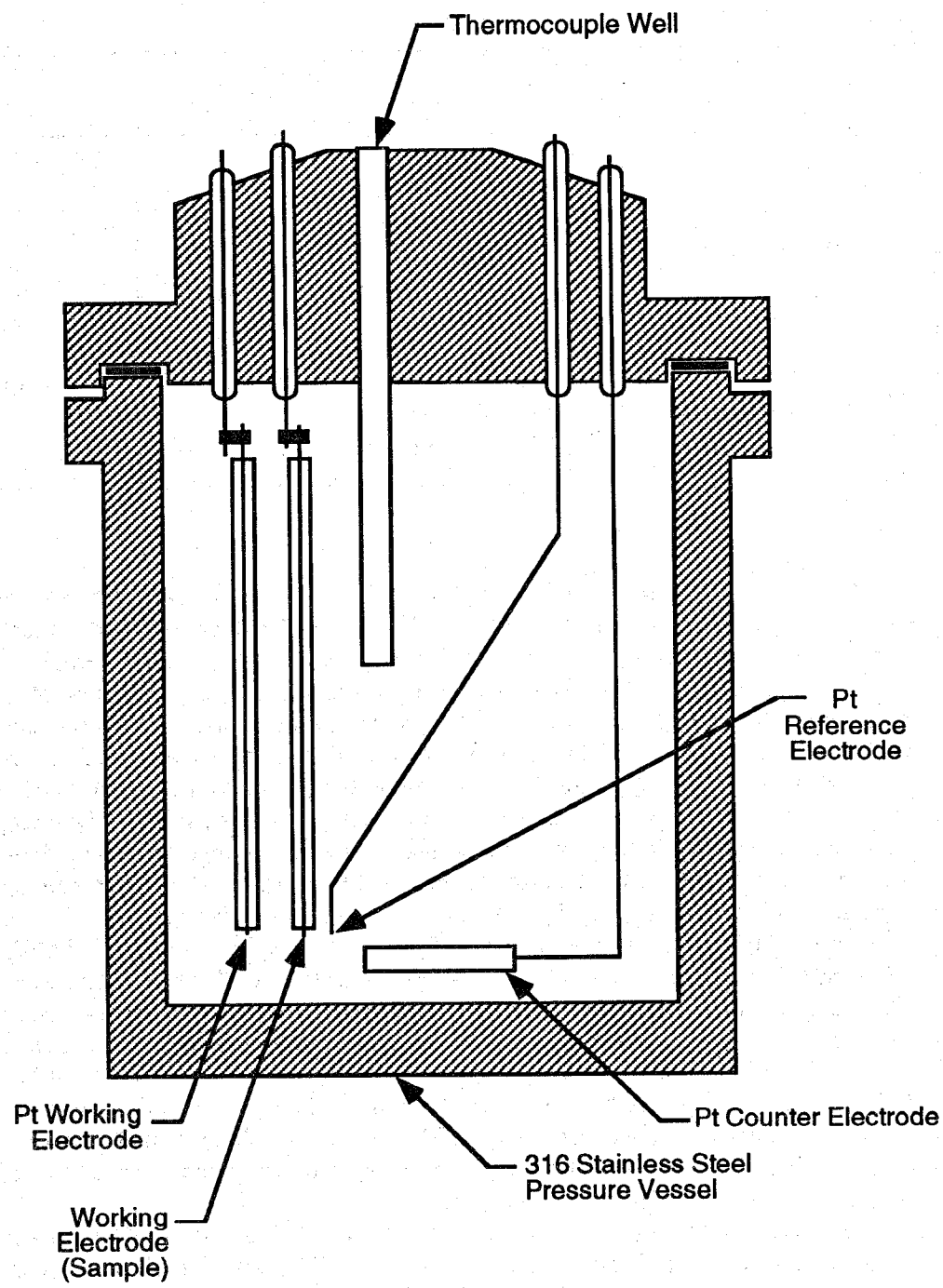

Figure 21. Electrochemical cell for making measurements in high vapor pressure low conductivity electrolytes.

Table 37. Resistivity and electron transfer rate constants of $Cp_2Fe^{0/+}$ and oxidation rates in various replacement candidates

Agent	Supporting Salt	Resistivity, ρ Ohms-cm	k^0 cm/s
HCFC-124	TBATFMS	80	0.0020
HCFC-124	$TBAPF_6$	79	0.0013
HFC-125	TBATFMS	44	0.0024
HFC-125	$TBAPF_6$	740	$2.5x10^{-4}$
CF_3I	TBATFMS	748	$3.6x10^{-4}$
CF_3I	$TBAPF_6$	---	---

5.5.3 Agent Resistivity. Electrochemical impedance spectroscopy (EIS) was used to measure the resistivity of the agents as a function of added salt. Values for the resistivity of the agent/salt combinations are shown in Table 37. Several conclusions can be drawn from this data. The resistivity of the agent/supporting salt electrolyte is related to several factors *i.e.*, the ionization of the salt, the mobility of its ions and the dissociation constant of the salt in the medium which regulates the number of ions available as charge carriers from the solvated salt. Furthermore the size of the two salts is approximately the same (Ue, 1994) with the TFMS anion being slightly larger. Analysis of Table 37 reveals that the resistivity of $TBAPF_6$ and TBATFMS in HCFC-124 is similar. The charge to volume ratio of the TFMS anions are slightly smaller than that of the PF_6^- anions and hence dissociate to a slightly larger extent in HCFC-124. In order for the resistivity of the solutions containing the different salts to be similar, the mobility of the PF_6^- ions must be higher than that for the TFMS anions.

The situation in HFC-125, however, is very different. The resistivity of the $TBAPF_6$ electrolyte is an order of magnitude higher than that of the TBATFMS electrolyte. With the verified assumption that all of the salts are dissolved and knowing that the ions are of the same general size, the difference in resistivity must be attributed to a difference in the number and mobility of the charge carriers in HFC-125. The TFMS ion has a structure that more closely resembles the structure of HFC-125 than PF_6^- does, thus facilitating the ability of TBATFMS to move through the medium in response to an applied field. The charge to volume ratio of the TFMS anions are slightly smaller than that of the PF_6^- anions and hence dissociate to a slightly larger extent in this medium. These two effects combine to give a much lower resistivity for TBATFMS in HFC-125.

The TFMS ions more closely resemble the molecules of HFC-125 than HCFC-124 implying a weaker intermolecular force and hence a higher mobility in HFC-125. The dielectric constant of HFC-125 is slightly lower than that for HCFC-124. Thus, the number of charge carriers would be greater in HCFC-124. From Table 37, the resistivity of the TBATFMS solution is slightly lower in HFC-125 suggesting that the mobility of the charge carriers is the major factor contributing to the lower resistivity of TBATFMS in HFC-125. That is, even though the number of charge carriers is lower in HFC-125, they are more mobile than those in HCFC-124 and result in a lower resistivity in HFC-125. Table 37 illustrates the fact that the resistivity is an order of magnitude higher in HFC-125

relative to HCFC-124 containing $TBAPF_6$. The number of charge carriers in HCFC-124 would be greater than that in HFC-125 because of the higher dielectric constant of HCFC-124. This implies that the mobility of the charge carriers in HCFC-124 would be similar to or slightly higher than in HFC-125.

HCFC-124 and HFC-125 containing 5 x 10^{-2} mol/L of TBATFMS have similar resistivities. The resistivity in CF_3I, however is an order of magnitude higher. Since the dielectric constant of CF_3I is much lower than that in the other salts, the number of charge carriers in this medium are much less. This fact alone accounts for the much increased resistivity. $TBAPF_6$ does not dissolve in CF_3I. The slightly higher polarity of this molecule compared to TBATFMS is enough to prevent its dissolution.

5.5.4 Defining a Reference Potential. Figure 22 displays a 0.1 V/s CV scan from -2.5 V to 1 V versus a Pt-QRE in HCFC-124 and HFC-125 containing 5 x 10^{-4} mol/L of ferrocene and 5 x 10^{-2} mol/L of $TBAPF_6$. These scans represent a typical CV in the above environments. The current was measured at a glass encapsulated Pt electrode. The potential axis has been normalized to $E_{1/2}(Cp_2Fe^{0/+})$, which appeared at 0.234 V and 0.481 V (Pt-QRE) in HCFC-124 and HFC-125 respectively. It can be seen from the figure that a major reduction occurs in both environments at approximately -2.55 V ($Cp_2Fe^{0/+}$). This suggests that the peak at -2.55 V ($Cp_2Fe^{0/+}$) is a reduction process associated with the supporting salt. This peak is in the vicinity of the onset of reduction for the Bu_4N^+ cation in dimethylformamide and acetonitrile (Kadish, 1984). At approximately -1.50 V ($Cp_2Fe^{0/+}$) a slight change in the curve can be seen for both environments. In this figure, the peak height is small, but it varies in magnitude each time the test cell is reassembled. The peak is thought to be a result of water contamination. This is supported by other experiments that demonstrate that the magnitude of the peak changes when controlled amounts of H_2O are injected into the cell. In this study, there was no evidence of any oxidation occurring at 1.0 V (Pt-QRE) or 0.77 V ($Cp_2Fe^{0/+}$) leaving at least a 2.27 V window where no reactions occur on Pt. By averaging the peak separation between ferrocene and the Bu_4N^+ and ferrocene and the water peak for scan rates up to 0.5 V/s in each environment, the following results are obtained: $E_{1/2}(Cp_2Fe^{0/+}) - E(Bu_4N^+) = 2.55$ V ± 0.002 V and 2.56 V ± 0.014 V, respectively, $E_{1/2}(Cp_2Fe^{0/+}) - E_{H2O} = 1.50$ V and 1.50 V for HCFC-124 and HFC-125 containing $TBAPF_6$, respectively.

Figure 23 displays a 0.1 V/s scan from -3 V to 1 V (Pt-QRE) in HCFC-124, HFC-125, and CF_3I containing 5 x 10^{-4} mol/L of ferrocene and 5 x 10^{-2} mol/L of TBATFMS. These are typical results for the above environments. As before, the current was measured at a glass encapsulated Pt electrode and the potential has been normalized to $E_{1/2}(Cp_2Fe^{0/+})$ which appeared at 0.19 V, 0.17 V, and 0.35 V (Pt-QRE) for HCFC-124, HFC-125, and CF_3I, respectively. At 2.48 V ($Cp_2Fe^{0/+}$) and 2.55 V ($Cp_2Fe^{0/+}$) for HCFC-124 and HFC-125, respectively, a major reduction peak can be seen. The peak separation between the ferrocene half wave and the major reduction peak is similar to the case in which $TBAPF_6$ was the supporting salt lending further credence to the belief that the major reduction peak is a result of the reduction of Bu_4N^+. A second peak at 1.503 V ($Cp_2Fe^{0/+}$) and 1.458 V ($Cp_2Fe^{0/+}$) for HCFC-124 and HFC-125, respectively, is associated with water. This peak is much more pronounced for the curves in Figure 22 than for those is Figure 23. This may be a result of contamination of the TBATFMS. In several cases, the water peak masks the onset of the large reduction peak of the salt and care must be taken when determining the half wave potential of ferrocene in the situation where no ferrocene is present. Oxidation of the electrolyte was not seen for several hundred mV above the half wave potential of ferrocene yielding a usable potential window of at least 2.0 V anodic of the water peak. Peak separations for scans up to 0.5 V/s were averaged and the results are as follows: $E_{1/2}(Cp_2Fe^{0/+}) - E(Bu_4N^+) = 2.49$ V ± 0.008 V and 2.55 V ± 0.008 V for

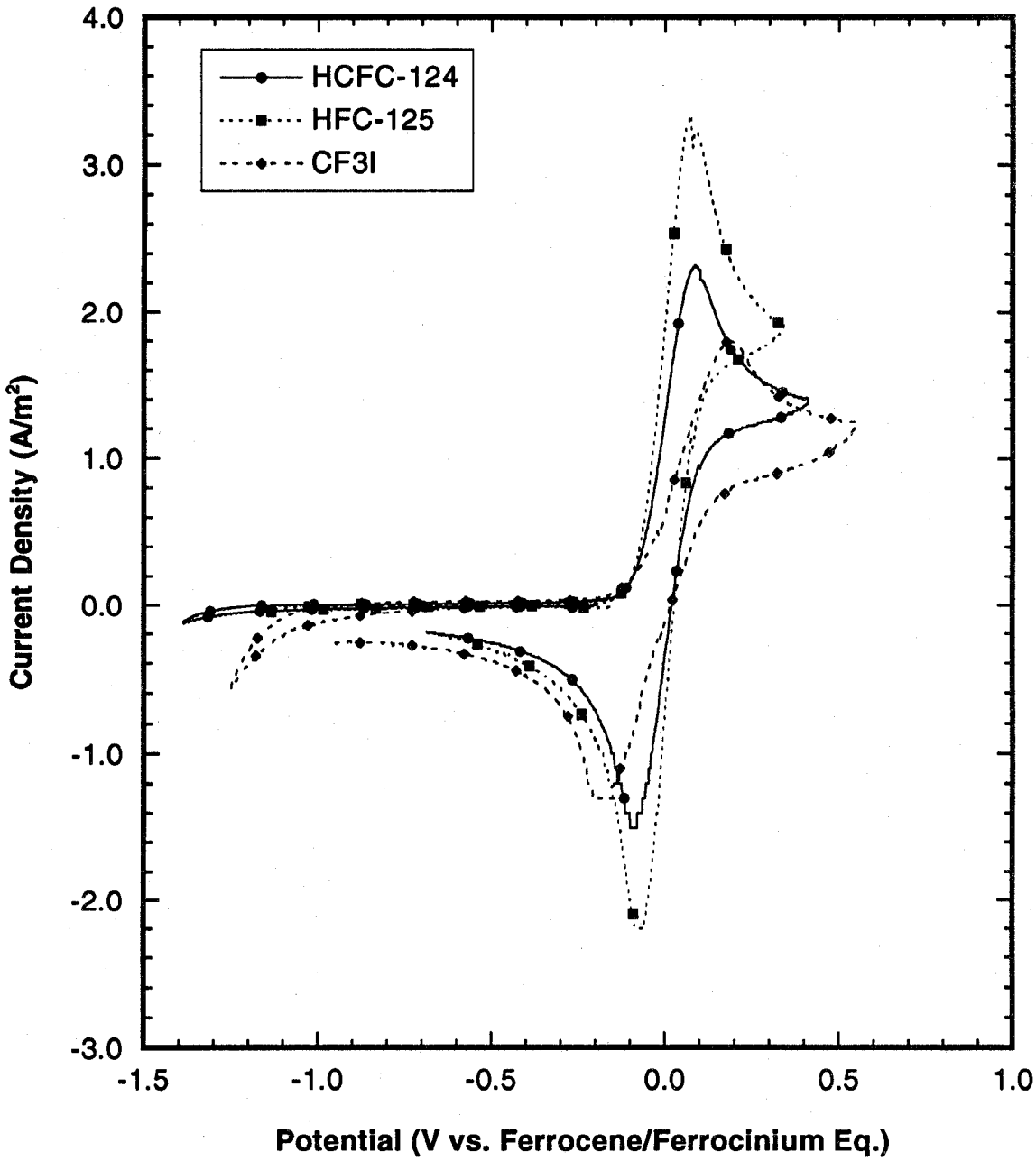

Figure 22. 0.1 V/s voltametric sweep on a Pt-QRE in HCFC-124 and HFC-125 using 5 x 10^{-4} mol/L of ferrocene and 5 x 10^{-2} mol/L of $TBAPF_6$ (1 out of 50 data points shown).

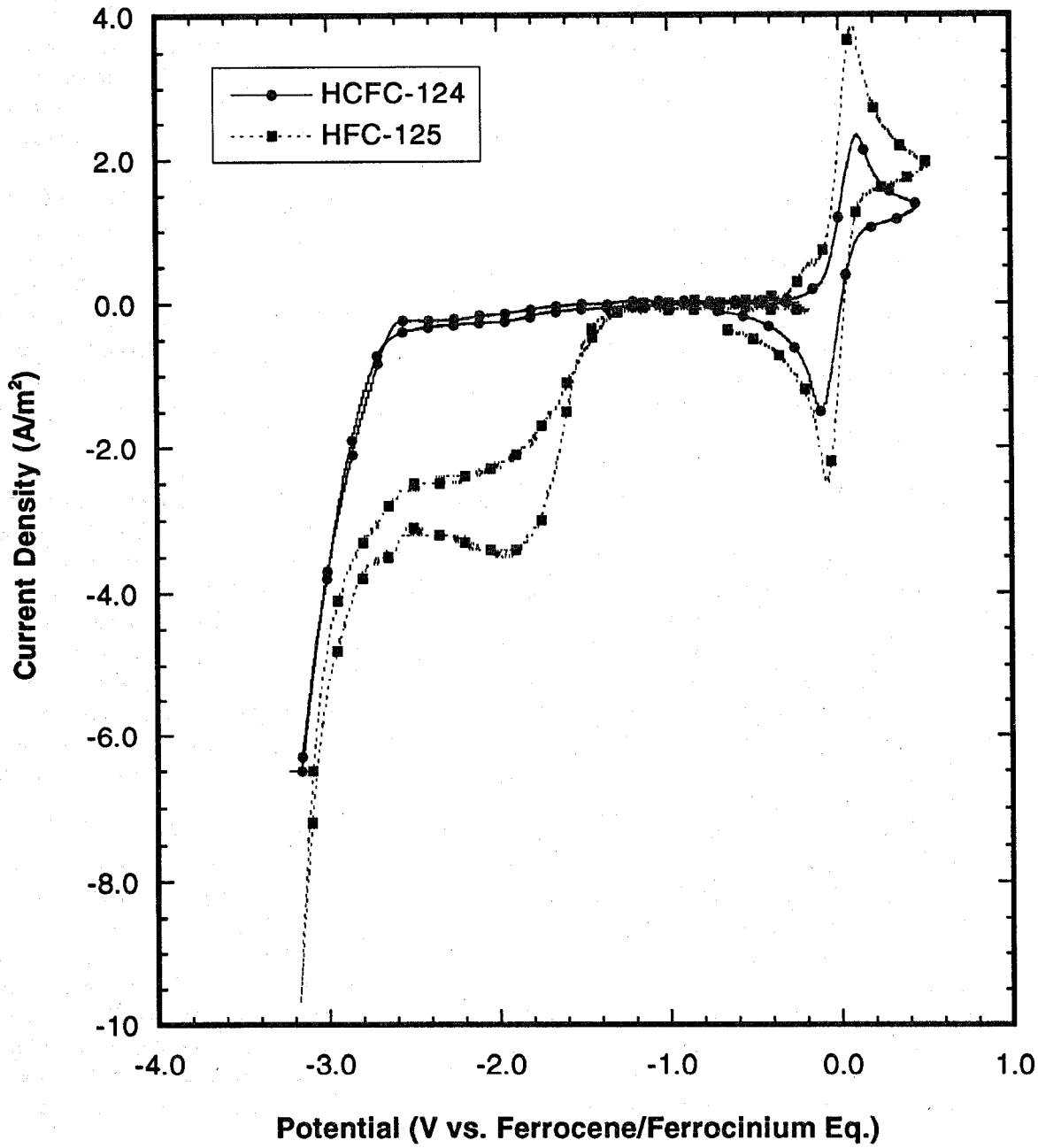

Figure 23. 0.1 V/s voltametric sweep on a Pt-QRE in HCFC-124, HFC-125, and CF_3I using 5 x 10^{-4} mol/L of ferrocene and 5 x 10^{-2} mol/L of TBATFMS (1 out of 50 data points shown).

HCFC-124 and HFC-125 respectively, $E_{1/2}(Cp_2Fe^{0/+}) - E_{H2O}$ = 1.50 V ± 0.009 V and 1.47 V ± 0.008 V for HCFC-124 and HFC-125, respectively.

The situation with TBATFMS in CF_3I is different from this salt in the other two environments. As can be seen in Figure 24, only one major reduction peak is observed at 1.095 V ($Cp_2Fe^{0/+}$). The peak is very large and the peak maximum is never detected. The addition of water has no affect on the voltammograms. It can not be ruled out, however, that this large peak is a result of water contamination. It is known that water is often found as a contaminant of CF_3I. The usable window for CF_3I containing TBATFMS is at least 1.5 V. Peak separations for scans up to 0.5 V/s were averaged yielding $E_{1/2}(Cp_2Fe^{0/+}) - E_{unknown}$ = 1.103 V ± 0.008 V.

In subsequent experiments studying the corrosion of alloys in HCFC-124, HFC-125, and CF_3I, there was no ferrocene added to the cell. $E_{1/2}(Cp_2Fe^{0/+})$ was then defined by noting the position of the salt reduction, finding the appropriate value for the separation of the reduction peak and the ferrocene peak listed in Table 38, and realizing that ferrocene is this much more anodic than the Bu_4N^+ reduction peak. In several of these experiments, however, the reduction peak associated with H_2O masked the onset of reduction of the salt. In this case, $E_{1/2}(Cp_2Fe^{0/+})$ was defined with reference to the separation of ferrocene and the water peak. In the case of CF_3I, the half wave potential of ferrocene was measured using the peak separation of the large reduction peak and ferrocene, listed in Table 38, in all cases.

5.5.5 $Cp_2Fe^{0/+}$ Electron Kinetics. Cyclic voltammograms of $Cp_2Fe^{0/+}$ oxidation and reduction peaks on a Pt disk electrode in HCFC-124, HFC-125, and CF_3I at 0.1 V/s with TBATFMS as the supporting salt are shown in Figure 24. Using $TBAPF_6$ as the supporting salt resulted in similar scans. Peak separation (E_a -E_c) and the separation of the anodic peak potential and the half-wave potential of $Cp_2Fe^{0/+}$ (E_a - $E_{1/2}$) as a function of scan rate were used to estimate the electron transfer rate constant, k^0 (Bard, 1980). Values for k^0 in all of the agent/supporting salt combinations is shown in Table 37. k^0 was calculated assuming a diffusion coefficient of 1 x 10^{-5} cm^2/s and α = 0.5. It should be noted that no IR compensation was used in the current experiments. The very large uncompensated resistance would thus result in a lowering of the k^0 values as the scan rate increased. Compensation for IR drop was attempted, but efforts to do so resulted in oscillations at entered resistance values that were much lower than their actual values.

The k^0 values found in the literature for $Cp_2Fe^{0/+}$ in acetonitrile, dichloromethane and chloroform using similar sized electrodes are k^0 ~ 9 x 10^{-2}, 6 x 10^{-2}, and 3 x 10^{-2} cm/s, respectively (Pournaghi-Azar, 1994 and Kadish, 1984). The k^0 values of $Cp_2Fe^{0/+}$ obtained in this study are approximately an order of magnitude lower, in the case of HCFC-124 with both salts and HFC-125 with TBATFMS. It should be mentioned that k^0 values for $Cp_2Fe^{0/+}$ of the magnitude seen in this study have been observed in electrolytes with similar dielectric constants using electrodes of similar proportions (Bond, 1988). In the case of HFC-125 with $TBAPF_6$ and CF_3I with TBATFMS, the k^0 values are about 1.5 orders of magnitude lower. In a study by Kadish *et al.*, there appears to be an inverse relationship between the solution resistivity and the value of k^0 that is not related to uncompensated resistance (Kadish, 1984). This trend is verified in the data for both TBATFMS and $TBAPF_6$.

It is interesting to note that in HCFC-124, as is the case for the resistivity, the k^0 values appear to be unaffected by the salt used. In HCFC-124 with both salts and HFC-125 with TBATFMS, k^0 decreases slightly with scan rate, at higher scan rates, indicating that IR does play a minor role in the low k^0 values obtained in this study. It was also noted that the k^0 values decrease with scan rate to a greater extent in HFC-125 using $TBAPF_6$ and CF_3I using TBATFMS. This implies that the IR effect is much more noticeable in those two environments as would be expected given the values of the resistivity in Table 37.

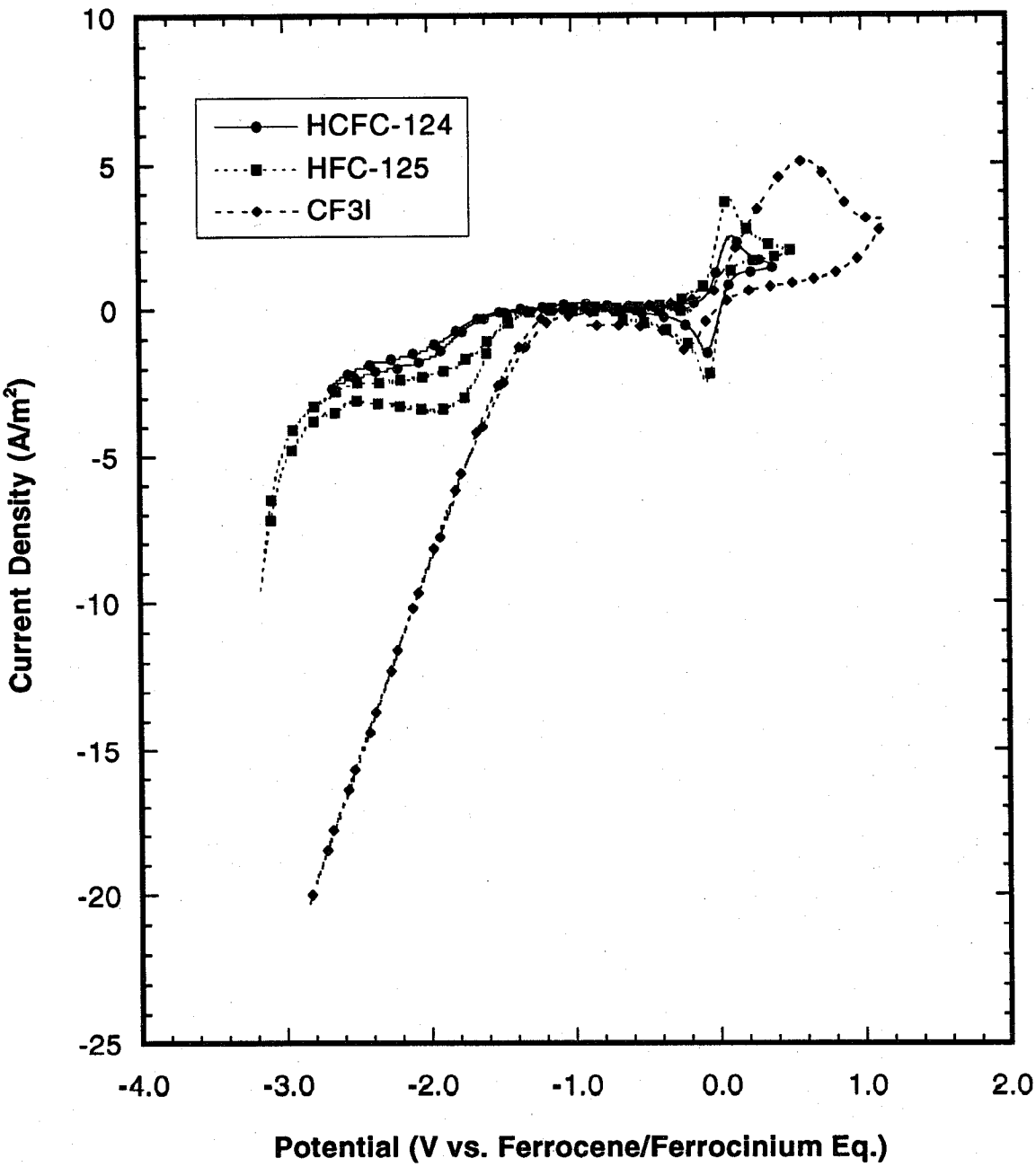

Figure 24. Ferrocene oxidation and reduction peaks on a Pt-QRE in HCFC-124, HFC-125, and CF_3I. (1 out of 50 data points shown).

Table 38. Reference peak values

Agent	Supporting Salt	$E_{1/2}(CP_2Fe^{0/+})$- E_{lrp}(TBA) Volts	$E_{1/2}(CP_2Fe^{0/+})$-E_{H20} Volts
HCFC-124	TBATFMS	2.49 ± 0.008	-1.50 ± 0.009
HCFC-124	$TBAPF_6$	2.55 ± 0.002	-1.50
HFC-125	TBATFMS	2.55 ± 0.009	1.47 ± 0.008
HFC-125	$TBAPF_6$	2.56 ± 0.014	-1.50
CF_3I	TBATFMS	1.103 ± 0.008	---
CF_3I	$TBAPF_6$	---	---

lrp = large reduction peak for tetrabutylammonium (TBA)

Based on solution resistivity and k^0 values in the various media, it appears that alternative fire suppressant solutions containing 5 x 10^{-2} mol/L of TBATFMS and 5 x 10^{-4} mol/L of ferrocene are the most appropriate systems for measuring corrosion rates of storage container alloys.

5.5.6 Corrosion Rates of Storage Vessel Alloys in HCFC-124, HFC-125, and CF_3I. Figures 25, 26, and 27 show Tafel plots of 304 stainless steel, Nitronic 40, Al 6061 T6, and Ti 15-3-3-3 in HCFC-124, HFC-125, and CF_3I, respectively. In all cases, the free corrosion potential (FCP) was very difficult to obtain and moved cathodically from a more or less stable value when potentiodynamic scans were performed. This cathodic movement was observed regardless of the direction of the scan. Fairly reproducible FCPs and scans were made by preconditioning the working electrode prior to a scan. A potential of -0.1 V was applied to the working electrode for 10 s prior to each scan. The potential was then allowed to return to a steady state over approximately 30 min. The sliding FCP was less severe in HFC-125. Therefore, scans were begun at -250 mV below the FCP and ended at 500 mV over the FCP. In the other two environments, where the FCP is less stable, potentiodynamic scans were begun at -100 mV below the FCP and terminated at 1.5 V of the FCP.

Table 39 shows the results of Tafel (Bard, 1980) extrapolations of the curves in Figures 25, 26, and 27. The extrapolation was based primarily on the anodic curves. It can be seen from the results that the corrosion current density in alternative fire suppressants is extremely low. The values are on the order of those obtained for passivated metals in aqueous solutions. No evidence of transpassive behavior was observed for any of the metals in any environment, even at high overpotentials. The low current densities may be a result of both a protective air formed oxide as well as the low dielectric constant of the environment. The presence of oxidation and reduction precursors and by products, *i.e.*, H^+, OH^-, and metal ions, are highly unfavorable in the low dielectric constant media.

Corrosion rates of the four alloys are reported in the third column of Table 39. The estimated weight loss values were calculated assuming the current densities in Table 39 and that the major dissolution phases are Fe/Fe^{2+} for Nitronic 40 and 304 SS, Al/Al^{3+} for Al 6061, and Ti/Ti^{2+} for Ti 15-3-3-3. In the fourth column of Table 39, weight change data from 25 day immersion tests at 20 °C is presented. All but two of the weight change data are positive indicating that film formation had

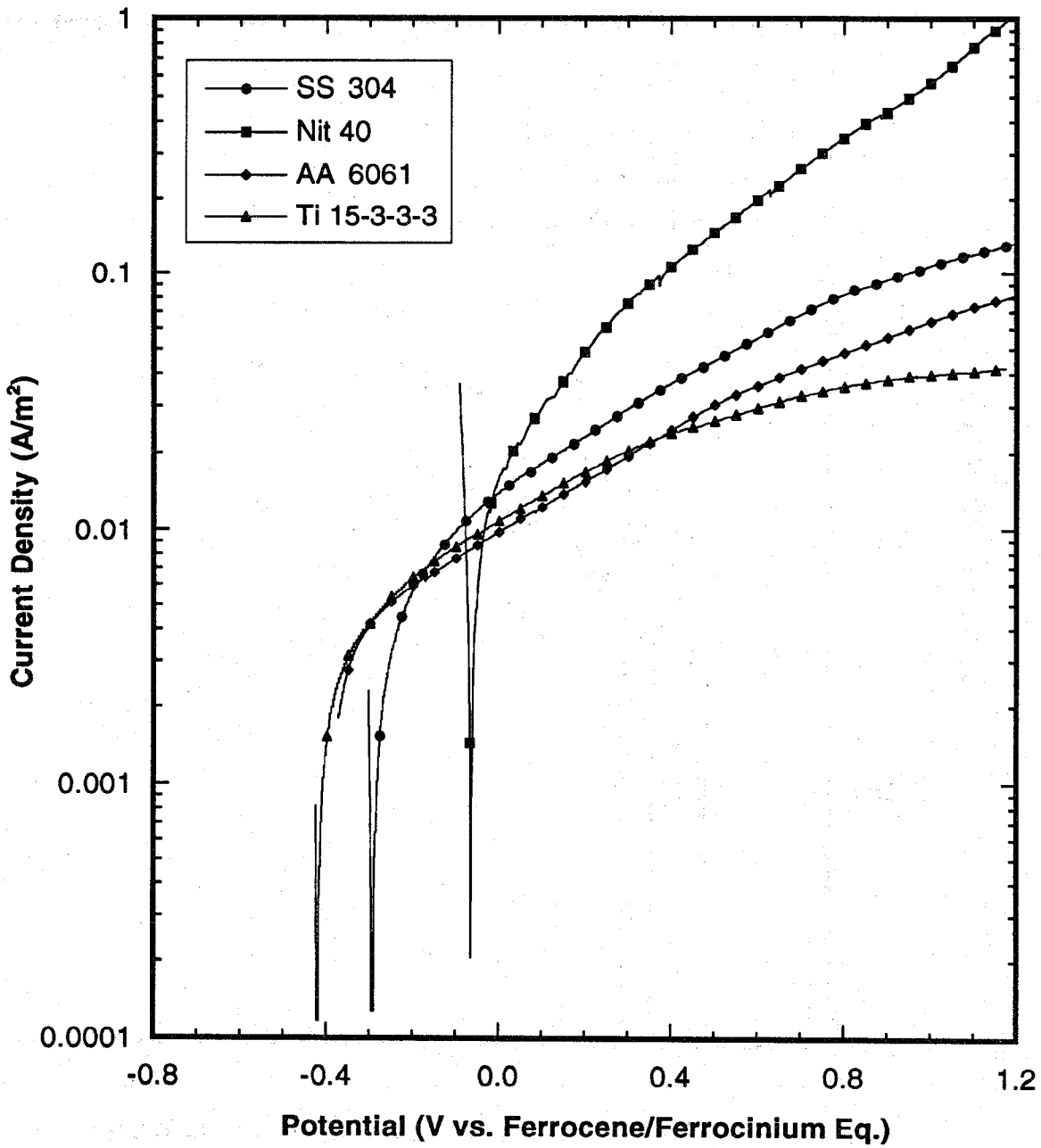

Figure 25. Potentiodynamic scans of 304SS, Nitronic 40, Al 6061-T6, and Ti 15-3-3-3 in HCFC-124 containing 5 x 10^{-2} mol/L of TBATFMS (1 out of 50 data points shown).

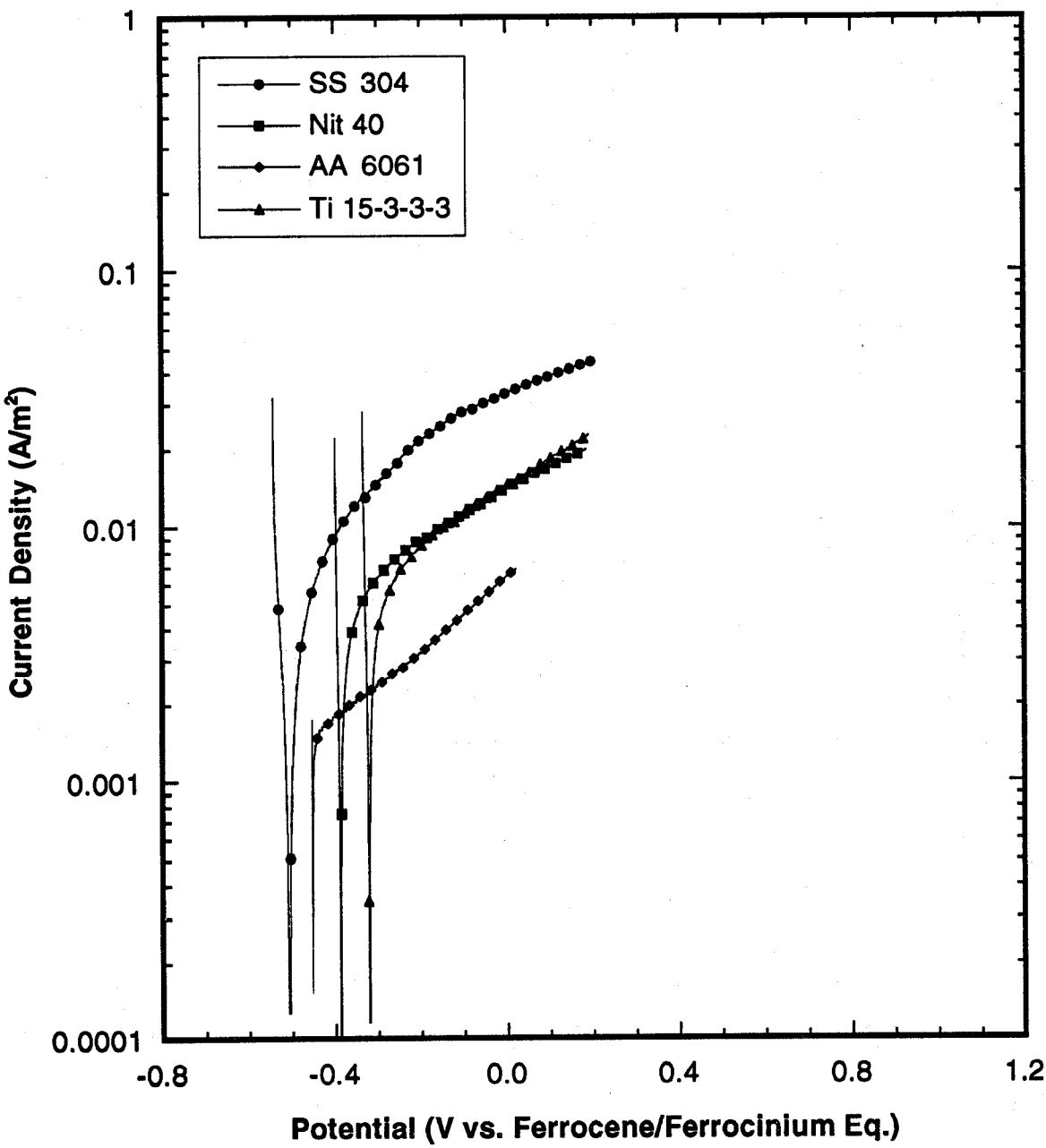

Figure 26. Potentiodynamic scans of 304SS, Nitronic 40, Al 6061-T6, and Ti 15-3-3-3 in HCFC-125 containing 5 x 10^{-2} mol/L of TBATFMS (1 out of 50 data points shown).

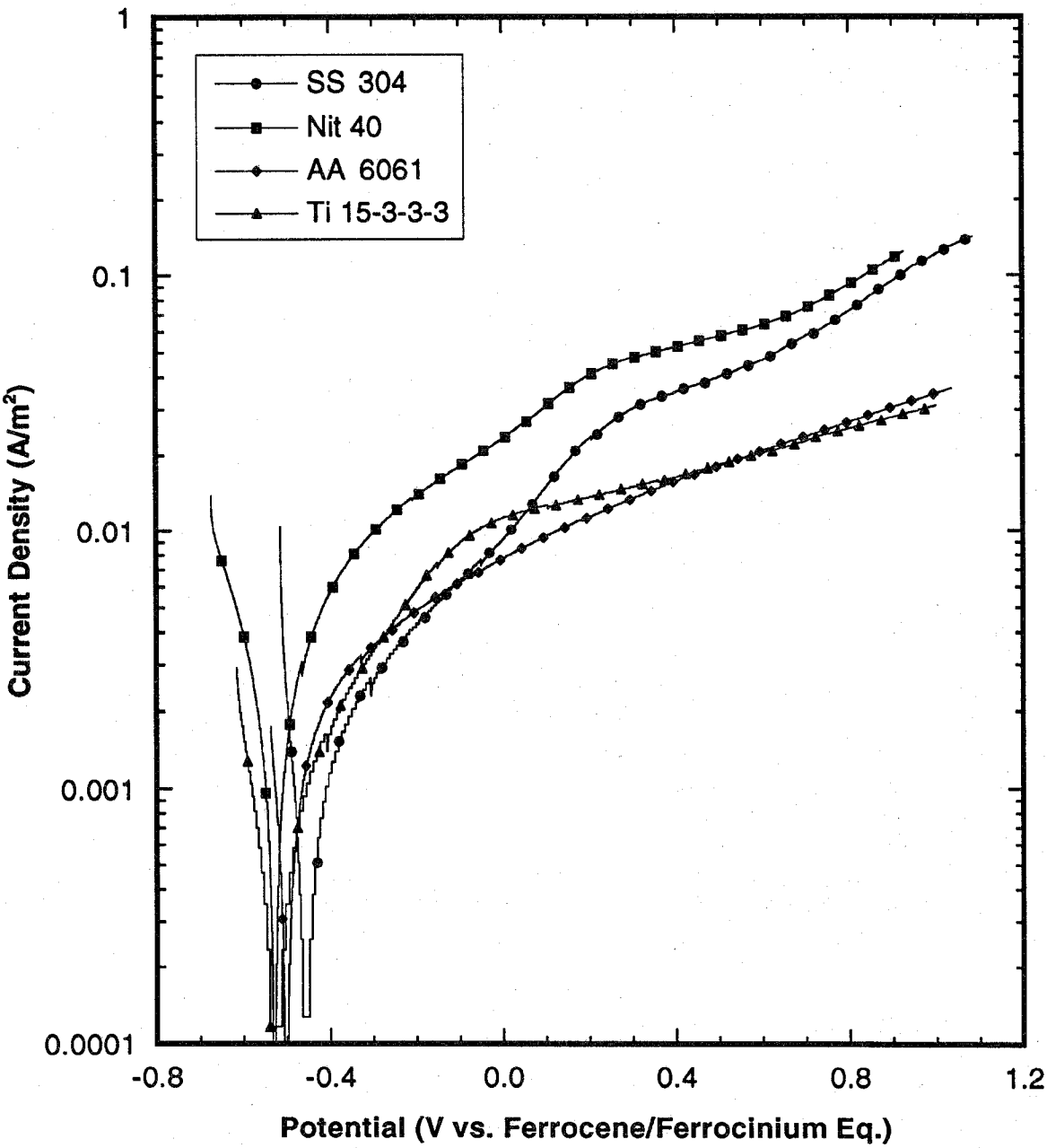

Figure 27. Potentiodynamic scans of 304SS, Nitronic 40, Al 6061-T6, and Ti 15-3-3-3 in CF_3I containing 5 x 10^{-2} mol/L of TBATFMS (1 out of 50 data points shown).

Table 39. Polarization for various alloys in replacement candidates as compared to weight change values after a 30 day immersion

Agent	Alloy	E_{Corr} (Volts)	ICorr (A/cm^2)	Estimated ΔM/A ($g/m^2 \cdot day$)	Measured ΔM/A ($g/m^2 \cdot day$)
HCFC-124	Nitronic 40	-0.066	$1.18x10^{-2}$	$-29.5x10^{-3}$	---
HCFC-124	304 Stainless Steel	-0.314	$3.97x10^{-3}$	$-9.93x10^{-3}$	---
HCFC-124	Al 6061-T6	-0.401	$3.67x10^{-3}$	$-2.96x10^{-3}$	---
HCFC-124	Ti 15-3-3-3	-0.435	$2.52x10^{-3}$	$-5.40x10^{-3}$	---
HFC-125	Nitronic 40	-0.388	$4.15x10^{-3}$	$-10.38x10^{-3}$	$2.79x10^{-3}$
HFC-125	304 Stainless Steel	-0.508	$4.73x10^{-3}$	$-11.82x10^{-3}$	$6.75x10^{-3}$
HFC-125	Al 6061-T6	-0.453	$1.50x10^{-3}$	$-1.21x10^{-3}$	$10.21x10^{-3}$
HFC-125	Ti 15-3-3-3	-0.320	$5.58x10^{-3}$	$-11.96x10^{-3}$	$0.89x10^{-3}$
CF_3I	Nitronic 40	-0.532	$3.72x10^{-3}$	$-9.30x10^{-3}$	$-1.01x10^{-3}$
CF_3I	304 Stainless Steel	-0.460	$1.16x10^{-3}$	$-2.90x10^{-3}$	$-0.39x10^{-3}$
CF_3I	Al 6061-T6	-0.501	$2.11x10^{-3}$	$-1.70x10^{-3}$	$1.09x10^{-3}$
CF_3I	Ti 15-3-3-3	-0.531	$6.63x10^{-4}$	$-1.42x10^{-3}$	$0.58x10^{-3}$

occurred. Attempts to remove this film and measure an actual metal dissolution rate were unsuccessful. Therefore, the conclusions that can be drawn from comparisons of columns 3 and 4 in Table 39 are limited. However, it is interesting to note that all but one of the corrosion weight loss data values obtained using electrochemical techniques are within one order of magnitude of immersion test values. Furthermore, the absolute value of all but one of the electrochemical data are greater than the absolute values of the immersion test values. This would indicate that the electrochemical data would allow for a worse case design criteria based on the higher corrosion values. It is believed that the electrochemical data is more realistic in this study because a true dissolution rate was not obtained for the immersion tests. According to the electrochemical data, it appears that Al 6061-T6 has the best overall performance in the agents studied. It is interesting to note that the Al alloy has the highest weight gain in both HFC-125 and CF_3I. This is probably indicative of the formation and growth of a protective layer.

5.5.7 Corrosion Rates of Metals in Other Halon Replacement Agents. From the data in Table 39, it appears that, in general, the corrosion rates for the various metals are lower in CF_3I than for the other two replacement environment. The lower dielectric constant for this medium is believed to be the reason for this lower value. Typical charged species involved in corrosion have a low probability of being dissolved in a low dielectric constant media because of their low charge to volume ratio resulting in a lower corrosion rate.

The other halon replacement agents under consideration, FC-218 and HFC-227ea have lower dielectric constants than those examined in these electrochemical experiments. In support of this assumption, the salts used in this study did not dissolve in FC-218 or HFC-227ea. Thus, it is proposed that the corrosion rate of storage vessel alloys in these media will be less than those measured here because the solubility of aggressive species and corrosion products will be reduced.

5.6 Conclusions

The primary objective of this investigation was to determine whether any of the candidates selected as potential replacements for halon 1301 should be eliminated from further consideration because of unacceptable corrosion rates of the metals used in the fire suppressant storage and distribution systems on aircraft. In Phase II of this study, the remaining candidates from the screening process (Phase I) were examined for longer times and over a broader range of environmental conditions. In addition, this phase examined both the corrosivity of a representative post deployment deposit on aircraft structural materials and the use of supporting salts which resolved the resistivity of the suppressants thereby enabling electrochemical measurements of corrosion rates.

As in the first phase of this investigation, no single candidate was found to cause serious corrosion problems with all of the alloys and no serious concerns were raised for all of the alloys in any of the agents. However, some agents did consistently demonstrate poorer performance than others or yielded results which indicate further testing is warranted before they should be placed into service. In particular, CF_3I demonstrated higher mass change rates for most of the alloys than the other agents requiring a mass change scale at least one order of magnitude larger than halon 1301 to plot the results. The other agents demonstrated mass change rates that essentially the same or less than those observed for halon 1301. Visual examination of the samples after the exposure tests revealed that AISI 4130 developed small pits during exposure to HFC-227ea, FC-218, and CF_3I with the largest pits being observed in CF_3I. Small pits were also observed in Nitronic 40 and Al 6061 during exposure to HFC-227ea. The only agent to demonstrate any conclusive evidence of environmental induced fracture during the slow strain rate tensile tests was CF_3I which caused cracking of two of the three samples tested at 150 °C.

Electrochemical measurements could only be made in three of the agents: HCFC-124, HFC-125, and CF_3I. Presumably, the corrosion rates in the others would be lower than these three due the same factors that inhibit the measurement of corrosion rate (high resistivity and dielectric constant). Of these three, the lowest corrosion rates were observed in CF_3I which is in contrast to the immersion test results. This may be due to the formation of protective surface films that slow corrosion resulting in a lower average corrosion rate over the long exposure times in the other agents or it could be an indication that the corrosivity observed for CF_3I is the result of second phase contaminants present in the agent as supplied and the fact that the electrochemical experiments used smaller volumes of agent and very small area samples which would result in a much lower probability of contaminating the surface with an aggressive species such as a halogen acid. If contaminants are responsible for the poor performance of CF_3I in these tests, then removal of these impurities could make this agent acceptable for use.

The results of this investigation demonstrate that it may be possible to use any of these agents in aircraft fire suppression systems, but before CF_3I is used, a better understanding of the factors influencing its corrosivity will be needed. Also, this conclusion is based on the quality of the agents as supplied for testing and changes in the impurity content of any of the agents could result in dramatic shifts in the corrosivity. Assuming that the performance of the CF_3I was the result of trapped impurities, then the presence of similar impurities in any of the agents should result in similar levels of performance.

5.7 Acknowledgments

The authors would like to thank Dr. Thomas Moffat and Mr. Carlos Beauchamp of NIST for their technical assistance and helpful suggestions during the design and development of the electrochemical techniques. We also would like to thank Mr. George Hicho and Mr. Richard Harris, also of NIST, for their insightful reviews. We acknowledge Dr. Kumar Jata and Mr. Thomas Naguy of the Wright-Patterson Materials Laboratory for their assistance and recommendations in the selection of the alloys used in this study. The authors especially wish to thank Ms. Joan Teagle, also of NIST, for her dedication and invaluable help with the editing of this document.

5.8 References

ASTM, Standard Test Methods of Tension Testing of Metallic Materials, *Annual Book of ASTM Standards, Section 3, Metals Test Methods and Analytical Procedures,* Philadelphia, PA, 1993.

ASTM, Standard Practice for Preparation and Use of Direct Tension Stress-Corrosion Test Specimens, *Annual Book of ASTM Standards, Section 3, Metals Test Methods and Analytical Procedures*, Philadelphia, PA, 1993.

ASTM, Standard Guide for Applying Statistics to Analysis of Corrosion Data, *Annual Book of ASTM Standards, Section 3, Metals Test Methods and Analytical Procedures*, Philadelphia, PA, 1993.

ASTM, Standard Practice for Laboratory Immersion Corrosion Testing of Metals, *Annual Book of ASTM Standards, Section 3, Metals Test Methods and Analytical Procedures*, Philadelphia, PA, 1993.

Bard, A. J., and Faulkner, L. R., *Electrochemical Methods, Fundamentals and Applications*, John Wiley and Sons, Inc., New York, 1980.

Bond, A. M., Henderson, T. L. E., Mann, D. R., Thormann, W., and Zoski, C. G., (1988), "Fast Electron Transfer Rate for the Oxidation of Ferrocene in Acetronitrile or Dichloromethane at Pt Disk Ultramicroelectrodes," *Anal. Chem. 60*, D. R. Lide, ed., 1978.

CRC Handbook of Chemistry and Physics (71st ed.), W. Palm Beach, FL CRC Press, 1990.

Dante, J. F., Stoudt, M. R., Fink, J. L., Beauchamp, C. R., Moffat, T. P., and Ricker, R. E., "Evaluation of the Corrosion Behavior of Storage Container Alloys in Halon 1301 Replacement Candidate Agents," Paper presented at the Tri-Service Conference on Corrosion, Orlando, FL 1994.

Deiter, G. E., *Mechanical Metallurgy* (3rd ed,) McGraw-Hill Series in Materials Science and Engineering, 275-324, McGraw-Hill, New York, 1986.

Fontana, M. G., and Greene, N. D., *Corrosion Engineering*, McGraw-Hill Series in Materials Science and Engineering, McGraw-Hill, New York, 1987.

Kadish, K. M., Ding, J. Q., and Malinski, T., "Resistance of Nonaqueous Solvent Systems Containing Tetraalkylammonium Salts," *Anal. Chem. 56*, 1741, 1984.

Linteris, G., Prediction of HF Formation During Suppression, 1994.

Mendenhall, W., & Sincich, T., Statistics for Engineering and the Sciences, San Francisco, Dellen Publ. Co., 1992.

Metals Handbook: Vol 12, Fractography, K. Mills *et al*, eds. (9th ed.), Metals Park, OH, ASM International, 1987.

Metals Handbook: Vol 9, Metallography and Microstructures, H. E. Boyer, (8th ed.), Metals Park, OH, ASM International, 1987.

Metals Handbook: Vol 13, Corrosion, L. J. Korb *et al.*, eds. (9th ed.), 669-706, Metals Park, OH, ASM International, 1987.

Nyden, M., Linteris, G., Burgess, D. R. F. Jr., Westmoreland, P. R., Tsang, W., and Zachariah, M. R., in *Evaluation of Alternative In-Flight Fire Suppressants for Full Scale Testing in Simulated Aircraft Engine Nacelles and Dry Bays*, NIST Special Publication 861, NIST, 1994.

Park, J., and Shaw, B. R., "Improved Performance of Unmodified and Cobalt Phthalocyanine-Modified Carbon-Kel F Composite Electrodes," *J. Electrochem. Soc. 56*, 1741, 1994.

Pournaghi-Azar, M. H., and Ojani, R., "Electrode Kinetic Parameters of the Ferrocene Oxidation at Pt, Au and Glassy Carbon Electrodes in Chloroform," *Electrochimica Acta 39*, 953, 1994.

Ricker, R. E., Stoudt, M. R., Dante, J. F., Fink, J. L., Beauchamp, C. R., and Moffat, T. P., in *Evaluation of Alternative In-Flight Fire Suppressants for Full Scale Testing in Simulated Aircraft Engine Nacelles and Dry Bays*, NIST Special Publication 861, NIST, 1994.

Sawyer, D. T., and Roberts, J. L., *Experimental Electrochemistry for Chemists*, John Wiley and Sons, Inc., New York, 1974.

Stoudt, M. R., Escalante, E., and Ricker, R. E., "The Influence of Moisture and Pressure on the Mechanical Properties of a Glass-Epoxy Matrix Composite and a Graphite-Epoxy Matrix Composite," *Environmental Effects on Advanced Materials*, San Diego, CA, 1991.

Stoudt, M. R., Fink, J. L., and Ricker, R. E., "The Environmentally-Induced Failure Susceptibility of Fire Suppressant Storage Container Alloys In Replacement Candidates for Halon 1301," In Press, 1995.

Stoudt, M. R., and Ricker, R. E., "Characterization of the Hydrogen Induced Cold Cracking Susceptibility at Simulated Weld Zones in HSLA-100 Steel," NISTIR 5408, NIST, 1994.

Stoudt, M. R., Fink, J. L., and Ricker, R. E., "Evaluation of the Stress Corrosion Cracking Susceptibility of Fire Suppressant Storage Container Alloys in Replacement Candidates for Halon 1301," Paper presented at the Tri-Service Conference on Corrosion, Orlando, FL, 1994.

Ue, M., "Mobility and Ionic Association of Li and Quaternary Ammonium Salts in Propylene Carbonate and -Butyrolactone," *J. Electrochem. Soc. 141*, 3336, 1994.

Zotikov, V. S., Bakhmutova, G. B., Bocharova, N. A., and Semenyuk, E. Y., "Corrosion of Al and its Alloys in Hydrofluoric Acid," *Prot. Met. 10*, 2, 154-156, 1974.

Appendix A. Mass Change Measurements at 150 °C

Sample Number	Test Environ. 150 °C	ΔM/Area 30 Days g/m^2	ΔM/Area 60 Days g/m^2	ΔM/Area 120 Days g/m^2	ΔM/Area 180 Days g/m^2	ΔM/Area 365 Days g/m^2
NIT40/13	HFC-227ea	0.11681	0.15692	0.14866	0.14866	---
NIT40/14	HFC-227ea	0.17698	0.18878	0.42003	0.14040	---
NIT40/15	HFC-227ea	0.14394	0.13215	0.18878	0.15810	---
NIT40/16	FC-218	0.17934	0.75866	4.43396	3.26942	---
NIT40/17	FC-218	0.10855	0.35160	4.23220	3.28476	---
NIT40/18	FC-218	0.13804	0.35632	3.78267	2.80809	---
NIT40/19	halon 1301	0.17108	0.23479	0.30559	0.36694	0.31031
NIT40/20	halon 1301	0.12743	0.18288	0.27845	0.34924	0.36694
NIT40/21	halon 1301	0.12153	0.19822	0.26075	0.29143	0.31503
NIT40/22	HFC-125	0.02124	0.06135	0.06371	0.12389	0.09675
NIT40/23	HFC-125	0.07197	0.09439	0.11563	0.11563	0.11091
NIT40/24	HFC-125	0.06253	0.06843	0.09557	0.08023	0.09675
NIT40/25	CF_3I	16.16778	16.47808	17.56002	---	---
NIT40/26	CF_3I	15.40322	16.09344	8.26972	---	---
NIT40/27	CF_3I	17.85381	18.71158	9.64663	---	---

Sample Number	Test Environ. 150 °C	ΔM/Area 30 Days g/m^2	ΔM/Area 60 Days g/m^2	ΔM/Area 120 Days g/m^2	ΔM/Area 180 Days g/m^2	ΔM/Area 365 Days g/m^2
6061/13	HFC-227ea	0.42492	0.63796	1.00595	1.25245	---
6061/14	HFC-227ea	0.53056	0.58925	0.73011	0.98834	---
6061/15	HFC-227ea	0.44957	0.59629	0.52000	0.72658	---
6061/16	FC-218	0.47774	0.73363	9.49842	7.84688	---
6061/17	FC-218	0.35097	0.67846	0.49652	0.17607	---
6061/18	FC-218	0.29228	0.55051	1.04469	0.55990	---
6061/19	halon 1301	0.42609	0.97074	1.26419	1.34635	1.24775
6061/20	halon 1301	0.36153	0.56812	0.94609	0.98600	0.90852
6061/21	halon 1301	0.36153	0.52234	0.95665	0.92026	0.87801
6061/22	HFC-125	0.25472	0.47422	0.93317	0.99656	0.94961
6061/23	HFC-125	0.23711	0.48243	0.91087	0.84044	0.96839
6061/24	HFC-125	0.26411	0.51647	0.79232	0.72893	0.89444
6061/25	CF_3I	2.17389	5.46523	8.58872	---	---
6061/26	CF_3I	0.41201	2.32061	4.04376	---	---
6061/27	CF_3I	0.27584	2.76900	5.07201	---	---

Sample Number	Test Environ. 150 °C	ΔM/Area 30 Days g/m^2	ΔM/Area 60 Days g/m^2	ΔM/Area 120 Days g/m^2	ΔM/Area 180 Days g/m^2	ΔM/Area 365 Days g/m^2
304/13	HFC-227ea	0.17679	0.22831	0.19318	0.19201	---
304/14	HFC-227ea	0.14752	0.20957	0.20372	0.18850	---
304/15	HFC-227ea	0.13464	0.17913	0.19552	0.14518	---
304/16	FC-218	0.23182	0.49993	7.36548	4.32727	---
304/17	FC-218	0.14284	0.33953	7.80453	4.95715	---
304/18	FC-218	0.16625	0.30441	6.66301	4.37644	---
304/19	halon 1301	0.26811	0.25992	0.30909	0.37348	0.33602
304/20	halon 1301	0.20840	0.22948	0.28099	0.31846	0.32665
304/21	halon 1301	0.17445	0.20255	0.26109	0.33016	0.31612
304/22	HFC-125	0.04566	0.10303	0.16157	0.24235	0.19904
304/23	HFC-125	0.09601	0.14752	0.15455	0.15103	0.16625
304/24	HFC-125	0.07142	0.13230	0.15220	0.16859	0.14401
304/25	CF_3I	9.23290	14.76492	32.35966	---	---
304/26	CF_3I	11.33448	20.14005	24.00251	---	---
304/27	CF_3I	10.09344	16.99412	15.15245	---	---

Sample Number	Test Environ. 150 °C	ΔM/Area 30 Days g/m^2	ΔM/Area 60 Days g/m^2	ΔM/Area 120 Days g/m^2	ΔM/Area 180 Days g/m^2	ΔM/Area 365 Days g/m^2
Ti/13	HFC-227ea	0.25954	0.37657	0.28503	0.02665	---
Ti/14	HFC-227ea	0.17728	0.25491	0.19466	0.21088	---
Ti/15	HFC-227ea	0.20393	0.30357	0.29778	0.29546	---
Ti/16	FC-218	0.30705	0.88986	0.98603	0.80528	---
Ti/17	FC-218	0.26418	0.38468	0.89566	0.66392	---
Ti/18	FC-218	0.22478	0.33717	1.56074	1.32205	---
Ti/19	halon 1301	0.17728	0.26418	0.34181	0.35571	0.41249
Ti/20	halon 1301	0.19582	0.24796	0.38816	0.44957	0.40322
Ti/21	halon 1301	0.19813	0.26765	0.40438	0.46695	0.44957
Ti/22	HFC-125	0.08111	0.18307	0.19118	0.21899	0.29199
Ti/23	HFC-125	0.06836	0.13325	0.14715	0.17959	0.17264
Ti/24	HFC-125	0.12166	0.20045	0.19118	0.19118	0.19466
Ti/25	CF_3I	4.89308	3.14696	6.10969	---	---
Ti/26	CF_3I	4.51188	3.35089	4.15385	---	---
Ti/27	CF_3I	4.46322	3.86882	5.35540	---	---

Sample Number	Test Environ. 150 °C	ΔM/Area 60 Days g/m^2	ΔM/Area 150 Days g/m^2
4130/13	HFC-227ea	-24.06626	-38.42012
4130/14	HFC-227ea	0.32681	-2.49535
4130/15	HFC-227ea	0.48845	-0.18287
4130/16	FC-218	3.79199	4.33117
4130/17	FC-218	2.96846	3.53360
4130/18	FC-218	2.86936	10.36130
4130/19	halon 1301	1.58098	2.68766
4130/20	halon 1301	2.08241	2.81626
4130/21	halon 1301	1.99982	2.62867
4130/22	HFC-125	1.46181	-1.02528
4130/23	HFC-125	0.85538	0.75981
4130/24	HFC-125	0.56042	0.46485
4130/25	CF_3I	-65.49613	-106.61335
4130/26	CF_3I	-74.17617	-57.24083
4130/27	CF_3I	-33.08845	-53.94674

Sample Number	Test Environ. 150 °C	ΔM/Area 90 Days g/m^2
321/04	halon 1301	1.38949
321/05	halon 1301	2.78602
321/06	halon 1301	1.49176
321/10	HFC-125	0.01411
321/11	HFC-125	0.01411
321/12	HFC-125	0.00823

Sample Number	Test Environ. 150 °C	ΔM/Area 90 Days g/m^2
CDA110/04	halon 1301	1.52769
CDA110/05	halon 1301	1.77123
CDA110/06	halon 1301	1.43710
CDA110/10	HFC-125	0.05824
CDA110/11	HFC-125	0.12706
CDA110/12	HFC-125	0.02647

Sample Number	Test Environ. 150 °C	ΔM/Area 90 Days g/m^2
CDA172/04	halon 1301	5.89103
CDA172/05	halon 1301	2.10562
CDA172/06	halon 1301	3.28194
CDA172/10	HFC-125	2.47205
CDA172/11	HFC-125	2.35912
CDA172/12	HFC-125	2.45440

Sample Number	Test Environ. 150 °C	ΔM/Area 90 Days g/m^2
355/04	halon 1301	1.04301
355/05	halon 1301	1.42683
355/06	halon 1301	1.90702
355/10	HFC-125	0.00459
355/11	HFC-125	0.03901
355/12	HFC-125	0.01893

Sample Number	Test Environ. 150 °C	ΔM/Area 90 Days g/m^2
I625/04	halon 1301	0.62422
I625/05	halon 1301	0.67142
I625/06	halon 1301	0.68322
I625/10	HFC-125	-0.01534
I625/11	HFC-125	-0.03186
I625/14	HFC-125	-0.07434

Appendix B. Mass Change Measurements at 20 °C

Sample Number	Test Environ. 20 °C	ΔM/Area 30 Days g/m^2	ΔM/Area 60 Days g/m^2	ΔM/Area 120 Days g/m^2	ΔM/Area 180 Days g/m^2	ΔM/Area 365 Days g/m^2
NIT40/01	HFC-125	0.08377	0.08377	0.15928	0.21238	0.65955 0.08613
NIT40/02	HFC-125	0.03068	-0.01652	0.06371	0.12271 0.12979	0.09793
NIT40/03	HFC-125	0.00236	0.01888	0.06017		
NIT40/04	HFC-227ea	0.01770	0.06607	0.09793	0.09911 0.05073	---
NIT40/05	HFC-227ea	-0.01062	0.03894	0.05545	0.07905	---
NIT40/06	HFC-227ea	-0.02950	0.03422	0.06253		---
NIT40/07	halon 1301	0.11799	0.14748	0.14984	0.28199	0.15928 0.16872
NIT40/08	halon 1301	-0.00118	0.02596	0.05545	0.10265 0.09557	0.14394
NIT40/09	halon 1301	-0.00236	0.03068	0.06725		
NIT40/10	FC-218	0.01298	0.07551	0.11563	0.12743	---
NIT40/11	FC-218	0.02950	0.05781	0.02950	0.08023 0.05781	---
NIT40/12	FC-218	-0.01416	0.04484	0.03422		---
NIT40/28	CF_3I	-0.03068	-0.00708	0.26547	---	---
NIT40/29	CF_3I	-0.01180	0.06253	0.12507	---	---
NIT40/30	CF_3I	-0.03658	0.02950	0.09439	---	---

Sample Number	Test Environ. 20 °C	ΔM/Area 30 Days g/m^2	ΔM/Area 60 Days g/m^2	ΔM/Area 120 Days g/m^2	ΔM/Area 180 Days g/m^2	ΔM/Area 365 Days g/m^2
6061/01	HFC-125	0.30636	0.42609	0.80992	0.96487 0.49065	1.19376 0.57986
6061/02	HFC-125	0.01409	0.08686	0.40614	0.55638	0.68315
6061/03	HFC-125	0.00352	0.09860	0.48713		
6061/04	HFC-227ea	0.05165	0.36857	0.50474	0.55990 0.74419	---
6061/05	HFC-227ea	0.00587	0.28993	0.45074	0.47187	---
6061/06	HFC-227ea	0.00235	0.27467	0.38501		---
6061/07	halon 1301	0.11738	2.53072	9.66862	-8.98664	-9.22493
6061/08	halon 1301	0.02348	0.33219	0.02348	0.08569 3.35238	-0.44957
6061/09	halon 1301	0.03521	-0.00352	1.33109		-2.11285
6061/10	FC-218	0.03639	0.34392	0.46952	0.57869 0.91791	---
6061/11	FC-218	0.05986	0.56225	0.82284	0.80288	---
6061/12	FC-218	0.04343	0.45426	0.71485		---
6061/28	CF_3I	0.00352	4.36068	-4.69052	---	---
6061/29	CF_3I	0.03991	53.50903	-6.39019	---	---
6061/30	CF_3I	0.03287	78.45355	-17.90990	---	---

Sample Number	Test Environ. 20 °C	ΔM/Area 30 Days g/m^2	ΔM/Area 60 Days g/m^2	ΔM/Area 120 Days g/m^2	ΔM/Area 180 Days g/m^2	ΔM/Area 365 Days g/m^2
304/01	HFC-125	0.20255	0.21660	0.32548	0.41212 0.07844	0.51398 0.09249
304/02	HFC-125	-0.01756	-0.01756	0.06088	0.13815	0.08781
304/03	HFC-125	0.00937	0.01288	0.06791		
304/04	HFC-227ea	0.03512	0.07493	0.08781	0.09015 0.08898	---
304/05	HFC-227ea	-0.00351	0.02459	0.02225	0.07259	---
304/06	HFC-227ea	-0.00820	0.04449	0.04566		---
304/07	halon 1301	0.05503	0.23182	0.13113	0.29153 0.22245	0.19669 0.15572
304/08	halon 1301	0.02107	0.03161	0.07376	0.29504	0.24587
304/09	halon 1301	-0.01873	0.03512	0.10771		
304/10	FC-218	0.01054	0.12059	0.04566	0.14635 0.09015	---
304/11	FC-218	-0.00585	0.05034	0.07142	0.09015	---
304/12	FC-218	-0.00234	0.03512	0.04566		---
304/13	CF_3I	-0.01171	0.31143	0.54559	---	---
304/14	CF_3I	-0.02576	0.27162	0.33485	---	---
304/15	CF_3I	-0.01054	0.18850	0.44959	---	---

Sample Number	Test Environ. 20 °C	ΔM/Area 30 Days g/m^2	ΔM/Area 60 Days g/m^2	ΔM/Area 120 Days g/m^2	ΔM/Area 180 Days g/m^2	ΔM/Area 365 Days g/m^2
Ti/01	HFC-125	0.02665	0.03128	0.07300	0.13788 0.13904	0.22594 0.14368
Ti/02	HFC-125	0.00579	0.02549	0.09733	0.16106	0.16569
Ti/03	HFC-125	-0.01275	0.03592	0.13325		
Ti/04	HFC-227ea	0.01275	0.05098	0.10892	0.12050 0.11587	---
Ti/05	HFC-227ea	-0.01506	0.08574	0.08458	0.11471	---
Ti/06	HFC-227ea	0.00463	0.04055	0.09849		---
Ti/07	halon 1301	0.00927	0.10080	0.10196	0.14020 0.12861	0.18307 0.17496
Ti/08	halon 1301	-0.00811	0.06604	0.06720	0.18539	0.20856
Ti/09	halon 1301	0.03013	0.11239	0.10660		
Ti/10	FC-218	0.01854	0.07995	0.09269	0.18886 0.13556	---
Ti/11	FC-218	0.00000	0.06604	0.09269	0.12398	---
Ti/12	FC-218	0.02665	0.07995	0.09965		---
Ti/28	CF_3I	0.01738	0.29083	0.35571	---	---
Ti/29	CF_3I	-0.03476	0.06720	0.23405	---	---
Ti/30	CF_3I	-0.01854	0.10080	0.24680	---	---

Sample Number	Test Environ. 20 °C	ΔM/Area 60 Days g/m^2	ΔM/Area 150 Days g/m^2
4130/01	HFC-125	0.30558	0.49553
4130/02	HFC-125	0.13686	0.96156
4130/03	HFC-125	1.44058	2.59917
4130/04	HFC-227ea	0.09675	---
4130/05	HFC-227ea	0.32209	---
4130/06	HFC-227ea	-1.05241	---
4130/07	halon 1301	2.14140	-1.28838
4130/08	halon 1301	0.28906	6.95394
4130/09	halon 1301	0.41648	6.62123
4130/10	FC-218	0.48373	---
4130/11	FC-218	0.57340	---
4130/12	FC-218	0.25838	---
4130/30	CF_3I	69.90163	87.28177
4130/31	CF_3I	44.32047	88.18198
4130/32	CF_3I	39.79817	80.18507

Sample Number	Test Environ. 150 °C	ΔM/Area 90 Days g/m^2
321/01	halon 1301	0.06701
321/02	halon 1301	0.05172
321/03	halon 1301	0.06877
321/07	HFC-125	0.04702
321/08	HFC-125	0.00000
321/09	HFC-125	0.03409

Sample Number	Test Environ. 150 °C	ΔM/Area 90 Days g/m^2
CDA110/01	halon 1301	0.20589
CDA110/02	halon 1301	0.09883
CDA110/03	halon 1301	0.07412
CDA110/07	HFC-125	0.11059
CDA110/08	HFC-125	-0.00118
CDA110/09	HFC-125	-0.00471

Sample Number	Test Environ. 150 °C	ΔM/Area 90 Days g/m^2
CDA172/01	halon 1301	-0.05058
CDA172/02	halon 1301	0.00118
CDA172/03	halon 1301	-0.00588
CDA172/07	HFC-125	0.05646
CDA172/08	HFC-125	0.00706
CDA172/09	HFC-125	-0.04705

Sample Number	Test Environ. 150 °C	ΔM/Area 90 Days g/m^2
355/01	halon 1301	-0.02295
355/02	halon 1301	0.06196
355/03	halon 1301	0.02065
355/07	HFC-125	-0.07803
355/08	HFC-125	0.02065
355/09	HFC-125	0.05508

Sample Number	Test Environ. a150 °C	ΔM/Area 90 Days g/m^2
I625/01	halon 1301	0.00708
I625/02	halon 1301	0.00708
I625/03	halon 1301	0.03009
I625/07	HFC-125	-0.00354
I625/08	HFC-125	0.01593
I625/09	HFC-125	-0.00177